Evolution of Stresses and Microstructure in Thermal Barrier Coatings: A Multiscale Modeling Framework

By
Francisco Bernabe Pascual

A Thesis Presented to the

Masdar Institute of Science and Technology

In Partial Fulfillment of the Requirements for the

Degree of

Industrial Engineering

In

Universidad Carlos III de Madrid

Abstract

The development of modern gas turbine (GT) engines has been the result of continual improvements in a wide variety of engineering disciplines including turbine design, combustion, and materials. Hot section components of the GT engine are required to operate in harsh environments significantly in excess of their melting temperatures, requiring extensive cooling coupled with heat resistant and protective coatings. Thermal barrier coatings (TBCs) comprise several layers and are designed to simultaneously provide thermal and oxidation protection. Development of high performance TBCs require a better understanding of the complex changes in their structures and properties that occur under operating conditions that lead to their failure. In this study, initially, multiscale analytical models were developed based on a thermodynamic variational principle to model sintering and microstructure evolution in thermal barrier top coat made using the electron beam physical vapour deposition route. It is assumed that the sintering occurs by interfacial diffusion at local contacts between columnar grains and driven by changes in interface free energy and elastic stored energy of the coating. The models link diffusional processes at the scale of contacting feathery columns with the macroscopic deformation and sintering response. Each member of the multi-layered TBC system is dynamic and all interact to control the performance and durability. Therefore, continuum level analytical and computational models were developed to determine the stresses generated in the coating system upon cool down to room temperature from maximum operating temperature accounting for temperature dependent material properties and spatial variation of TBCs properties due to sintering. The effect of sintering on the stresses in the thermally grown oxide layer (TGO) was also examined. Furthermore, the effect of stress dependent creep both in the bond coat and TGO during service at high temperature on the stress evolution was studied. In addition, rumpling and growth of TGO due to oxidation were also analyzed to gain insight into the failure behavior of the TBC system.

This research was supported by the Government of Abu Dhabi to help fulfill the vision of the late President Sheikh Zayed Bin Sultan Al Nahyan for sustainable development and empowerment of the UAE and humankind.

Acknowledgments

I would like to express my more sincere and profound gratitude and admiration to my advisor Prof. Kumar Shanmugam for his guidance and support through the Thesis, without whom I would not be presenting my Thesis today, for the good moments and his patience in the bad ones, because working closely day by day is not always a path of happiness and laughs, but specially for all his effort, and the knowledge and experience he has transfered me during this two years.

My kind thanks to my Thesis committee members Prof. Tariq Shamim and Prof. Amal Al Ghaferi for all their time invested,and their helpful suggestions and criticisms on this Thesis. I also would like to thanks my colleagues from the Advance Materials & Multifunctional Structures Group for all the time and help during the past two years.

I would like to dedicate this Thesis to my parents Francisco Bernabe and Maria Soledad Pascual, for all the sacrifices and hard work they did to give me the required education to meet the standards to join Masdar Institute of Science & Technology. To finish I would like to specially thanks my girlfriend Isabel Barrio who has stayed by my side in all the moments, she gave me strength to follow when I didn't have it and helped me stand when I couldn't hold the weight in my shoulders. Thank you to them and all my friends and family for their tireless and loving support in every step of my life.

Francisco Bernabe,

Masdar City, May 2015.

Contents

List of Tables

List of Figures

CHAPTER 1

Introduction

The improvement of efficiencies in gas turbines used in the transportation, energy, and defense sector rely directly on high-temperature thermal-barrier coatings (TBCs). Thermal barrier coatings are refractory-oxide ceramic coatings adhered to metallic surfaces in the components of the gas-turbines engines exposed to higher temperatures, enabling the turbine to operate at higher inlet gas temperatures. The efficiencies of gas turbines and thus their power is directly related with the temperature at which the gas enters the turbine. To increase the temperature of the entering gas in order to increase the energy efficiency of the gas-turbine engines further improvements in TBCs are needed. This will lead in increase in electricity output, thrust-to-weight ratio and durability in jet gas turbine engines. The high demand of passenger to be able to travel around the globe and the response of the airlines opening new aerial ruts is, increasing the demand of aircrafts and therefore of gas turbines. Just the value of the turbines made during one year exceeded, the annual sales of the top 35 businesses in the world.

There are many factors taking part in the efficiency of gas turbines, but prominent step is increasing the engine temperature were the introduction of Thermal Barrier Coatings comes into picture. The aim of TBCs is to provide thermal insulation to the super-alloy normally Ni-based gas turbine components. The hot components protected with TBCs are combustor, stationary guide vanes, rotating blades, blade outer air-seals and shrouds. The maximum limit of gas temperature is increased with the use of TBCs and cooling techniques are improved better than

acquired by earlier material development.

Thermal barrier coatings are also used in diesel engines, where higher temperature while operating turns into increase in fuel economy and cleaner exhaust. Better understanding of the complex changes in the structure and properties of TBCs under operational conditions that lead to their failure are required to study the improvements in TBCs.

1.1 Gas Turbine Engines

A gas turbine is a rotating device that uses the action of fluid to produce work. A mixture of fuel and air is burned inside the gas turbine which results in hot inlet gases to produce mechanical power converting the internal energy of high temperature gas. Different type of fuels can be utilized, for example natural gas or even synthetic fuels.

1.1.1 Anatomy

The main three components of a gas turbine engine are: compressor, combustor or combustion chamber, and turbine as shown in Fig. 1.1. The compressor compresses the incoming air to high temperature and pressure, passes it to the combustor chamber. Then in combuster this high pressurized air is burned by mixing fuel in it. Then this high pressurized air with high velocity is directed to the turbine where the energy is extracted. The turbine has different stages, each of them with a row of stationary nozzles or blades, that help directing the expanding gases, followed by a stage composed by a row of moving blades. The compressor uses around 60 percent of the power that is being produced by the turbine. The remaining energy is transformed to electricity by means of a generator. Kinetic energy transfer can be optimized by implementing several stages of compressor and turbine in a series, but this is not reliable because increase in efficiency is less in each addition of stage while manufacturing cost increases significantly.

By increasing the operating temperature, the efficiency of the turbine can be increased. The higher the temperature of the inlet gas, higher energy can be derived from the gas turbine.

The components which come across the flow of hot gases experience high thermal loading. The turbine blades are exposed initially to the continuous gas, so they are more vulnerable to thermal damage. The gas enters the turbine in the temperature range of 800^oC to 1700^oC. The

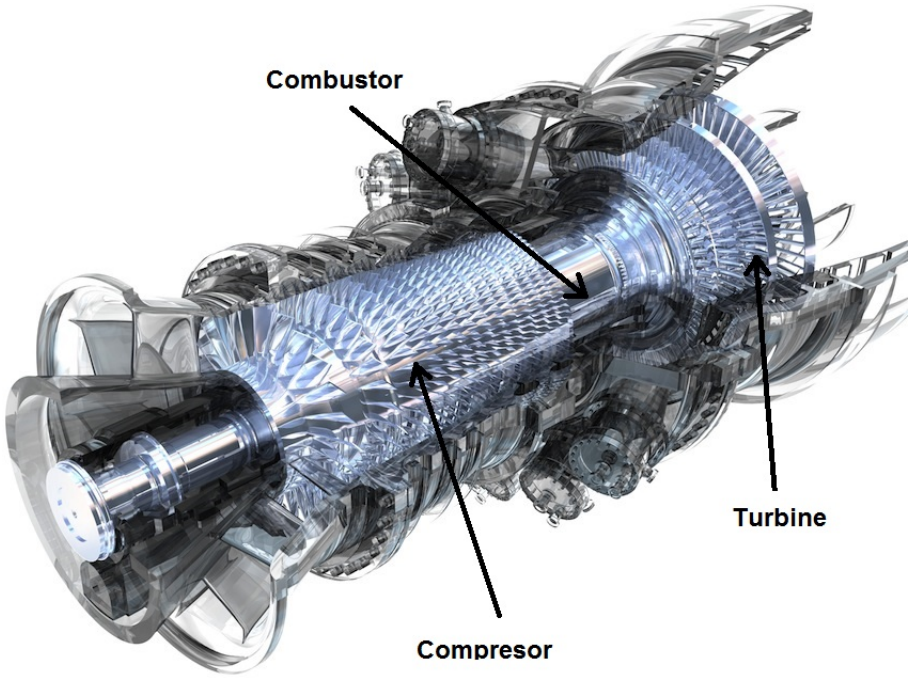

Figure 1.1: Main parts of a Natural Gas Turbine (developed by GE) [20]

maximum temperature limit is more than the melting temperature of the base metal, such as nickel based superalloy. There are various techniques are available for internal and external cooling to keep the maximum temperature of the blade below its melting point. At higher temperatures and long duration runs, turbine blades may fail which may lead to the failure of whole aircraft structure.

1.1.2 Industry

Gas turbines are one of the most used engine in power generation and aerospace industries, and also in some marine applications. In electricity generation, power turbine is used while the gas turbine is used for aviation purpose.

The gas-turbine industry is a 42 billion dollars industry worldwide. A high percentage above 60% of the sales are for jet engines and the remainder is for electricity generation. A big share of this last ones are fueled by liquid fuels or natural gas. Airline traffic is expected to grow at high levels, say twice in the next 20 years. Same scenario is found in the worldwide growth of electricity demand, leading to a tremendous growth in the number of gas turbine engines in

service and jet engines in the coming decades.

1.1.3 Development

The energy generation and aerospace industry have been under significant development in the past decade, and is planned to face a greater growth in the upcoming years. Now a days not even increasing business competition in the sector, but to produce more efficient engines led engine manufacturers for manufacturing of high efficiency gas turbine engines . Today's development of gas turbines engines is the results of continuous improvements and a compilation of different engineering skills during the pass decades.

Efforts were placed in the development of high-temperature and high-strength resistant new materials, air cooling methods and protective coatings. Improved strength capabilities were developed in alloys to resist higher temperatures and increase turbine inlet temperatures. Developments were also made from heat resisting steel and wrought Nickel-Chromium alloys in the nineteen-fifties, Nickel base superalloys extruded blades in the nineteen-sixties, increased alloy temperature capabilities but reduced resistance to oxidation and hot corrosion. In the early seventies, equiaxed cast blades showing high number of grain boundaries and random crystal orientation were developed, that facilitated the inclusion for internal cooling in the design of the blade. Directionally solidified casting began to be used in the late seventies, leading to a fewer boundary conditions and crystal orientation in the radial direction. Maximum resistance to stress produced by centrifugal forces was obtained. Development of single crystal turbine blades, maintaining radial oriented crystal and no grain boundary conditions further enhanced strength capabilities. Introduction of air cooling technology in the nineteen-seventies was crucial to increase the turbine entry temperature, requiring at the same high level design and casting techniques. Evolving from single pass cooling to multi pass cooling to maximize heat transfer between the blade and the cooling air. Figure 3.1 describe the increment in the turbine entry temperature due to the association of implementations in the materials and techniques [65].

The efficiency of the gas turbine is primarily restricted for the high pressure and temperature of the gas in the inlet of the turbine. Higher entry temperatures lead to higher efficiency. Some sections of the turbine are directly exposed to the hot gas and operate in harsh condition over their fusion point requires extensive cooling at the same time. Spallation of the coating driven

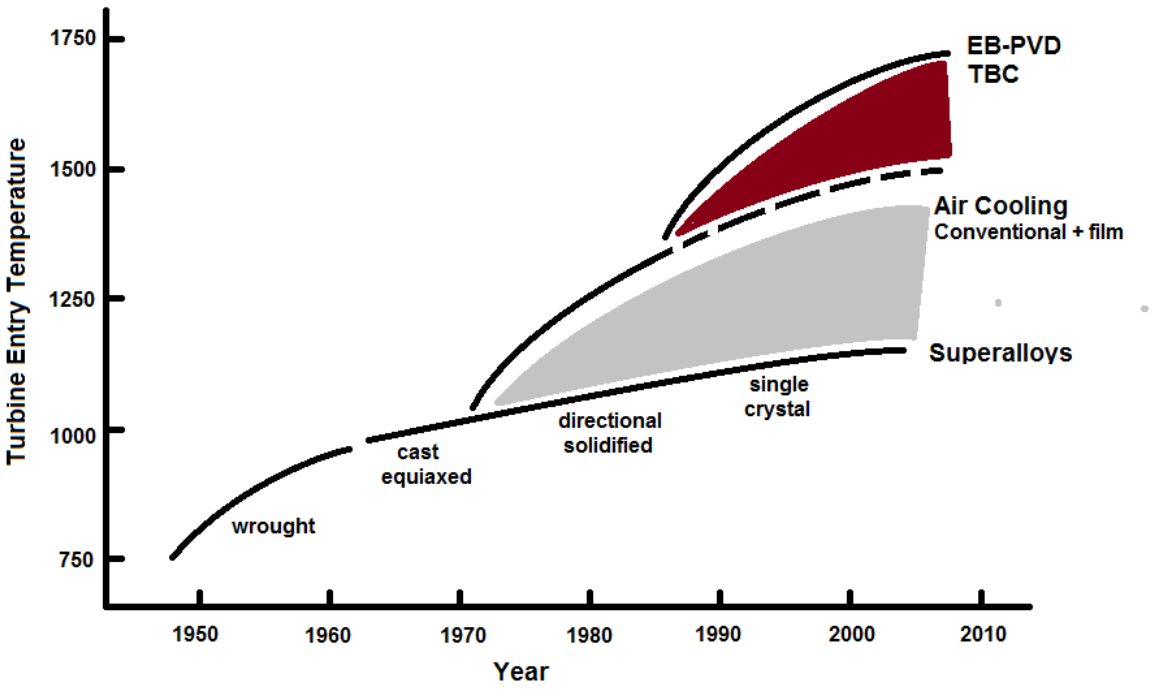

Figure 1.2: Turbine Entry Temperature (TET) development and effect of direct techniques related to it, over the past six decades.

by delamination in such components leads to a quick damage and failure of the component.

By applying TBCs, the temperature in the turbine blades can be dropped on the order of 100^oC to 300^oC. TBCs led not only in better efficiency in the turbine but also in longer durability of the components, since a part from thermal resistance TBCs add corrosion and oxidation resistance. The necessity to increase this operating temperatures of the inlet gas entering the turbine in order to increase the efficiency of the turbine bring the necessity of a development in the coating of the turbine, since the development of better materials for the substrate of the turbine is constrained.

1.2 Thermal Barrier Coatings

Thermal barrier coatings are used in high temperature exposed components, to achieve a high temperature gradient between the nickel based superalloy and the external yttria stabilized zirconia surface. The benefit of the thermal coatings is the life prolongation of the turbine component by decreasing the temperature of the Ni-superalloy substrate and increasing the efficiency of the

turbine. At the same time that reduces environmental attack, creep rupture or fatigue. Today's gas turbine entry temperature have reached the values of 1500^oC and is estimated to increase to 1800^oC in the following decade. A combination of developments in superalloys materials, internal and external cooling, and thermal barrier coatings have been made and will make possible to achieve maximum temperature.

1.2.1 Architecture

TBCs have several layers, where each layer has different properties. Designed to provide simultaneously thermal and oxidation protection [64]. The different layers are:

- TBC: Provides thermal insulation; the preferred material is zirconia stabilized with yttria in solid solution (YSZ). Substrate: Sustains the structural loads, is a super-alloy containing between 5 and 12 additional elements to provide better properties, such as high temperature, strength ductility, oxidation resistance, hot corrosion resistance and casting ability. Diffusion of elements at high temperature between the super-alloy and the bond-coat can occur, and is an important influence in spallation failure of the TBC. To avoid instantaneous delamination of the coating strain tolerance is designed in the material [2]

- Bound-Coat (BC): Metallic and oxidation resistant layer located in between the substrate and the TBC, provides a surface in which the TBC can adhere to avoid the spallation failure having thickness 50-150 μm. Working at a temperature over 700^oC the bond-coat's oxidation can't be avoided and TGO layer is formed.

- Thermally Grown Oxide (TGO): Is formed between the BC and TBC, and provides oxidation protection. Alumina is the preferred selected oxide due to high adherence and low diffusivity of oxygen. Specially high residual stresses are developed and supported by the TGO during cooling cycle to ambient temperature, reaching compressions between 3-6 GPa. The principal reason for this values of compressive stress is the misfit in the thermal expansion coefficient with the substrate. TGO formation is continuous during exposure to high temperatures generating growth of the layer.

- Substrate: Is the base of the turbine blade components, single crystal directional solidified Nickel base superalloy materials are used in the substrate design and manufacturing pro-

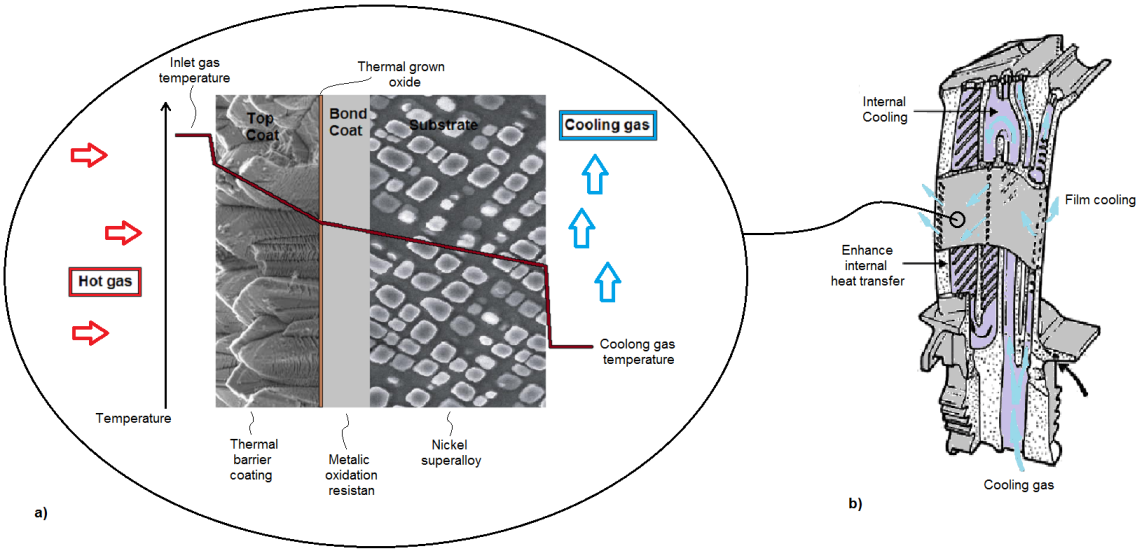

Figure 1.3: a) Representation of thermal barrier coating structure, comprised of a nickel based superalloy, an aluminum rich bond coat, a thermal grown oxide(TGO) and a top coat thermal barrier coating(TBC). Temperature profile presented inside the system during service conditions. b) Conventional+fill gas cooled turbine coated by a TBC system [8].

cess. The material is characterized by enhanced strength capabilities at high temperatures [62].

Studies of different bond coat compositions revealed that the highest resistance to oxidation is shown in coatings with high Aluminide levels, specially nickel/cobalt aluminides. Finally high Chromium level, would oxidate at low temperature, growing a Cr_2O_3 layer and therefore show corrosion protection. This research materials presenting oxidation and corrosion resistance could be suitable for gas turbine use [37].

The TBC thermal expansion coefficient is likely to differ from the thermal expansion coefficient of the substrate. A TBC should therefore have a high in-plane compliance to accommodate the misfit in thermal expansion. A very important feature apart from the thermal stability that a TBC should have is a low sintering rate taking place in the in-plane compliance [32].

1.2.2 Air Plasma Spray Coatings

The deposition is designed to incorporate inter-splat porosity and a network of crack-like voids that again provides some strain tolerance, while lowering the thermal conductivity. Air plasma spray (APS) deposition provides generally tiny better thermal insulation in TBC systems and offers economic advantages but less resistance to mechanical and erosive attack [49]. In the

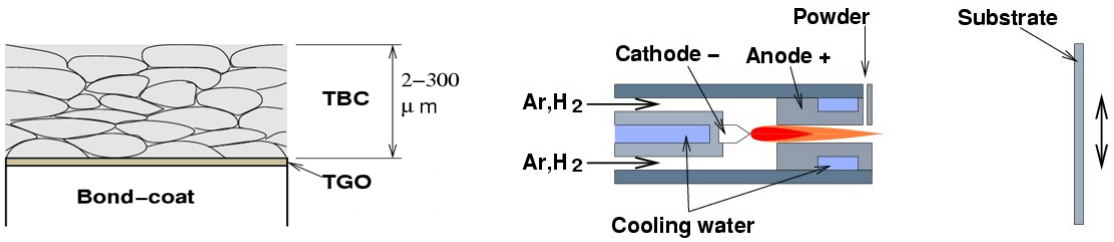

Figure 1.4: a)Illustration of the microstructure acquired by air plasma spray deposition methods. b)Schematic of the deposition process of APS coatings [54].

deposition process normally yttria stabilized zirconia powders are used, the high temperature, high velocity plasma jet is filled by injection of the powder. Once the yttria powder is melted, the jet propels the liquid plasma into the metal surface, that will solidify by the energy transfered by the impact, in the form of the so called splats. The accumulated splats in form of horizontally deformed dots (see Fig.1.2.2) lead to the formation of the coating. Planar porosity are contained in the splats boundaries, this porosity will contribute to lower thermal conductivity and lower mechanical resistance to spallation compared to EB-PVD coatings [34] There are several new processes using plasma spry means, among them we can highlight the solution precursor plasma spry (SPPS) method, which offers low cost, low conductivity and higher durability coatings [40] and sculptured thin films [29][35]

1.2.3 Electron Beam Physical Vapor Deposition Coatings

In electron beam physical vapor deposited coatings, vapor is directed in the preheated component. This is operating under deposition conditions which are designed for multi-scale porosity columnar grain creation. as shown in Fig. 1.2.3. Strain tolerance and thermal conductivity reduction is achieved by multi-scale porosity. Comprehensive understanding of porous microstructure evolution in columnar ceramic TBC lead to great progress in EB-PVD optimization of microstructure [58]. The aim of TBC systems design is to reduce conductivity, increase temperature capabilities and elongate the components life. Deposition of the coating by EB-PVD methods have proved to reduce the thermal conductivity, increase strain tolerance and attractive aerodynamically smooth protective coatings [49]. Electron beam physical vapor deposited YSZ coatings have proven to support reduction of phonon transportation by addition of dopant atoms, technique know as colouring, and allows photon transport reduction due to layered microstructure, by advance processing of the coating. Thermal conductivities reductions to 1 Wm/K have been proved by colouring and layered ceramic coatings techniques, from measurements of 1.6-

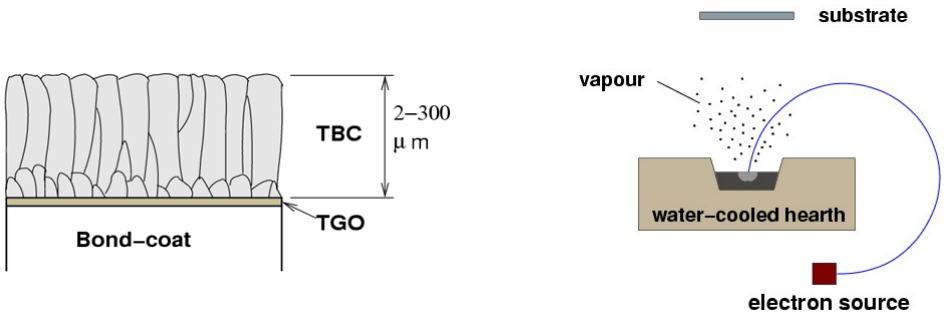

Figure 1.5: a)Illustration of the microstructure acquired by electron beam physical vapor deposition methods. b)Schematic of the deposition process of EB-PVD coatings [54].

2 Wm/K in commercial coatings systems [30]. Four basic processes rule the microstructure formation of in PVD techniques, they are namely shadowing, surface diffusion, volume diffusion and desorption [57]. In the EB-PVD process, first the chamber is pressurized to allow the electrons to travel from the electron gun to the evaporation material. Then electron bombarding against the material lead to an energy transfer to the material and evaporation.The evaporated material will then condensate in the substrate surface forming the coating. Condensation will be in the form of columnar grains on the substrate leading to better mechanical resistance than APS. Pores will be formed in the grain boundaries between columns that may lead to low conductivity but higher than in APS coatings.

1.3 Failure Mechanisms

Failure mechanisms of a thermal barrier coating can be severals, depending on the deposition methods, applications and operations. We could highlight generation of thermal stresses in the TBC system, Bond Coat oxidation, and the continuously changing microstructure, properties and morphologies of the contact interfaces in the coating systems.

Failure of TBC systems is highly complex and can not be completely described by a simple model. Stress generation due to oxidation, top and bond coat creep and thermal cycling yields to a progression of cracking. A model containing all these factors would be necessary to obtain a close description of the process [3][39]. Prediction ability of life time of thermal barrier coating systems and failure is of high priority for high-pressure gas turbine users, and development concentration is based on empirical steadies which relate the continuous damage to straining and oxidation of the coating [42].

Delamination is considered as the large separation of the TGO interface from the substrate or top coat due to mechanical effects while spallation is related to the when a small area separation of the coating system which is completely separated or removed from the rest of the system. In the image on Fig. 1.6 from [24] different mechanisms of damage that can lead to spallation are presented. Two types of spallation mechanisms can be considered depending on the stiffness of the thermal grown oxide compared with that of its interfaces, as shown in Fig. 1.6 a) and b); delamination in the interface is produced by buckling and by crack propagation through the top coat, respectively. Figure 1.6 c) shows spallation produced by cracking and propagation within the thermally grown oxide layer.

Spallation by buckling-delamination is the first delamination and occurs by formation of an horizontal crack in one of the TGO interface and propagated through the surface due to lower elastic stored strain energy in the interface than within the grown oxide layer. Then vertical cracks propagate along the top coat thickness leading to spallation, and this case is shown in Fig. 1.6 a). When spallation is induced by edge delamination, the opposite case is produced, first cracks appear with in the top coat and vertically propagate towards the TGO interfaces previously damaged leading to spallation, as shown in Fig. 1.6 b). In both of the cases the spallation of the ceramic layer will release the elastic stored strain energy of the system. When strain energy in the interface is higher than that of the TGO, micro-cracks will be formed within the top grown oxide layer and propagated along the layer, vertical cracks will be also formed in the ceramic coat and propagate along its thickness. Spallation will then occur when both cracks meet in the TGO (see Fig. 1.6 c)).

Maximum tensile stresses due to oxide growth have been found to be located in the top coat at the valley regions of the TGO-YSZ interface and TGO-BC interface at the protuberances, as a result of the thermo elastic mismatch strains and the continuity conditions of the TBC system. Sub-critical crack occur in locations near TGO interfaces where out of plane tensile strain is maximum and the values of these stresses are highly affected by the bond coat surface roughness. Effect of thermal loading are found to be in the reported on TGO interfaces and the tensile stresses increase with the increase in the BC roughness. The maximum stress reached in the top coat bond coat interface and the general TBC system can be highly underestimated if elastic isotropic behavior for the EB-PVD top coat is assumed [22].Thermally grown oxide formation

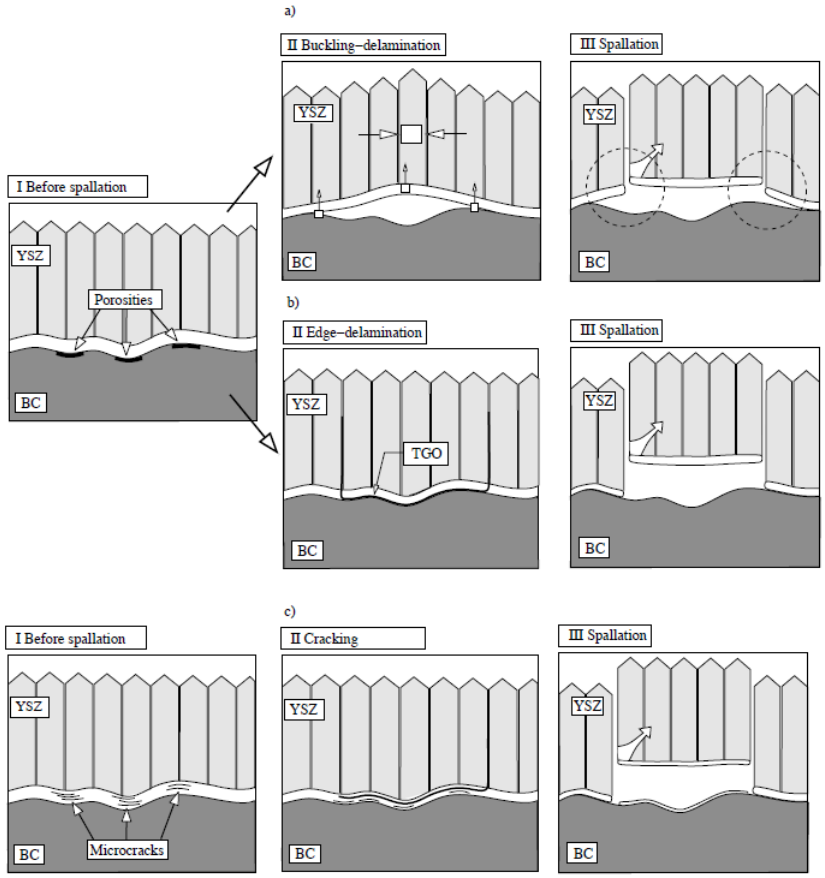

Figure 1.6: a) Representation of thermal barrier coating system structure, comprised of a nickel based superalloy, an aluminum rich bond coat, a thermal grown oxide(TGO) and a top coat thermal barrier coating(TBC). This figure represents the temperature profile inside the system during service of the engine. b) Conventional+fill gas cooled turbine coated by a TBC system [2].

is an important factor in the failure of the coating systems. Spallation is the typical associated mechanism of failure, and usually occur at the TGO interfaces where high tensile stresses concentration induced. Possible micro-cracks initiate in sites between TGO and BC [21]. Delamination models dealing with edge cracking and bulking can be considered but this models of failure are not critical, since zones with extended delamination is required to propagate cracks as been observed in the previous works. In this studies it is reported that failure is associated with some irregularities on the sinusoidal bond coat interface, and in sites of the TGO region where high tensile stresses occurred. Cracking was observed when computed compressive tensile stress is sufficiently high along more than the half of the TGO thickness [26].

Sintering deformation and tensile stress development due to creep and relaxation during cooling are responsible for surface cracks initiation in the TBC and propagation through its

thickness. Bending moment generated due to difference in thermal stresses along the top coat thickness, which generates tensile stresses normal to the top-coat-bond-coat interface leading to crack initiation and propagation in the interface, hence to delamination and structural failure. Surface cracks an TBC-BC interface cracks form independently [59][7]. As a result of some experiments, fracture resistance has been shown to increase with crack elongation, and fracture resistance curves were also noticed to be sensitive to the different layers thickness as well as the total TBC system thickness, increased resistance when similar properties where found along the coating system, and reduced with increasing properties differences [46].

1.4 Multi-scale Modeling Methods

Multi-scale model provides a tool for the construction of analytical and computational model to solve physical problems, combining existing and new developed fundamental principles, to bring under consideration different scales relevant in the problem, specially time and multiple length scales.[18] To approach the sintering, mud-craking and stress evolution precesses in the thermal barrier coating systems, is important to consider the material behavior along the numerous different scales. In order to complete continuum and atomistic analysis an understanding of matter structure at a continuous large scale and a discrete atomistic scale is demanded. Multi-scale model are designed to use particular descriptions of systems or materials at different levels to calculate properties of the system at a unique level, being able to coexist between microscopic and macroscopic properties of a material [33]. Multi scale modeling field has evolved in recent years from a descriptive to a predictive method for material and processes functions and properties. [17]. Direct multi-scale of sintering have been modeled studying the influence of internal parameters on the macroscopic contraction of a TBC system during sintering. Providing information in the unit cell internal structure evolution that is connected with the shape distortion resulting of macro and mesoscopic strain rates. [4].

1.4.1 Modeling of sintering

Previous direct multi-scale modeling studies of different viscous and diffusion mechanisms of constrained sintering samples conclude that kinetics of sintering differ for different material structures for both viscous and diffusion mechanisms not matter if the have the same level of porosity [4]. Micro-mechanics of sintering response on TBC systems and its effects and relation

with mud-craking phenomena is studied by Hutchinson in [48]. They found that mud-cracking can reveal in the coating due to in plane tensile stress and inter columnar sintering. Mud-cracking relives stress concentration and sintering is promoted between columns of the cluster. Mud-cracked openings grow due to sintering within columns of the cluster that can affect the performance of the coating system and lead to spallation of the top coat.

1.5 Structure of Thesis

In Chapter 2: First, the effect of sintering in an electron beam physical vapor deposited ceramic constrained layer is studied, EB-PVD lead to a columnar grain formation, and thus sintering evolution will be studied in the inter-columnar space. Observations demonstrated that in coatings with sufficiently large elastic modulus sintering was switch off, and that higher modulus were required to arrest large thermal mismatches. Stresses generated in the coating due to sintering and thermal loading can lead to mud-cracking formation. Thus the effect of mud-cracking on sintering process will now be studied, for a surface of fully developed square pattern of cracks. The obtained results will lead to observations of full sintering between layers for a mud-cracked surface with the same Young's modulus as a non cracked film where sintering was switched off, due to lower elastic constraints. Effect of the cluster arrangement dimensions showed that formation of smaller volume clusters or cross-sectional area show smaller elastic constrains and therefore lead to full sintering. Finally reduction af the model to one degree of freedom was possible due to steady inter-columnar diffusion of matter observation, highly reducing algebraic computation. High concordance of solutions was observed with the two degree of freedom problem.

In Chapter 3: Initially an analytical model to study stresses evolution during cooling in a three layer thermal barrier coating system will be developed. Continuity conditions of peel and shear stresses are applied due to perfect bonding assumption, stress free condition are also assumed due to lower stresses development at high temperatures during service. For thermal stress calculations constant isotropic materials properties and uniform temperatures along the system are used. The main purpose of the analytical work was to model the systems behavior during cooling and not to accurately calculate the stresses value. Thermal barrier coating systems are of high complexity, and limitations in characterization of the system were presented in analyt-

ical modeling. Therefore a computational model was developed to in a highest extend predict the stresses of the TBC system having into consideration effect of sintering evolution studied in chapter 2. Sintering is introduced in the top coat behavior by a material user subroutine of the computational software abaqus. First various sets of boundary conditions for the cases of uniform and non-uniform cooling, and sintering effect inclusion were studied to choose to most accurate set of BCs, and to understand the effect of non-uniform cooling and densification by sintering in the top coat are caused in the residual stress developed. Once the model is chosen and validated study of thermal oxide thickness effect in the stress evolution is studied in Chapter 4, furthermore the effect of creep and TGO growth at operating temperatures prior to cooling is considered for a more realistic prediction of stress evolution.

In Chapter 5 final conclusions are presented and future work proposed in the area is discussed.

CHAPTER 2

Inter-columnar Sintering in EB-PVD Coatings

2.1 Abstract

A micro-mechanical model in high-performance thermal barrier and protective coating systems using Electron Beam Physical Vapor Deposition EB-PVD is developed to simulate the sintering evolution of microstructure during service and eventual inter-columnar cracking in coatings. The model assumes that inter-columnar sintering is driven by changes in the potential energy of the applied stress and interface free energy of columns. The developed microscopic constitutive model will enable to predict system-level performance of such coatings systems, specifically for efficient turbine-based engine applications, by evaluating the sensitivity of the sintering response.

The inter-columnar microstructure is geometrically idealized for simplifications in calculations, and is assumed that the sintering rate of contact asperities is determined by diffusion along the interface. This investigation is aimed at developing advanced thermal barrier and protective coatings to ensure turbine sustainability at higher operating conditions. This involves a multilayer, multi-material coating system, which is intended simultaneously to provide oxidation, corrosion, foreign object erosion, wear and thermal barrier protection. Utilizing the new coating materials, processing parameters and design methodologies will be concurrently optimized to further increase the capabilities of these coating systems.

2.2 Problem Statement

Thermal barrier coating is a junction of multitude of layers, and these layers perform a defined function and show different properties and behaviors. Coating can be deposited over the substrate by different approaches, explained in Chapter 1. Electron beam physical vapor deposition is the commonly used process in turbine applications, even though it is more expensive than APS, exhibits greater thermal performance, leading to a columnar grain structure as shown in Fig. 2.1. Top coat behavior will be the principal source of study, especially sintering evolution and its effect in mud-cracking. During service the coating is subjected to a temperature gradient along its thickness. For simplification and better understanding of the coating behavior, isothermal case will be considered. As per described in [48], parallel columns result of the deposition process will be idealized to a have a square cross section of side d. Coordinate system and directions used throughout the model are x_1, x_2 and x_3, where x_1 and x_2 are normal to the column side surfaces in the coating plane, and x_3 is perpendicular to the plane directed to the top of the columns and starting with origin in the TGO-TBC interface. Smooth feather structure of the column surface acquired by deposition is almost smooth and an undulated surface of wavelength λ evolves in the surface. Amplitude growth of the undulated surface can lead to contact of adjacent columns. Columns will sinter together during service at high temperatures, and as a result of sintering, strains will be developed in the coating. A constitutive model is developed to study the sintering rate as a result of internal geometry evolution and stress induced in the coating.

An alternative micro-mechanical model, for progressive sintering, to the one developed in [48], especially provide insight in modeling constrained sintering and growing cracks by crevasse means. A different crack formation mechanism due to instabilities in the process of adjacent columns to sinter together leading to mud-craking, when the full sintering occur, will be approached in this study with some differences in geometries idealization that we believe have a closer behavior to the real sintering process . The main objective is to understand sintering in micro level to translate hardening in the top coat into the elastic properties of the YSZ top coat, and not to capture every detail of the sintering behavior. A 2 degrees of freedom model will be developed to capture the sintering evolution with respect to contact geometries and macroscopic strain generated in the coating. Identification of cracking occurrence evaluating different mate-

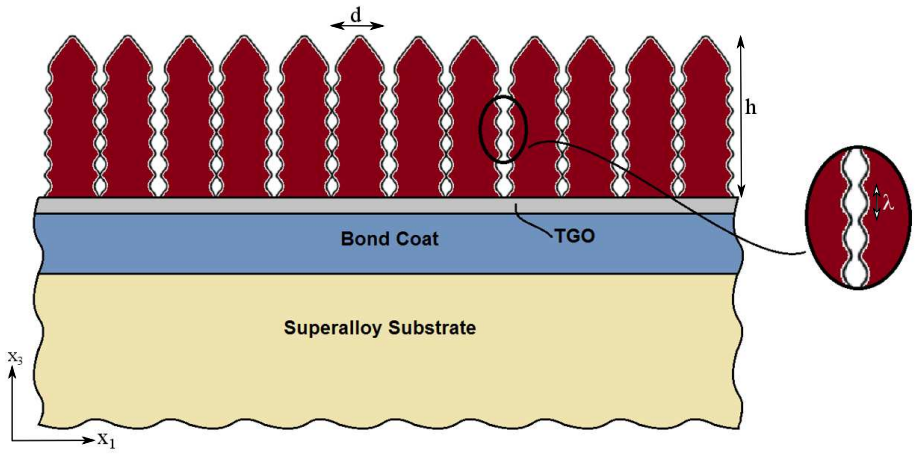

Figure 2.1: Schematic representation of a thermal barrier coating system of an electron beam physical vapor deposited yttria stabilized zirconia top coat, leading to formation of columnar grain structure.

rials and geometric conditions can be achieved under a 2DOF model. A wider study would be carried using a 3DOF model.

Two problems will be analyzed to explore the sintering response of a perfect Electron beam physical vapor deposited YSZ coating as follow,

- Intercolumnar sintering of infinite thermal barrier coating film of columns of cross-section dxd, as shown in Fig. 2.1.
- Intercolumnar sintering of a mud-cracked square cluster of side $2R$, as shown on Fig. 2.3.

2.3 Micro-structure

Electron Beam physical vapor deposition YSZ coatings are the most often used in high pressure gas turbines. EB-PVD lead to a columnar feathery morphology structure formation over the bond coat metallic layer, this layered microstructure permits thermal conductivity reduction. Exposure of parts to high temperature for longer periods lead to sintering evolution in the thermal barrier coating layer, densifying the coat.

Sintering occurs in two stages [60], the initial feathery morphology surface of the columns when deposited and develops an undulated surface with smother lines. The amplitude of the undulated waves grows until contact with the surrounding columns closing gaps between them, and

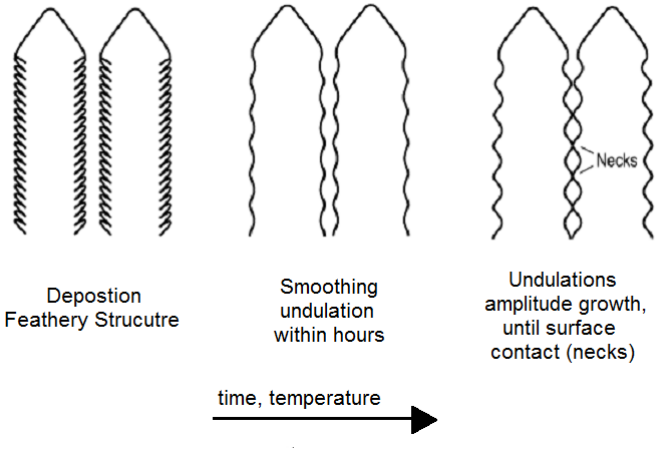

Figure 2.2: Sintering evolution on the microstructure of columns of EB-PVD coatings [60].

rows of local necks are formed along the columns. This necks formations encourage sintering of adjacent columns. Two steps sintering evolution on the column microstructure is demonstrated in Fig. 2.2

Bond coat undulations due to creep and thermal expansion coefficients mismatch affect the sintering evolution. In the perfect film case we will assume a straight and horizontal bond coat where columns are vertical and parallel to each other. After sintering of adjacent columns together, TBC layer can stand temperatures over 1400 ^oC for longer periods of time over 300 hours before cracking. A second case will be considered when rumpling evolves in the bond coat and mud-cracking occurs. Necks are formed in this case and undulations of the bond coat cause larger columns regions to sinter together, further this will cause formation of dens clusters with gaps between them.

Gaps formation between columns depend on the coefficient of thermal expansion mismatch between base and coating, when CTE of the base is higher than that of the coat columns tend to spread and hence gaps open up. When CTE is higher in the coating than in the base, the columns tend to approximate to each other and therefore smaller gaps occur between them. In the case of EB-PVD Yttria stabilized Zirconia over a Pt-Al bond coat where the coefficient of thermal expansion of the metallic bond coat is significantly higher than YSZ top coat, with values of 13.6 $10^-6/^oC$ and 9.0 $10^-6/^oC$ at room temperature respectively, gaps tend to open up. Poisson's ratio ν has been observed not to influence the sintering evolution of the system.

2.4 Progressive sintering of an uncracked EB-PVD YSZ layer

In this section, an analytical model to study the sintering evolution on a perfect semi-infinite film is developed. The coating is formed by parallel columns of square cross-section dxd and height H. It has been deduced in several computational studies that Poisson's ratio does not have influence in the evolution of sintering. Poisson's ratio is the coefficient of lateral over axial strain. In this study we assume an incompressible film and therefore is assumed to be $\nu = 0.5$, that will lead to simpler displacement film. Thus a better understanding of the process' physics will be captured.

2.4.1 Elastic Strain Energy

The coating can be considered as a semi-infinite film, due to its relative small thickness compared with the substrate thickness and the coating length, hence the total strain in the film is practically zero as presented in Fig. 2.1.

$$\varepsilon_S(x_3) + \varepsilon_T(x_3) + \varepsilon_E(x_3) = 0 \tag{2.1}$$

Where ε_T is the in-plane strain produced due to thermal expansion coefficient misfit between the ceramic coating and the nickel based superalloy substrate, and is calculated using Eqn. 2.2, where α_i are the CTE for the TBC and the substrate, T_D is the deposition temperature of the coating, T_{BC} is the temperature on the surface and $T(X_3)$ is the temperature of the TBC for a given instant and can vary with height. However the case of steady state will be considered with a given temperature profile.

$$\varepsilon_T = \alpha_{TBC}(T(x_3) - T_D) - \alpha_{BC}(T_{BC} - T_D) \tag{2.2}$$

And ε_S is the in plane sintering strain, generated by sintering due to the contact geometry evolution with time. In-plane sintering strain can be measured as the initial displacement of the columnar grain wall towards the adjacent column, means the total displacement u for the different instants of time divided by the half of the width of contact surface between columns for that instant of time d, as shown in Eqn. 2.3. Total distance u will increase with time and therefore for ε_S will be negative and decreases further. Variational principle will be used to calculate the sintering strain evolution proportional to the increasing contact geometry of the

adjacent columns.

$$\varepsilon_S = \frac{u_1 - u}{d} \tag{2.3}$$

$$\varepsilon_E = -\varepsilon_T + \varepsilon_S \tag{2.4}$$

Stress components in direction x_3 and shear stresses in the plane directions σ_{12} and σ_{21} will be canceled out, and in-plane stresses normal to direction x_1 and x_2 will become equal. Next, we used three dimensional Hooke's Law stress-strain relations for normal stresses (see Eqn. 2.5),and assumed the plane stress problem, approximating a two dimensional approach. Then substituting the equality stresses in the plane $\sigma_{x1} = \sigma_{x2}$, the in-plane stress where $i = x_1$ or $i = x_2$, E is the in-plane effective Young's modulus and ν is the Poisson's ratio of the film, are determined using Eqn. 2.6

$$\varepsilon_i = \frac{1}{E}(\sigma_i - \nu(\sigma_j + \sigma_k)) \tag{2.5}$$

$$\sigma_i = \frac{E}{1-\nu}\varepsilon_i^E \tag{2.6}$$

The unitary elastic stored energy for the different values of x_3 in the top coat can be calculated using the following relation:

$$U(x_3) = \sigma_i \varepsilon_i^E = \frac{E}{1-\nu}(\varepsilon_i^E)^2 \tag{2.7}$$

2.4.2 Contact Geometry

During sintering, first feathery structure acquired by the columnar grains surface after deposition into a wavy surface. The amplitude of the waves increases by growth until contact between neighboring columns takes place as seen in Fig. 2.2, leading to contact between two rough surfaces of wavelength λ. Farther sintering growth driven by diffusion bonding occurs. For simplification in the micro-mechanical modeling of sintering by inter-columnar contact evolution, as descried in [48], surface roughness of the surfaces is joined into a unique undulated surface considering the remaining surface as a perfectly flat. Idealization of the contact wavy geometry to the so called sawthooth inter-columnar contact shown in Fig. 2.3, will allow us

to develop an analytical model for the evolution of the intercolumnar contact geometry driven by sintering. The initial profile that describes the perfect situation to before the contact begins and is only introduced for calculation proposes but it can not be achieved in practice since sintering occurs not only in service but also during deposition. Contact $2b$ will be increased with time as sintering evolves and therefore amplitude of the rough surface decreases. Wavelength in the contrary will remain fixed until full-sintering occurs. Fig. 2.3 b) represents inter-columnar sintering evolution by u and w parameters, where sintering evolution between the walls is represented by u, roughness is denoted by w and wavelength by λ. Further assumptions are made on the level of roughness to be of the same order than feathery arms' length scale of the columns surface. Justifications are based on [60], where observation of the smoothen feathery surface occurs within hours after the coat is deposited.

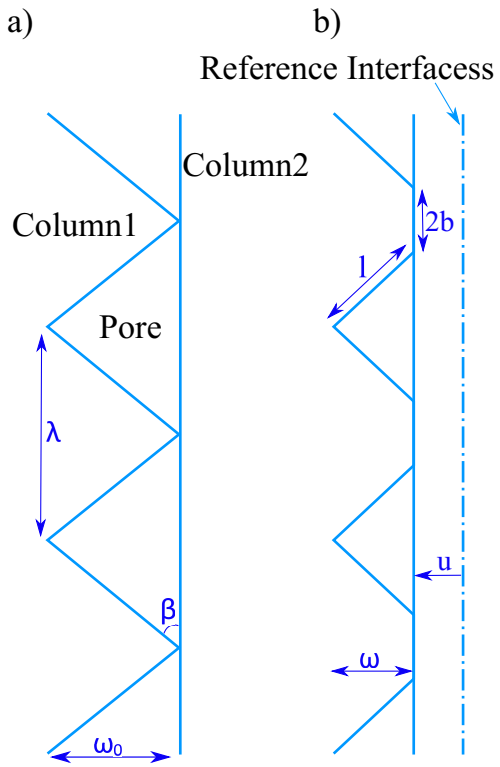

Figure 2.3: Schematic of the idealized contact geometry for analytical simplifications. a) Reference configuration prior to sintering where no strain has been evolved. b) Configuration at any instant, where displacement u of the assumed flat surface column with respect to the initial position of the other surface.

The objective of the current study is to model the surface structure evolution due to interfacial diffusion sintering, in which matter is diffused from the contact peaks into the empty pores, in terms of the unknowns u and w. The interfacial energy reduction and the previously

calculated potential energy of the system are the primary driving forces of the coating system.

Geometry relations will be identified to express the primary geometries of the contact surface b, l and β in terms of two unknowns (u, v), where d is half of the width of the contact point, l is the length of the saw-teeth side and β is the angle of the gap formed between the teeth and the supposed perfectly flat surface, and are given by, respectively:

$$b = \left(\frac{2u + w - w_0}{2w} \lambda \right) \tag{2.8}$$

$$l = \sqrt{w^2 + \left(\frac{\lambda (w_0 - 2u)}{2w} \right)^2} \tag{2.9}$$

$$\beta = \arctan \left(\frac{2w^2}{\lambda (w_0 - 2u)} \right) \tag{2.10}$$

2.4.3 Macroscopic Rate Potential

Rate potential ψ_λ considers the rearrangement of matter by diffusion over the rough surface of along the film. The potential is calculated as a function of the volumetric flux, as expressed in Eqn. 2.11. The flux is calculated and represented in the local coordinate system as shown in Fig. 2.4.

$$\psi_\lambda = \frac{d}{D_G} \int_0^b j^2(s_1) ds_1 + \frac{d}{D_S} \int_0^l j^2(s_2) ds_2 \tag{2.11}$$

Now observing sintering at the local level, matter diffusion occurs from the contact peaks into the free surface of pores connecting the peak with the valley of the saw-tooth where it is deposited. We used Fick's first Law that establishes a relation between the diffusive flux with the concentration gradient with direction from high to low concentration. For our case, the diffusive flux of the interface j $[m^2/s]$ and the gradient of chemical potential μ $[J/m^3]$ from high concentration peaks into low concentration pores, represented in Eqn. 2.12, where s is the length along the surface, and D $[Jm^6/s]$ is the diffusivity tensor of the column interface.

$$j = -D \frac{\partial \mu}{\partial s} \tag{2.12}$$

D is sensitive to temperature, and can be calculated using Eqn. 2.13, where δ is the thickness of the interface, Φ is atomic volume, k is the constant of Boltzmann, D_0 is the reference value

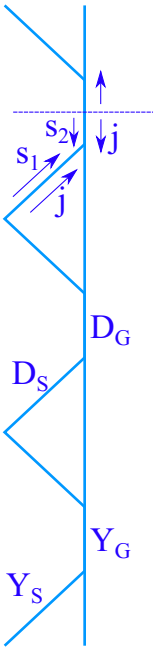

Figure 2.4: Schematic of the idealized geometry showing surface energies γ, diffusivities D and fluxes j and s.

of D for a given temperature and ΔE is the activation energy.

$$D = \frac{\delta\Phi}{kT} D_0 e^{-\Delta E/kT} \tag{2.13}$$

Continuity of mass has to be satisfied in the interface, and the normal velocity to the surface has to be equal to that of flux rate of the diffusing matter, such that:

$$\upsilon_n + \frac{\partial j}{\partial s} = 0 \tag{2.14}$$

Velocities normal to the surface s_1 and s_2 shown in Fig. 2.4 in terms of the unknown (u,w) and their derivatives, respectively, can be written as follows

$$\upsilon_n(s_1) = -\dot{u} \tag{2.15}$$

$$\upsilon_n(s_2) = -(\dot{u}+\dot{w})\cos\beta + \frac{s_2}{l}(\dot{w}\cos\beta + \dot{b}\sin\beta) \tag{2.16}$$

Introducing velocity equations in Eqn. 2.14, we can obtain the respecting fluxes:

$$j(s_1) = -\dot{u}s_1 \tag{2.17}$$

$$j(s_2) = (\dot{u}+\dot{w})s_2\cos\beta - \frac{s_2^2}{2l}(\dot{w}\cos\beta + \dot{b}\sin\beta) \tag{2.18}$$

where $\dot{b}$:

$$\dot{b} = \left(\frac{2\dot{u}w + \dot{w}(w_o - 2u)}{w^2}\right)\frac{\lambda}{2}$$

The condition of continuity of mass is satisfied since $j(s_1 = b) = j(s_2 = l)$ that is the common point in the peak corner of the idealized geometry. Now rate potential per unit volume defined as the height of a wave length λ and cross-section dxd.

$$\psi = \frac{\psi_\lambda}{d^2\lambda} \tag{2.19}$$

Introducing Eqn. 2.11, 2.17 and 2.18, in Eqn. 2.19:

$$\begin{aligned}\psi(\dot{w},\dot{u}) = {} & \frac{2\dot{u}^2b^3}{3d\lambda D_G} + \frac{2(\dot{u}+\dot{w})^2\cos^2(\beta)l^3}{3d\lambda D_S} + \frac{l^3}{10d\lambda D_S}\left[\dot{w}\cos\beta + \left(\frac{\lambda(w_0-2u)\dot{w}}{2w^2} + \frac{\lambda\dot{u}}{w}\right)\sin\beta\right]^2 \\ & - \frac{l^3(\dot{u}+\dot{w})\cos\beta}{2d\lambda D_S}\left(\dot{w}\cos\beta + \frac{\lambda\sin\beta}{2w^2}(w_0-2u)\dot{w} + \frac{\lambda\dot{u}\sin\beta}{w}\right)\end{aligned} \tag{2.20}$$

2.4.4 Gibbs Free Energy

Total Gibbs free energy for a volume of height λ and side d, Eqn.2.21 will be the sum of the interfacial energy reduction G_λ and the elastic stored energy, as previously calculated in Eqn. 2.7 for the slice.

$$G_{TOT} = G_\lambda + Ud^2\lambda \tag{2.21}$$

For a slice of thickness λ and cross-section dxd, the interfacial free energy G_λ will be:

$$G_\lambda = [2b\gamma_G + 2l\gamma_S + (\lambda - 2b)\gamma_S]2d \tag{2.22}$$

Where b and l are given by Eqn. 2.8 and Eqn. 2.9, respectively.

$$G_\lambda = \left[\frac{(2u+w-w_0)}{w}\lambda\gamma_G + 2\sqrt{w^2+\left(\frac{\lambda(w_0-2u)}{2w}\right)^2}\gamma_S + \left(1-\frac{(2u+w-w_0)}{w}\right)\lambda\gamma_S \right] 2d \tag{2.23}$$

Dividing the total energy by the volume of the representative slice volume, we obtain the Gibbs free energy per unit volume G:

$$G = \frac{G_\lambda}{d^2\lambda} + U \tag{2.24}$$

Introducing the values of the interfacial energy and the potential energy from Eqs. 2.23 and 2.4 respectively.

$$G = \left[\frac{(2u+w-w_0)}{w}\gamma_G + 2\sqrt{\frac{w^2}{\lambda}+\left(\frac{(w_0-2u)}{2w}\right)^2}\gamma_S + \left(1-\frac{(2u+w-w_0)}{w}\right)\gamma_S \right] \frac{2}{d} + \frac{E}{1-\nu}(-(\varepsilon_T+\varepsilon_s))^2 \tag{2.25}$$

Now differentiating G with respect to time, we obtain $\dot{G}$ Eqn. 2.26:

$$\begin{aligned} \dot{G} = {} & \frac{2(\gamma_G-\gamma_S)}{dw^2}(w(2\dot{u}+\dot{w})-\dot{w}(2u+w-w_0)) + \frac{2\gamma_S}{d}\sqrt{\frac{w^2}{\lambda}+\left(\frac{(w_0-2u)}{2w}\right)^2} \\ & \left(2w\dot{w}-\frac{(w_0-2u)(2\dot{u}w+\dot{w}(w_0-2u))}{2w^3}\right) - \frac{2E}{1-\nu}\left(\left(\varepsilon_T+\frac{u_1-u}{d}\right)\frac{\dot{u}}{d}\right) \end{aligned} \tag{2.26}$$

2.4.5 Variational Principle

A mathematical function Φ will be defined to account the effects of the rate of change with time of the system's Gibbs free energy $\dot{G}$ and the macroscopic rate potential Ψ, see Eqn. 2.27. Both of the expressions are in terms of the rates of evolution of the contact geometry, diffusion and displacement rate.

The solution obtained in practice among the different possible combinations of rates will be the one that leads to the minimum value of Φ, as proven in [55]. Hence Φ will be minimized to determine the present rate distribution. Other possibility to calculate the present velocities is by means of the moving interface partial differential equations, but sometimes lead to formidable calculations, deciding therefore to approach the problem using the thermodynamical variational principle method presented in [1] and [55]. However, PDE would exactly resemble the surface

evolution and TVP does an approximate analysis.

Focusing in the local sintering problem of wrinkle contact surface between neighbor columns on a length scale λ smaller than 1 μm, and slower diffusion over larger areas can be neglected, of the order of the sides of the column d (5-10 μm) or the height H ($\approx$ 200 μm). Therefore, we can neglect diffusion in the x_3 direction ($h >> \lambda$), and it can be solved for any value of x_3 and a fixed temperature T(x_3) for sintering strains evolution with time in directions 1 and 2.

$$\Phi(\dot{u},\dot{w}) = \dot{G}(\dot{u},\dot{w}) + \Psi(\dot{u},\dot{w}) \tag{2.27}$$

The minimal velocities for $\dot{u}$ and $\dot{w}$, will lead to variations of Φ in $\dot{u}$ and $\dot{w}$ equal to zero, that leaves two equations 2.28 and 2.29.

$$\frac{\partial\Phi(\dot{u},\dot{w})}{\partial\dot{u}} = \frac{\partial\dot{G}(\dot{u},\dot{w})}{\partial\dot{u}} + \frac{\partial\Psi(\dot{u},\dot{w})}{\partial\dot{u}} \tag{2.28}$$

$$\frac{\partial\Phi(\dot{u},\dot{w})}{\partial\dot{w}} = \frac{\partial\dot{G}(\dot{u},\dot{w})}{\partial\dot{w}} + \frac{\partial\Psi(\dot{u},\dot{w})}{\partial\dot{w}} \tag{2.29}$$

Where Gibbs free energy rate $\dot{G}$ is linear and rate potential Ψ is quadratic in $(\dot{v},\dot{w})$, Consequently Eqs. 2.28 and 2.29 can be expressed in the matrix form as shown in Eqn. 2.4.5:

$$\begin{pmatrix} \frac{\partial\Psi^2(\dot{u},\dot{w})}{\partial(\dot{u})^2} & \frac{\partial\Psi^2(\dot{u},\dot{w})}{\partial\dot{u}\partial\dot{w}} \\ \frac{\partial\Psi^2(\dot{w},\dot{u})}{\partial\dot{u}\partial\dot{w}} & \frac{\partial\Psi^2(\dot{u},\dot{w})}{\partial(\dot{w})^2} \end{pmatrix} \begin{pmatrix} \dot{u} \\ \dot{w} \end{pmatrix} = \begin{pmatrix} \frac{\partial\dot{G}(\dot{u},\dot{w})}{\partial\dot{u}} \\ \frac{\partial\dot{G}(\dot{u},\dot{w})}{\partial\dot{w}} \end{pmatrix}$$

2.4.6 Non-dimensionalisation

In order to minimize the number of variables and simplify calculations, we developed non-dimensionalized model. All the length scale variables will be normalized by the undulations wavelength λ, equations 2.30, 2.31, 2.32, 2.33 and 2.34

$$\bar{b} = \frac{b}{\lambda} \tag{2.30}$$

$$\bar{l} = \frac{l}{\lambda} \tag{2.31}$$

$$\bar{d} = \frac{d}{\lambda} \tag{2.32}$$

$$\bar{u} = \frac{u}{\lambda} \tag{2.33}$$

$$\bar{w} = \frac{w}{\lambda} \tag{2.34}$$

After normalizing the appropriate relations for non-dimensional time and material properties will be 2.35, 2.36, 2.37 and 2.38:

$$\bar{t} = \frac{D_S \gamma_S t}{\lambda^4} \tag{2.35}$$

$$\bar{D_G} = \frac{D_G}{D_S} \tag{2.36}$$

$$\bar{\gamma_G} = \frac{\gamma_G}{\gamma_S} \tag{2.37}$$

$$\bar{E} = \frac{E\lambda}{(1-\nu)\gamma_S} \tag{2.38}$$

Non-dimensional time resembles the sintering time dependence with the inverse quadratic wavelength. Values of the following variables are $\bar{d} = 20$, $\bar{D_G} = 1$ and $\bar{\gamma_G} = 0.68$ [23].

Once we normalize the different rates of the function Φ, the components of the matrix 2.4.5 lead to:

$$\frac{\partial^2 \Psi}{\partial \dot{\bar{u}}^2} = \frac{4\bar{b}^3}{3\bar{d}\bar{D_G}} + \frac{4\bar{l}}{3\bar{d}}\cos^2\bar{\beta} + \frac{\bar{l}^3}{5\bar{d}\bar{w}^2}\sin^2\bar{\beta} - \frac{\bar{l}^3}{\bar{d}\bar{w}}\cos\bar{\beta}\sin\bar{\beta} \tag{2.39}$$

$$\begin{aligned}\frac{\partial^2 \Psi}{\partial \dot{\bar{u}}\partial \dot{\bar{w}}} = \frac{\partial^2 \Psi}{\partial \dot{\bar{w}}\partial \dot{\bar{u}}} = \frac{4\bar{l}^3}{3\bar{d}}\cos^2\bar{\beta} + \frac{\bar{l}^3\sin\bar{\beta}}{5\bar{d}\bar{w}}(\cos\bar{\beta} + \frac{1}{2}\left(\frac{(\bar{w_0} - 2\bar{u})}{\bar{w}^2}\right)\sin\bar{\beta}) \\ - \frac{\bar{l}^3}{2\bar{d}\bar{w}}\cos\bar{\beta}\sin\bar{\beta} - \frac{\bar{l}^3\cos\bar{\beta}}{2\bar{d}}(\cos\bar{\beta} + \frac{1}{2}\left(\frac{(\bar{w_0} - 2\bar{u})}{\bar{w}^2}\right)\sin\bar{\beta})\end{aligned} \tag{2.40}$$

$$\begin{aligned}\frac{\partial^2 \Psi}{\partial \dot{\bar{w}}^2} = \frac{\partial^2 \Psi}{\partial \dot{\bar{w}}\partial \dot{\bar{u}}} = \frac{4\bar{l}^3}{3\bar{d}}\cos^2\bar{\beta} + \frac{\bar{l}^3}{5\bar{d}}(\cos\bar{\beta} + \frac{1}{2}\left(\frac{(\bar{w_0} - 2\bar{u})}{\bar{w}^2}\right)\sin\bar{\beta}) \\ - \frac{\bar{l}^3\cos\bar{\beta}}{2\bar{d}}(\cos\bar{\beta} + \sin\bar{\beta}\frac{1}{2}\left(\frac{(\bar{w_0} - 2\bar{u})}{\bar{w}^2}\right)\sin\bar{\beta})\end{aligned} \tag{2.41}$$

And the components of the vector ∂G in 2.4.5:

$$\frac{\partial \dot{G}}{\partial \dot{\bar{u}}} = \frac{4(\bar{\gamma_G} - 1)}{\bar{d}\bar{w}} + \frac{2}{\bar{d}}\left[\frac{-\bar{w_0} + 2\bar{u}}{\bar{w}^2\left(\bar{w}^2 + \frac{(\bar{w_0} - 2\bar{u})^2}{4\bar{w}^2}\right)^{1/2}}\right] - \frac{2\bar{E}}{\bar{d}}\left(\varepsilon_T + \frac{\bar{u_1} - \bar{u}}{\bar{d}}\right) \tag{2.42}$$

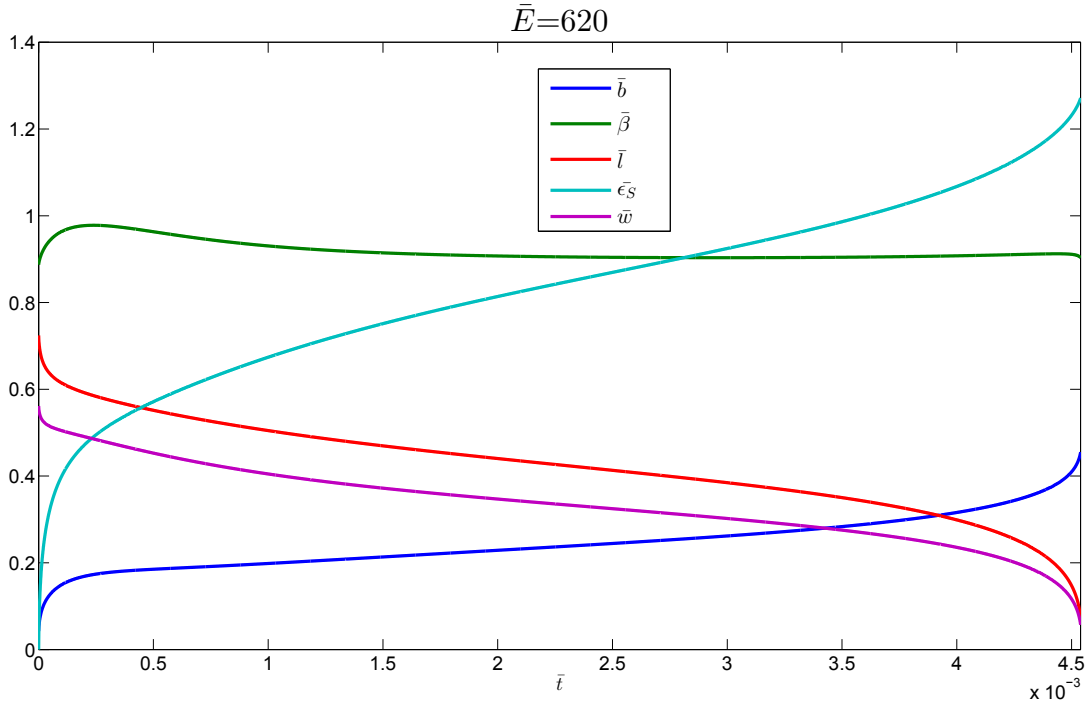

Figure 2.5: Evolution of contact geometry and sintering strain (%) with $\bar{t}$ for $\bar{E} = 620$ in a perfect film. The inclination is in radians. $\bar{E}$ and $\bar{t}$ are non-dimensional Young's modulus and time, respectively.

$$\frac{\partial \dot{G}}{\partial \dot{\bar{w}}} = \frac{2(\bar{\gamma_G} - 1)}{\bar{d}\bar{w}^2}(\bar{w} - (2\bar{u} + \bar{w} - \bar{w_0})) + \frac{2}{\bar{d}} \frac{\left(2\bar{w} + \frac{(\bar{w_0} - 2\bar{u})^2}{2\bar{w}^3}\right)}{\left(\bar{w}^2 + \frac{(\bar{w_0} - 2\bar{u})^2}{4\bar{w}^2}\right)^{1/2}} \tag{2.43}$$

2.4.7 Results

For initial values of $\bar{u_1} = 0.05$, $\bar{w_1} = 0.56$ and $\bar{w_0} = \frac{1}{2}\tan\bar{\beta}$, and solving the system of equations 2.4.5, two different behaviors were observed depending on the Young's modulus $\bar{E}$ value. Full sintering can be deduced straight forward from the idealized geometry as shown in Fig. 2.3 to be reached when $2b = \lambda$ then $\bar{b} = \frac{1}{2}$ and consequently the surface undulations amplitude reduce to zero. This leads to no further diffusion of matter from peaks to valleys of pores $\bar{w} = 0$ and increase to the saturation point of the sintering strain ε_S during the time interval. Magnitude of sintering strain reached at full sintering can be deduced from the expression of $\bar{b}(\bar{u}, \bar{w})$ Eqn. 2.8 and 2.30, then substituting these relations in the strain sintering Eqn. 2.3 we can obtain a final strain of $(2\bar{u_1} - \bar{w_0})/2\bar{d} = -1.3\%$. Full sintering was observed for lower magnitudes of $\bar{E}$ where the elastic resistance slower the sintering rate but does not arrest it.

An example is shown in Eqn. 2.5 for an elastic modulus of $\bar{E} = 620$ for the case of decrease

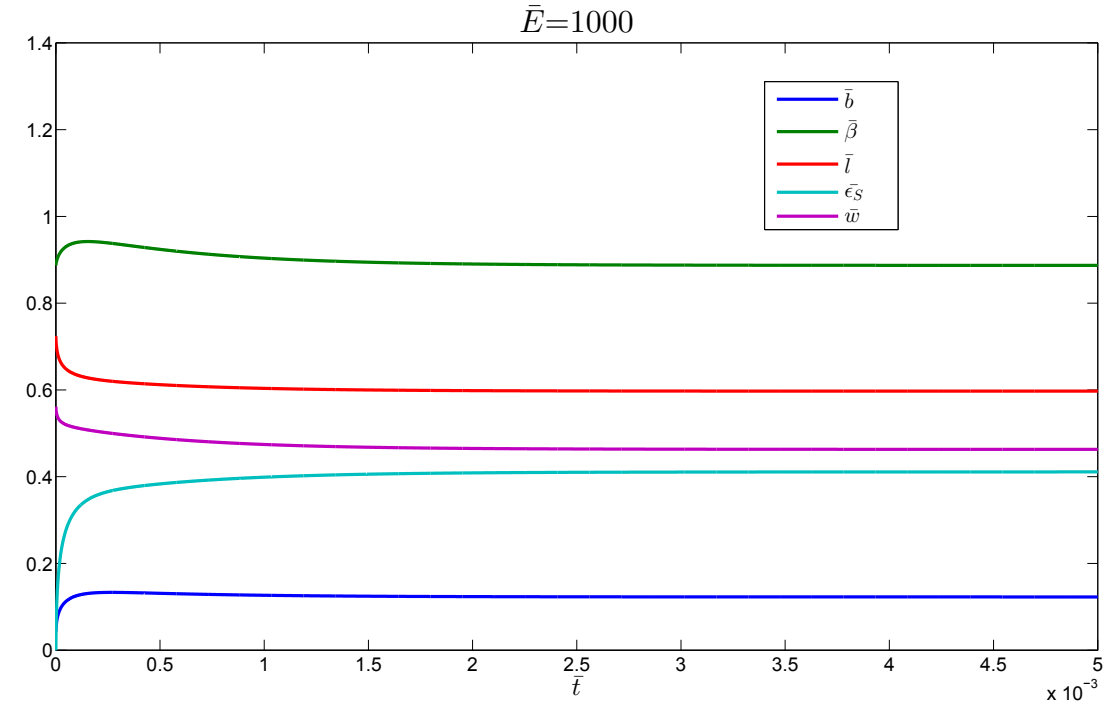

Figure 2.6: Evolution of contact geometry and sintering strain (%) with $\bar{t}$ for $\bar{E} = 1000$ in a perfect film. The inclination is in radians. $\bar{E}$ and $\bar{t}$ are non-dimensional Young's modulus and time, respectively.

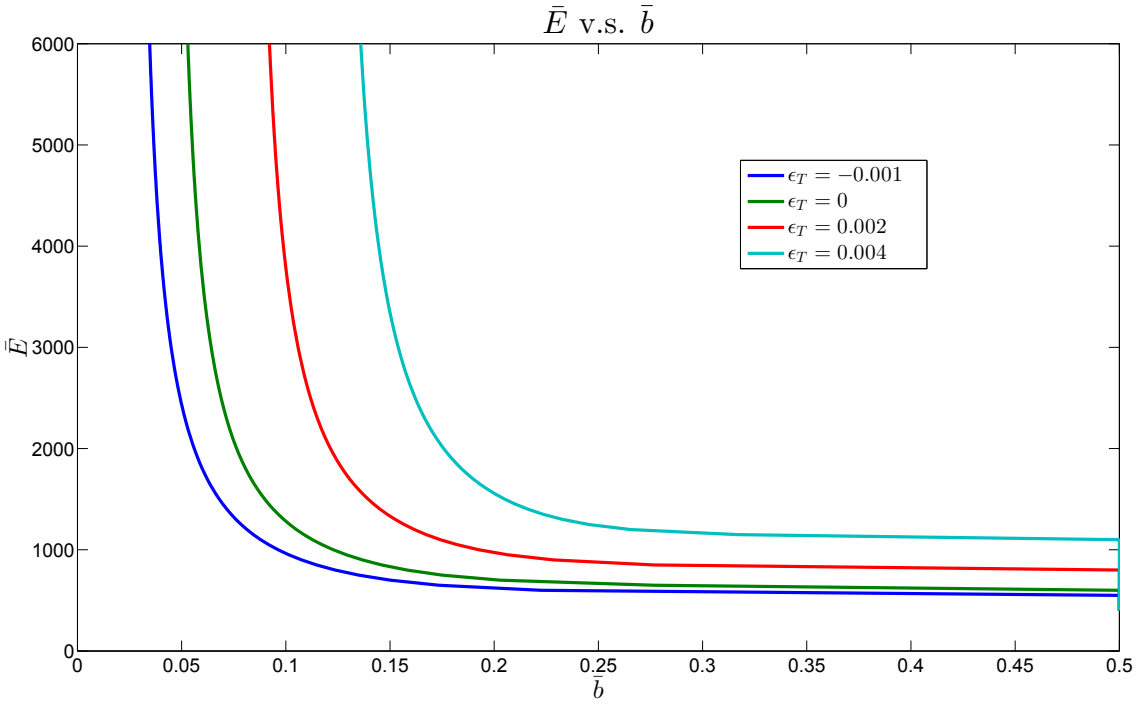

Figure 2.7: Represent final neck size $\bar{b}$.
as a function of the non-dimensionalized elastic modulus for the different thermal strains $\bar{\varepsilon_T}$.

of thermal strain ε_T. It may be observed from this figure, the values of $\bar{l}$ and $\bar{w}$ decrease gradually to zero and the magnitudes of the sintering strain ε_S and $\bar{b}$ reach their asymptotic values 1.3% and 0.5 respectively, while the roughness surface angle $\bar{\beta}$ tend to a steady state.

For stiffer coatings with larger values, sintering strain ε_T is observed to be switched off before saturated magnitudes are reached, in this case variables tend to steady state. Elastic strain energy rate in this case is sufficient to arrest later sintering stages. For example, for the case of Young's modulus of $\bar{E} = 1000$, decreased ε_T can be observed in Fig. 2.6, where values of $\bar{l}$ and $\bar{w}$ from the idealized contact geometry Fig. 2.3 decrease to a constant value grater than 0; and the values of ε_S and $\bar{b}$ asymptote to values lower to saturation respectively, and this shows the tendency of a trend to a constant value of the profile angle of the pores $\bar{\beta}$. It can also be noticed that the values of $\bar{\beta}$ in both the cases of lower and higher Young's moduli, have the pre-sintering initial values after deposition and similar qualitative response in the early sintering stages. However, lower elastic modulus presents opposite trend for sintering retarding the occurrence of full sintering while higher elastic modulus switch off the diffusion process prior to full sintering, leading to mud-cracking between the columns if the tensile states in the TBC are sufficiently high.

Final size of the contact points $\bar{b}$ as a function of the elastic modulus of the coating for different magnitude of thermal strains are presented in Fig. 2.7. Thermal strain ε_T has been neglected in previous cases studied above and it can be compared with the case of $\varepsilon_T = 0$ represented now , where we can observed how for values lower than $\bar{E} = 1000$, the neck size b tends to values of 0.5 hence to full densification. Fig. 2.7 illustrates that thermal strain in stiffer materials results in full sintering. Therefore, we can conclude that the stiffer coatings are required for higher thermal strains in the coating, and that can be translated into minimization of inter-columnar sintering by decreasing the thermal mismatch or increasing the in-plane Young's modulus of the coating.

2.5 Progressive sintering within a mud-cracked EB-PVD YSZ layer

Roughness of the metallic bond generate in plane stresses which create a pattern of gaps within the coatings after thermal cycles. These gaps seem to be boost by undulations of the Pt-Al bond

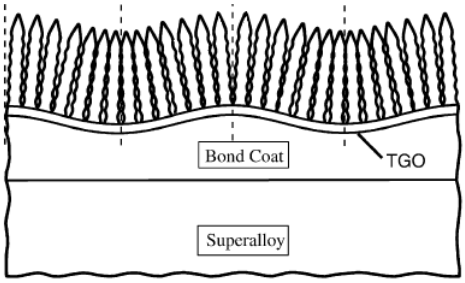

Figure 2.8: Schematic representation of a TBC system after EB-PVD YSZ and columnar grain formation, where effect of bond coat roughness is observed after the thermal cycling [60].

coat, as shown in Fig. 2.8. This in addition to sintering evolution narrows the distance between the columns in the valley regions leading to dens cluster formations with large gaps between [55]. The micrograph illustration shown in Fig. 2.9a) demonstrate the top view of a mud cracking pattern in a coating of YSZ layer. In plane tensile stresses are generated in the coating due to inter-columnar sintering. As presented in the previous section, this in-plane tension can arrest sintering process if its magnitude is sufficiently high, leading to mud-cracking between the columns in the coating layer. A fully developed mud-cracking pattern is assumed in the perfect film as per stated in [48]. The highly densified areas formed by groups of columns, called clusters, for computational simplification will be considered as square cross-section structure of size $2Rx2R$ and height H as illustrated in Fig. 2.10 a) and b). We did not consider circular cross-sectional clusters as described by Hutchinson because that will yields to potential energy changes. The cluster is stress free at its sides and upper surface, and the bottom is considered to be perfectly bonded to the thermally grown oxide surface. Due to traction free surfaces there will be a reduction in in-plane traction stress compared to the perfect film case. The drop in the elastic strain energy inside the arrangement is translated in smaller opposition to evolution of sintering. Hence, inter-columnar diffusion is promoted by mud-cracking phenomena. Idealized structure of the mud-cracked surface formed by several clusters, in which cluster is composed of a sum of columns as demonstrated in Fig. 2.10 a) and b) respectively.

For the calculation of the elastic strain energy stored in the mud-cracked coat, isothermal conditions will be assumed and therefore thermal strain $\bar{\varepsilon_T}$ will be uniform within the coatings. For simplification, the sintering strain $\bar{\varepsilon_S}$ will be considered uniform along the cracked TBC, but may change with the time. The deformation of the columns within the cluster will lead to a strain field distribution that can be approximated by the stored potential energy calculation. More accurate calculations can be done for nonuniform distribution of sintering and thermal strains,

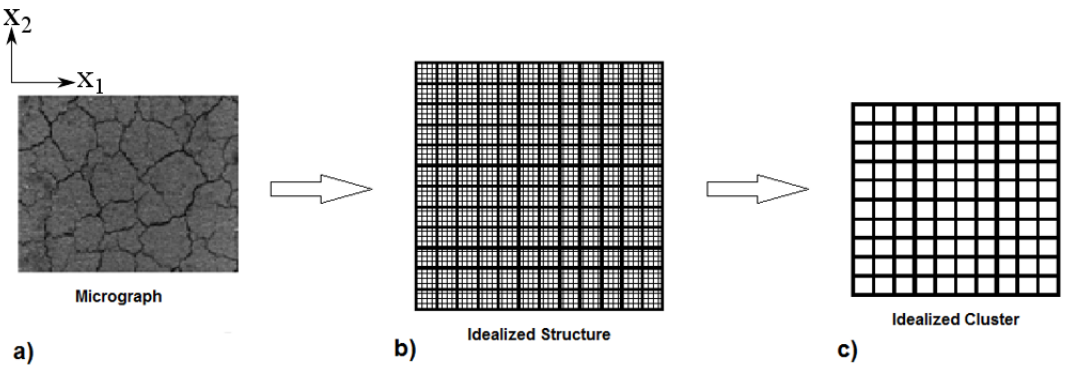

Figure 2.9: Idealization of the formed clusters in a mud-cracked matrix. a)Irregular cluster formation due to mud-cracking of the top coat can be observed in micro-graph, b)cluster structure is idealized to square shape ,and c)where each isolated cluster comprise of number of columns where further sintering takes place.

but computational labor will be increased. However, the objective of the study is to provide an analytical model to asses in the prediction and behavior of sintering after mud-cracking. Calculations of the local intercolumnar sintering at the microstructure level will for a mud-cracked layer will be equal to does previously calculated for an uncracked layer. Sintering will be initiated by free energy of the interface, for calculation of Gibbs free energy density G_λ. Dissipation will be driven by interfacial diffusion to calculate the rate potential Ψ as in the case of a uncracked layer. Consequently now applied to a single cluster of columns.

2.5.1 Elastic Strain Energy

In the calculation of the elastic stored train energy in the idealized squared cross-section cluster isothermal uniform conditions will be assumed in the arrangement. Stress free transformation strain and in-plane displacement constraints are imposed at the bottom of the cluster due to perfectly bounded supposition. Applying the so called Eshelby-type procedure mentioned in [48] we can obtain the following elastic components in the in-plane directions (x_1, x_2) for the bottom of the cluster x_3:

$$u_{x_1} = -(\varepsilon_T + \varepsilon_S)x_1 \tag{2.44}$$

$$u_{x_2} = -(\varepsilon_T + \varepsilon_S)x_2 \tag{2.45}$$

The coordinate system (x_1, x_2, x_3) is situated at the center of a cluster bottom. In the calculation of the elastic stored strain energy, it is found that the strain only occurs in a slice of

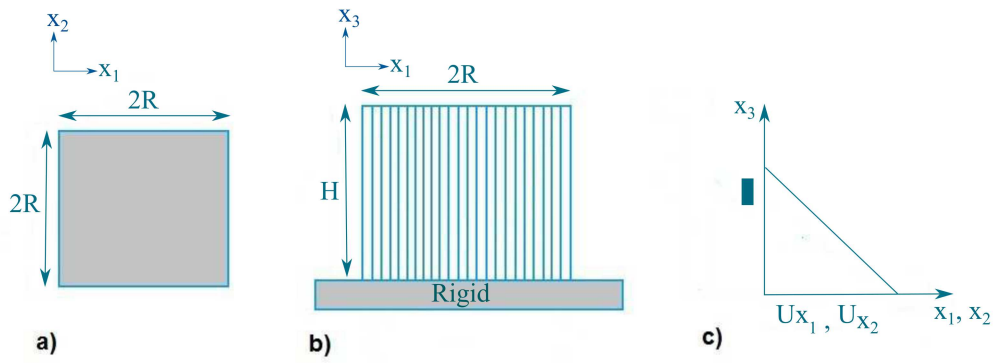

Figure 2.10: Illustration of an idealized square clusters of side 2R and height H. a)Top view of the isolated cluster, b)Lateral view of the cluster, Boundary conditions for a slice of height ζ where strain field will evolve.

the cluster of height ζ as presented in Fig. 2.9 c). Starting with Eqn. 2.44 and 2.45, we can obtain a kinetically feasible displacement field that satisfies the previously mentioned boundary conditions:

- $u_{x_1}(x_1,x_3) =$

$$-(\varepsilon_T+\varepsilon_S)\left(1-\frac{x_3}{\zeta}\right)x_1 \qquad if: \qquad 0<x_3<\zeta \tag{2.46}$$

$$0 \qquad if: \qquad \zeta<x_3<H \tag{2.47}$$

- $u_{x_2}(x_1,x_3) =$

$$-(\varepsilon_T+\varepsilon_S)\left(1-\frac{x_3}{\zeta}\right)x_2 \qquad if: \qquad 0<x_3<\zeta \tag{2.48}$$

$$0 \qquad if: \qquad \zeta<x_3<H \tag{2.49}$$

Strain components in the directions x_1 and x_2 are now calculated from displacements Eqs. 2.46 and 2.48:

$$\varepsilon_{x_1}=\frac{\partial u_{x_1}}{\partial x_1} \qquad\qquad \varepsilon_{x_2}=\frac{\partial u_{x_2}}{\partial x_2} \tag{2.50}$$

$$\varepsilon_{x_1}=-(\varepsilon_T+\varepsilon_S)\left(1-\frac{x_3}{\zeta}\right) \tag{2.51}$$

$$\varepsilon_{x_2} = -(\varepsilon_T + \varepsilon_S)\left(1 - \frac{x_3}{\zeta}\right) \tag{2.52}$$

Incompressibility conditions are assumed to find elastic strain Eqn. 2.53:

$$\varepsilon_{x_1} + \varepsilon_{x_2} + \varepsilon_{x_3} = 0 \qquad \varepsilon_{x_3} = -\varepsilon_{x_1} - \varepsilon_{x_2}$$

$$\varepsilon_{x_3} = 2(\varepsilon_T + \varepsilon_S)\left(1 - \frac{x_3}{\zeta}\right) \tag{2.53}$$

Introducing the elastic strain calculated from Eqn. 2.53 in $\varepsilon_{x_3} = \frac{\partial u_{x_3}}{\partial x_3}$, we can obtain the elastic displacement in the direction x_3 as follows:

- $u_{x_1}(x_1, x_3) =$

$$(\varepsilon_T + \varepsilon_S)\left(2 - \frac{x_3}{\zeta}\right)x_3 \qquad if: \qquad 0 < x_3 < \zeta \tag{2.54}$$

$$(\varepsilon_T + \varepsilon_S)\zeta \qquad if: \qquad \zeta < x_3 < H \tag{2.55}$$

Integrating the elastic strain field in the volume of the cluster for the different slices, the elastic stored strain energy of the cluster U_q is:

$$U_q = \frac{1}{2}\int_{-R}^{R}\int_{-R}^{R}\int_{0}^{\zeta}\sigma_{ij}\varepsilon_{ij}dV + \frac{1}{2}\int_{-R}^{R}\int_{-R}^{R}\int_{\zeta}^{H}\sigma_{ij}\varepsilon_{ij}dV$$

$$U_q = \frac{8ER^2}{3}(\varepsilon_T + \varepsilon_S)^2\left(1 - \frac{R^2}{6\zeta}\right) \tag{2.56}$$

Next we will choose the value of ζ in such way that it will minimize the elastic stored energy U_q, when $\frac{\partial U_q}{\partial \zeta} = 0$,Subsequently, we can obtain the optimal value that minimizes the elastic stored strain energy in the cluster as: $\zeta = \frac{R}{\sqrt{6}}$, assuming that $\zeta < H$. Now introducing in Eqn. 2.56 the following relation for the elastic energy we can write:

$$U_q = \frac{16ER^3}{3\sqrt{6}}(\varepsilon_T + \varepsilon_S)^2 \tag{2.57}$$

Dividing now by the reference volume $(2R)^2H$ and normalizing $\tilde{H} = \frac{H}{R}$ and $\bar{E} = \frac{E\lambda}{(1-\nu)\gamma_S}$ the elastic stored energy density will be obtained:

$$U_Q = \frac{4}{3\sqrt{6}}\frac{\bar{E}}{\tilde{H}}(\varepsilon_T + \varepsilon_S)^2 \tag{2.58}$$

It can be deduced that stored elastic energy density is reduced for the case of a mud-cracking TBC layer promoting the sintering process in the film. Full-sintering will be achieved in stiffer coatings.

2.5.2 Gibbs Free Energy

The inter-columnar local sintering problem will remain as stated in the previous section, and therefore the interfacial energy G_λ as well. Introducing Eqn. 2.24, new elastic stored energy where U is now U_Q, we can obtain the values of G and $\dot{G}$, respectively in Eqs. 2.59 and 2.60:

$$G = \left[\frac{(2u+w-w_0)}{w}\gamma_G + 2\sqrt{\frac{w^2}{\lambda} + \left(\frac{(w_0-2u)}{2w}\right)^2}\gamma_S + \left(1 - \frac{(2u+w-w_0)}{w}\right)\gamma_S\right]\frac{2}{d} + \frac{4}{3\sqrt{6}}\frac{\bar{E}}{\tilde{H}}(\varepsilon_T+\varepsilon_S)^2 \tag{2.59}$$

Now first normalizing using Eqs. 2.33, 2.34 and 2.32, and after differentiating Gibbs Free Energy G with respect to time, Gibbs Free Energy rate $\dot{G}$ can be expressed in terms of the variables $(\dot{\bar{u}}, \dot{\bar{w}})$ as obtained from Eqn. 2.26:

$$\begin{aligned}\dot{G} = {} & \frac{2(\gamma_G-\gamma_S)}{dw^2}\left(\bar{w}(2\dot{\bar{u}}+\dot{\bar{w}}) - \dot{\bar{w}}(2u+\bar{w}-\bar{w}_0)\right) + \frac{2\gamma_S}{d}\sqrt{\frac{\bar{w}^2}{\lambda} + \left(\frac{(\bar{w}_0-2\bar{u})}{2\bar{w}}\right)^2} \\ & \left(2\bar{w}\dot{\bar{w}} - \frac{(\bar{w}_0-2\bar{u})(2\dot{\bar{u}}\bar{w}+\dot{\bar{w}}(\bar{w}_0-2\bar{u}))}{2\bar{w}^3}\right) - \frac{4}{3\sqrt{6}}\frac{\bar{E}}{\tilde{H}}\left(\left(\varepsilon_T + \frac{\bar{u}_1-\bar{u}}{d}\right)\frac{\dot{\bar{u}}}{d}\right)\end{aligned} \tag{2.60}$$

2.5.3 Results

The thermodynamic variational principle will be applied in the case of a non mud-cracked layer, where the function Φ will be the union of the new Gibbs free energy rate. For the case of an isolated cluster and the previously calculated macroscopic rate potential Ψ, Eqn. 2.20, both of them can be expressed in terms of the rates of evolution of the local contact geometry $(\dot{\bar{u}}, \dot{\bar{w}})$. The same procedure will be followed, as per the previous case. Equations 2.28 and 2.29 will be expressed in the matrix form, where new values of $\frac{\partial \dot{G}}{\partial \dot{\bar{u}}}$ and $\frac{\partial \dot{G}}{\partial \dot{\bar{w}}}$ are expressed as below:

$$\frac{\partial \dot{G}}{\partial \dot{\bar{u}}} = \frac{4(\bar{\gamma}_G - 1)}{\bar{d}\bar{w}} + \frac{2}{\bar{d}}\left[\frac{-\bar{w}_0 + 2\bar{u}}{\bar{w}^2\left(\bar{w}^2 + \frac{(\bar{w}_0 - 2\bar{u})^2}{4\bar{w}^2}\right)^{1/2}}\right] - \frac{4}{3\sqrt{6}}\frac{\bar{E}}{\tilde{H}\bar{d}}\left(\varepsilon_T + \frac{\bar{u}_1 - \bar{u}}{\bar{d}}\right) \tag{2.61}$$

$$\frac{\partial \dot{G}}{\partial \dot{\bar{w}}} = \frac{2(\bar{\gamma}_G - 1)}{\bar{d}\bar{w}^2}(\bar{w} - (2\bar{u} + \bar{w} - \bar{w}_0)) + \frac{2}{\bar{d}}\frac{\left(2\bar{w} + \frac{(\bar{w}_0 - 2\bar{u})^2}{2\bar{w}^3}\right)}{\left(\bar{w}^2 + \frac{(\bar{w}_0 - 2\bar{u})^2}{4\bar{w}^2}\right)^{1/2}} \tag{2.62}$$

The rest of the terms, differentiation of the rate of potential Φ will remain the same as in the previous case, since the local inter-columnar problem is the same for both cases. Solving now the algebraic equations simultaneously for the initial conditions $\bar{u_1} = 0.05$, $\bar{w_1} = 0.56$ and $\bar{w_0} = \frac{1}{2}\tan\beta$. We can observe that solutions will depend on the dimensionless value of $\tilde{H}$ that represents the geometry of the formed cluster, and again that depends on the mud-cracking pattern. To study effect of mud-craking on the sintering evolution a value of $\tilde{H} = 1$ will be assumed and later we will study the effect of the cluster dimensions. Elastic thermal strain will be neglected for the simplifications in the prediction of sintering evolution but it will be observed consecutively how thermal strain will affect upon sintering. For example, results for Young's modulus magnitude $\bar{E} = 1000$ are illustrated in Fig. 2.11. We compared the obtained results in Fig. 2.6 with the values of $\bar{E} = 1000$ and $\varepsilon_T = 0$. In the case of perfect film the elastic stored strain energy was found to be enough to stop the evolution of sintering, while in the case of a mud-cracked surface the same elastic modulus is found to be not sufficient to arrest sintering. This due to the free stress surfaces of the arranged clusters, leading to inter-columnar full sintering. Sintering strain reaches the asymptotic value of 1.3%, neck size is equal to the initial wavelength λ and the amplitude $\bar{w}$ gradually goes to zero, meaning that both columns are sinter together. In the prediction of sintering evolution the assumption of $\varepsilon_T = 0$ was made for a better understanding of how the inter-columnar contact evolves. In Fig. 2.13, the final neck size b is represented for the different elastic moduli for the cases of increasing thermal strain. It can be observed that similarly as in the previous chapter, larger values of Young's modulus are required to arrest the sintering process for increasing thermal strain, but now higher modulus are required to switch off sintering for the same value of ε_T.

The value of $\tilde{H}$ was supposed to equal to 1 for simplification and better understanding of the prediction by considering $\bar{E} = 1000$, and dimensionless $\tilde{H} = \frac{H}{R}$; where R and H are values of the half side and height of the cluster, respectively. Final magnitudes of b in the case of different

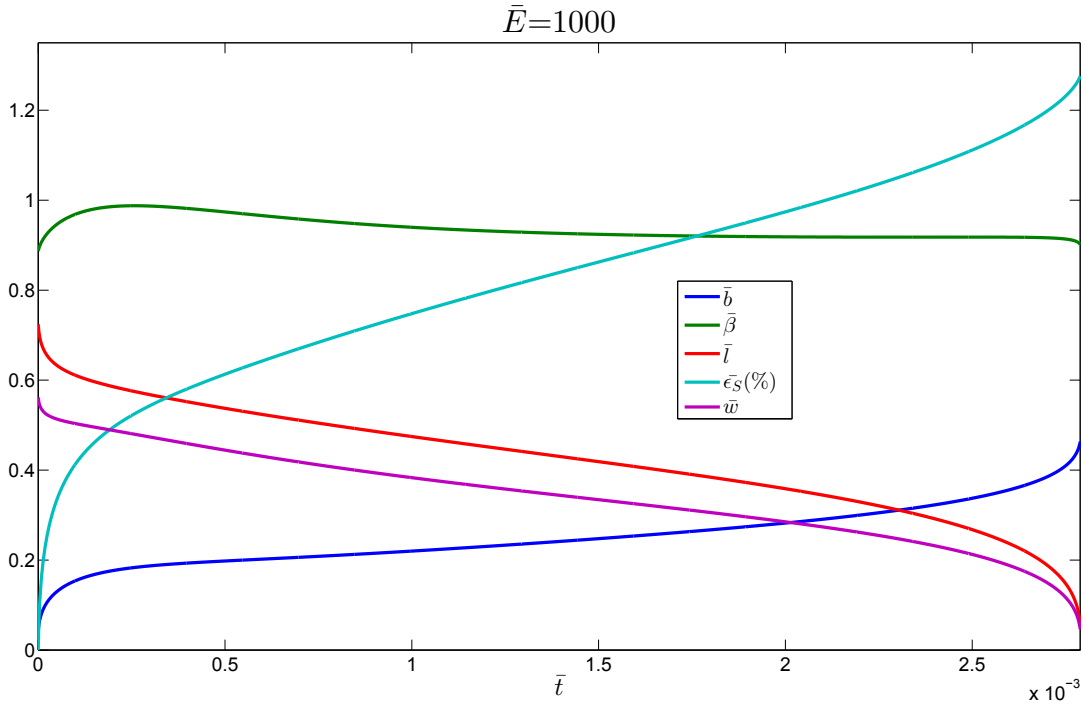

Figure 2.11: Evolution of contact geometry and sintering strain (%) with $\bar{t}$ for $\bar{E} = 1000$, for neglected thermal strain and non-dimensional $\tilde{H} = 1$ in a mud-cracked layer. The inclination is in radians. $\bar{E}$ and $\bar{t}$ are non-dimensional Young's Modulus and time respectively.

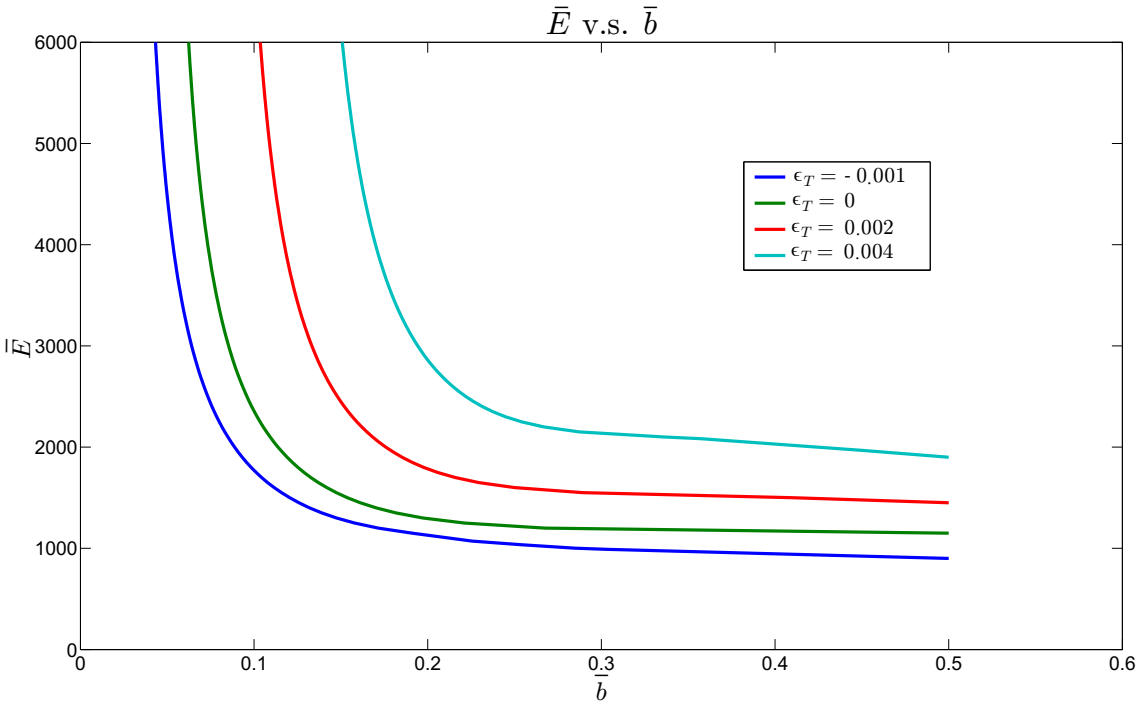

Figure 2.12: Final size of the contact neck b for several magnitudes of Young's modulus for increasing the values of thermal strain ε_T. Sintering is arrested for values of $\bar{b} < 0.5$.

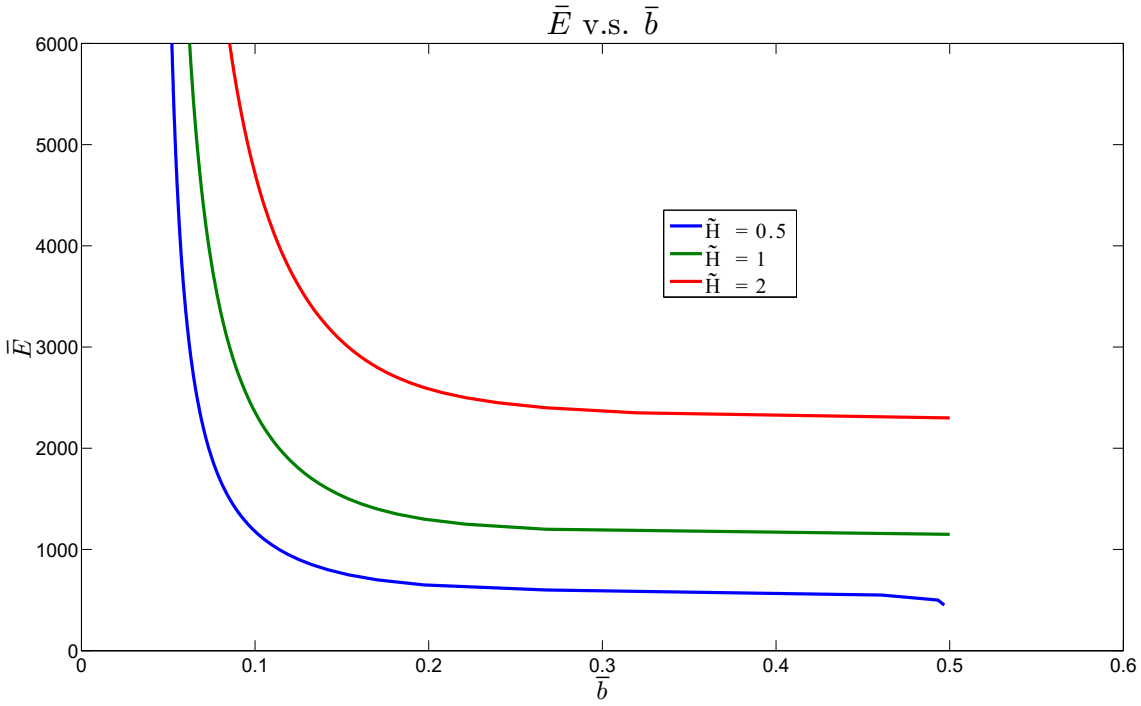

Figure 2.13: Final size of the contact neck b for several magnitudes of Young's modulus for increasing the values of non dimensional $\tilde{H} = \frac{H}{R}$. Sintering is arrested for the values of $\bar{b} < 0.5$.
1

Young's modulus for a range of $\tilde{H}$ are illustrated in Fig. 2.12, to understand the effect of the cluster size. $\tilde{H}$ can be increased by decreasing the side $2R$ or increasing H. From this figure, we can conclude that conformable non-dimensional $\tilde{H}$ results in stiffer coating because the elastic stored strain energy becomes sufficient to arrest sintering. We assumed that our coating is of constant height and there fore higher modulus will be required to switch off sintering for smaller cross-section clusters.

Values of the last neck size for several values of Young's modulus and non-dimensional $\tilde{H}$ are presented in Fig. 2.14. The red area represents when full sintering occurs within the TBC layer, yellowish area represent the elastic modulus and $\tilde{H}$ configures the full sintering initiation. It is observed that for low values of $\bar{E}$ and $\tilde{H}$ sintering is arrested in the coating, and higher elastic modulus are required to switch off sintering as the value of $\tilde{H}$ increases. The elastic strain energy limit values for which sintering process is arrested for a given elastic modulus can be observed. However, the main focus of this study is to illustrate the microeconomics importance of sintering and its direct relation with mud-craking. More accurate results would be necessary to predict the exact values at which changes occur.

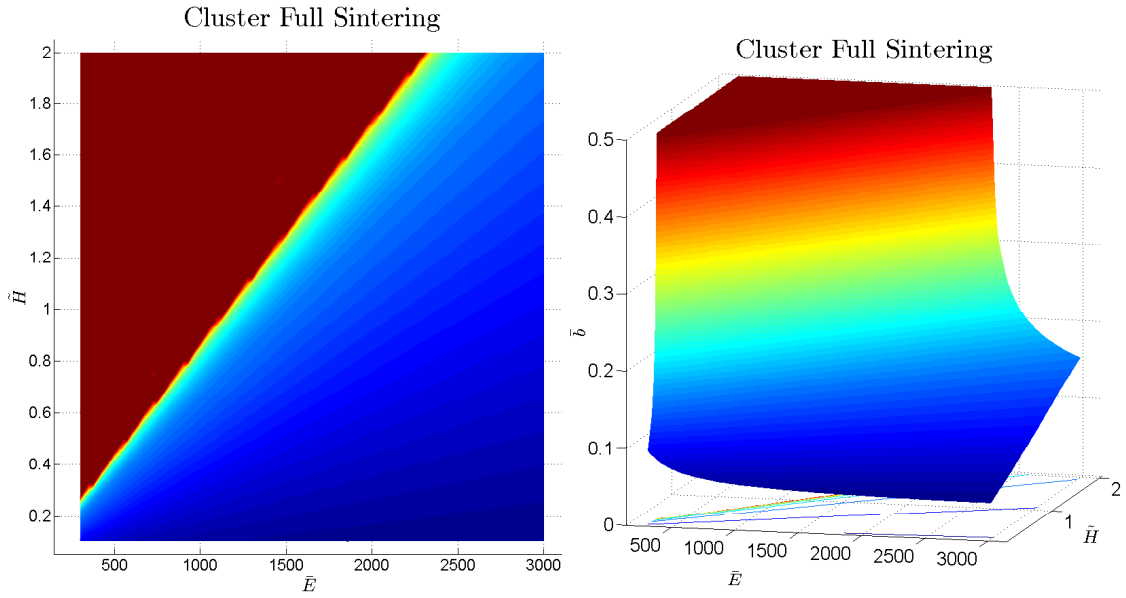

Figure 2.14: Interrelation between Young's modulus $\bar{E}$, non-dimensional $\tilde{H} = H/R$ and contact neck size for the case of an isolated columnar cluster of size *RxRxH* is presented. Full sintering occurs when $\bar{b} = 0.5$ that is denoted by the red area.

2.6 Reduction to One DOF

From the contact evolution with time of the inter-columnar surface, as presented in Fig. 2.5, 2.6 and 2.11. It can be observed that that the angle of the pore β (Fig. 2.3) quickly tend to constant value. Constant reduction of the amplitude ($\bar{w}$) with time, is driven by the thermodynamic force $\frac{\partial \dot{G}}{\partial \dot{\bar{w}}}$ and lead to the conclusion that the Gibbs free energy rate is optimal with $\dot{\bar{w}}$, therefore $\frac{\partial \dot{G}}{\partial \dot{\bar{w}}} \approx 0$. The constant value of equilibrium for the angles β is:

$$\cos\beta = \frac{1}{4}[(\gamma_G - 1) + ((\gamma_G - 1) + 8)^{1/2}] \tag{2.63}$$

Therefore the problem can be reduced to one degree of freedom(u). From the contact geometry variable β (see Eqn. 2.10), w can be expressed in terms of u and the contact angle that is now approximated to its equilibrium value. And now we can substitute w in the rest of algebraic expressions, leading to only one unknown u.

$$w = \sqrt{\frac{1}{2}\tan\beta(\lambda(w_0 - 2u))} \tag{2.64}$$

Applying thermodynamic variational principal to the new function Φ and representing the sys-

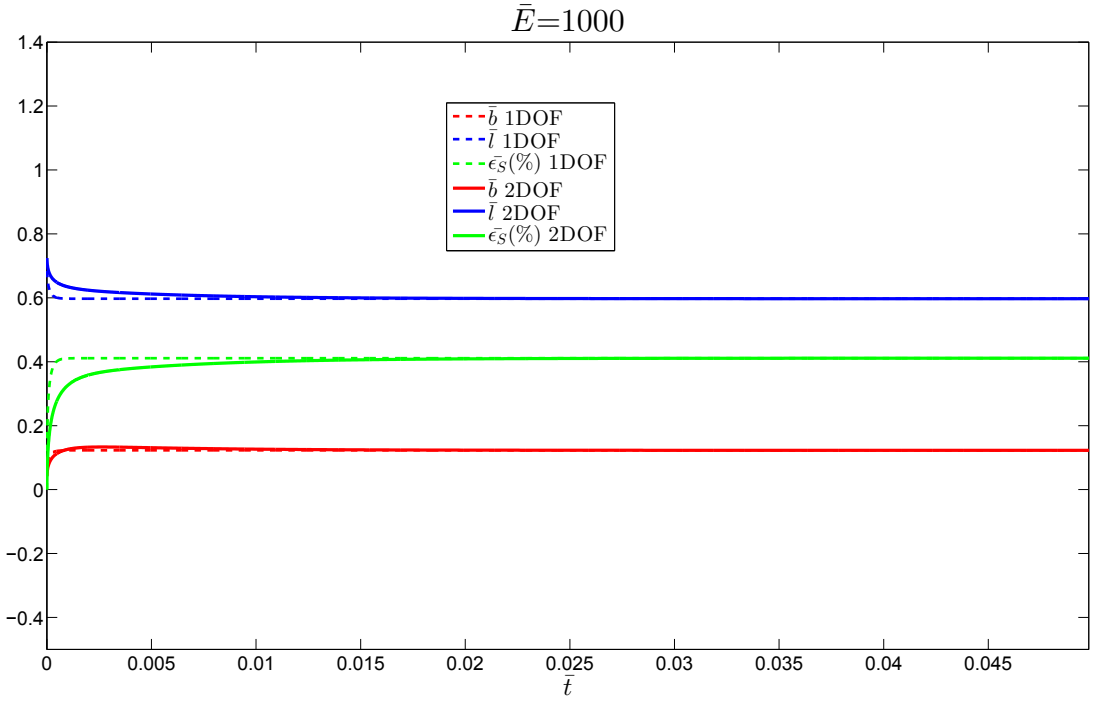

Figure 2.15: Sintering contact evolution of a perfect film of Young's modulus $\bar{E} = 1000$, comparing the case of 2 degrees of freedom with the simplification to 1 degree of freedom.

tem in the matrix form, we can observe how the problem can be solved.

$$\begin{pmatrix} \frac{\partial \Psi^2(\dot{u},\dot{w})}{\partial(\dot{u})^2} & 0 \\ 0 & 0 \end{pmatrix} \begin{pmatrix} \dot{u} \\ \dot{w} \end{pmatrix} = \begin{pmatrix} \frac{\partial \dot{G}(\dot{u},\dot{w})}{\partial \dot{u}} \\ 0 \end{pmatrix}$$

Where the different components can be obtained introducing $\bar{w}$ (Eqn. 2.64) in the rate potential and Gibbs free energy rate equations for the cases of perfect film and mud-cracked coating. Same initial conditions that in the previous sections will be applied compared with the case of two DOF and validate the reduction to one degree of freedom. $\bar{w_1} = 0.56$ and $\bar{w_0} = 0.887158057$. The case of a non-cracked perfect film and a mud-cracked layer are presented in Fig. 2.15 and 2.16, respectively, for the cases of 2 DOF and 1 DOF, it can be concluded that the reduction is satisfactory, highly simplifying the algebraic calculation time.

During cooling of gas turbine engines to room temperature condition, in-plane tensile stress is developed in the YSZ layer and mud-cracking can frequently be observed in the coating due to the build-up stress. We can discus now that mud-cracking is due to in-plane stresses generated by inter-columnar sintering within the coating. It can be further affirmed that cluster formation

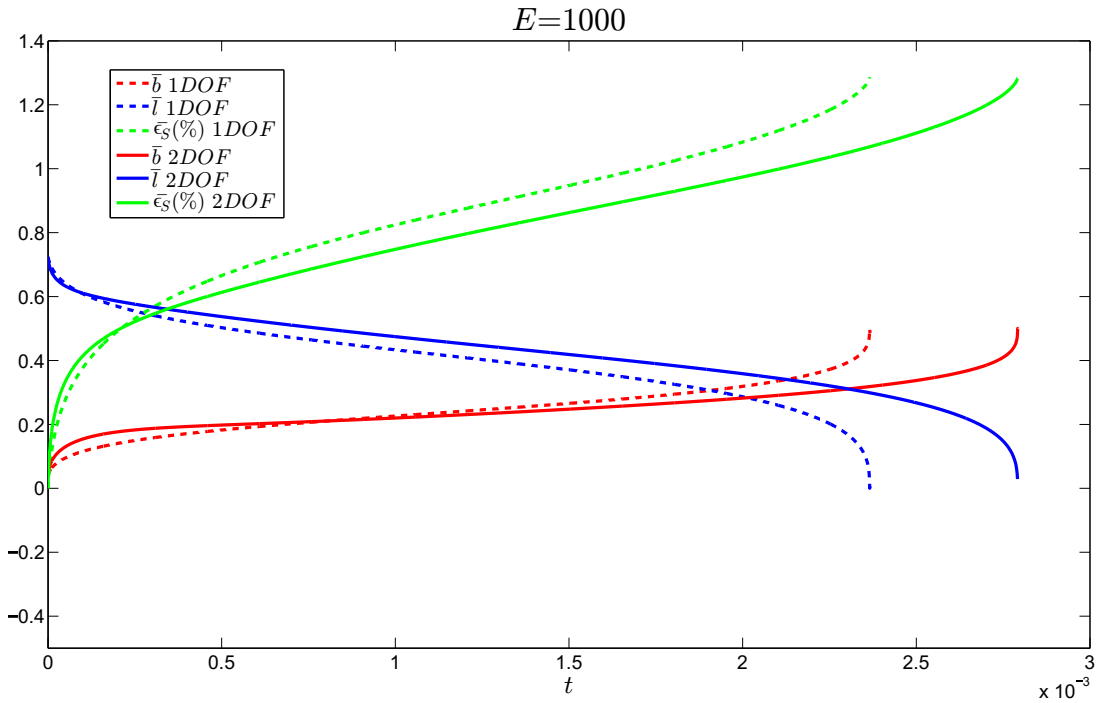

Figure 2.16: Sintering contact evolution of an isolated cluster of Young's modulus $\bar{E} = 1000$, comparing the case of 2 degrees of freedom with the simplification to 1 degree of freedom.

accelerates the sintering process, requiring the stiffer materials to arrest sintering. Hardening of the coating is produced by densification due to sintering. In the following chapters taking into consideration densification and hardening of the coating due to sintering, considering the mismatch between thermal strain, stress evolution will be studied along the TBC system.

CHAPTER 3

Modeling of Thermal Stresses

During service no mechanical loads are applied to the gas turbine components, but they are exposed to a very high temperatures producing residual thermal stresses in the coating system, and that can lead to cracking and spallation of the coating. When spallation occurs the nickel based superalloy component surface is exposed to temperatures above its melting point leading to imminent failure. In this chapter thermal stresses developed in EB-PVD yttria stabilized zirconia thermal barrier coating systems will be modeled, and the importance of including the different internal mechanisms will be studied.

3.1 Analytical Model

In this section an analytical model to study stress evolution in a three layer system prior to bond coat oxidation will be developed. Perfect bonding between the layers with plane interface between them in a semi-infinite film will be considered. Variational principal will be used for the calculation of stresses within the coating.

3.1.1 System

The system under study is a three layer system composed by a nickel based superalloy substrate of height h_{SUB} protected by a corrosive and oxidizing resistance metallic bond coat of height h_{BC} and thermally insulted by a ceramic top coat of height h_{TBC}. In the following calculation,

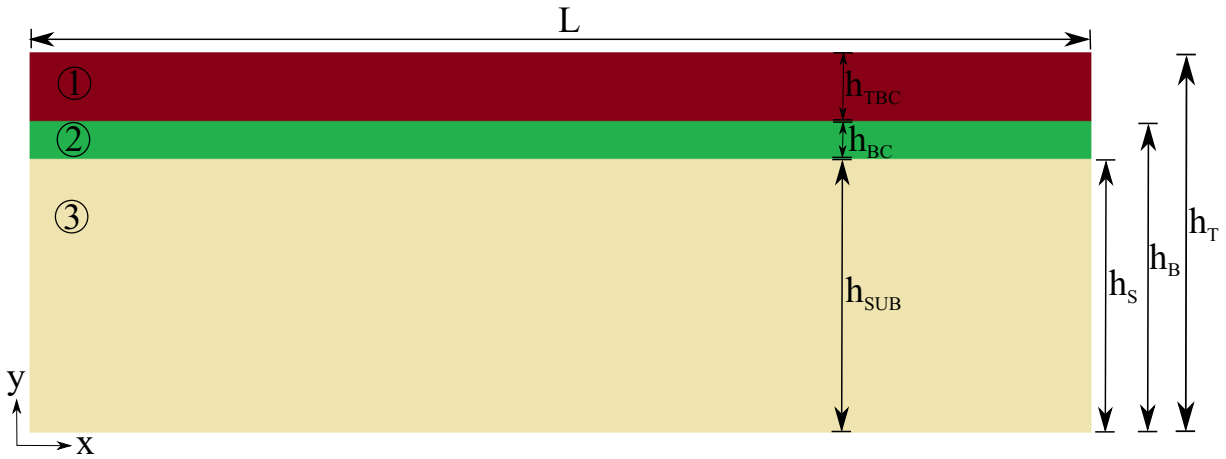

Figure 3.1: Schematic of the thermal barrier system used in the model. Dimensions are given in table 3.1.4.

stresses in the TBC will be denoted by 1, those of the bond coat they will be denoted by a 2 and the stresses in nickel superalloy substrate will be denoted by 3. Schematic of the thermal barrier system is shown in Fig. 3.1 and its dimensions are given in table 3.1.4,

3.1.2 Boundary Conditions

Continuity conditions of out of plane and shear stresses between consecutive layers, and free stress systems are considered to model the stress field:

- Stress-free condition:
  - $\sigma_{xy}^{(1)}(x,h_t)=\sigma_{yy}^{(1)}(x,h_t)=\sigma_{xy}^{(3)}(x,0)=\sigma_{yy}^{(3)}(x,0)=0$
- Out of plane stress continuity condition:
  - $\sigma_{yy}^{(1)}(x,h_b)=\sigma_{yy}^{(2)}(x,h_b)$
  - $\sigma_{yy}^{(2)}(x,h_s)=\sigma_{yy}^{(3)}(x,h_s)$
- Shear stress continuity condition:
  - $\sigma_{xy}^{(1)}(x,h_b)=\sigma_{xy}^{(2)}(x,h_b)$
  - $\sigma_{xy}^{(2)}(x,h_s)=\sigma_{xy}^{(3)}(x,h_s)$

The stress components are different in the coating systems as follows,

- Top Coat: $\sigma_{xx}^{(1)}(x)$, $\sigma_{xy}^{(1)}(x,y)$, $\sigma_{yy}^{(1)}(x,y)$

- Bond Coat: $\sigma_{xx}^{(2)}(x)$, $\sigma_{xy}^{(2)}(x,y)$, $\sigma_{yy}^{(2)}(x,y)$
- Substrate: $\sigma_{xx}^{(3)}(x,y)$, $\sigma_{xy}^{(3)}(x,y)$, $\sigma_{yy}^{(3)}(x,y)$

3.1.3 Stress Field

First approach we made is state of equilibrium for the thermal barrier coating system, and two dimension continuum differential equations have to be satisfied in order to accomplish the equilibrium condition.

$$\frac{\partial \sigma_{xx}^{(i)}}{\partial x} + \frac{\partial \sigma_{xy}^{(i)}}{\partial y} = 0 \tag{3.1}$$

$$\frac{\partial \sigma_{xy}^{(i)}}{\partial x} + \frac{\partial \sigma_{yy}^{(i)}}{\partial y} = 0 \tag{3.2}$$

Using the equilibrium conditions given by Eqs. 3.1 and 3.2, and the boundary conditions, all the stress components in the assembly are calculated in terms of stresses in the bond coat.

- $\sigma_{xx}^{(1)}(x)$=$\sigma_{TBC}(x)$=σ_{TBC}
- $\sigma_{xx}^{(BC)}(x)$=$\sigma_{BC}(x)$=σ_{BC}

Top Coat

The stress in the longitudinal direction on the top coat is one of the unknown of our system of differential equations:

$$\sigma_{xx}^{(1)}(x) = \sigma_{TBC} \tag{3.3}$$

From Eqn. 3.1 and free-stress condition at $y = h_t$, shear stress in top coat results in

$$\sigma_{xy}^{(1)}(x,y) = (h_t - y)\sigma'_{TBC} \tag{3.4}$$

Using the equilibrium Eqn. 3.2 and applying again the stress-free condition in $y = h_t$ for the thermal barrier coat surface, we obtain:

$$\sigma_{yy}^{(1)}(x,y) = \frac{1}{2}(h_t - y)^2 \sigma''_{TBC} \tag{3.5}$$

Bond Coat

The stress component in the longitudinal direction in the metallic layer where the thermal barrier coating is deposited can be written as follows:

$$\sigma_{xx}^{(2)}(x) = \sigma_{BC} \tag{3.6}$$

From equilibrium Eqn. 3.1 equilibrium equation and the condition of shear stress continuity between bond coat and thermal barrier coat at $y = h_b$, shear stress in the bond coat is:

$$\sigma_{xy}^{(2)}(x,y) = h_{TBC}\sigma_B C' + (h_{BC} - y)\sigma' \tag{3.7}$$

where $h_{TBC} = (h_t - h_b)$

Equilibrium Eqn. 3.2 and out of plane stress continuity is now used to calculate out of plane stress in the bond coat:

$$\sigma_{yy}^{(2)}(x,y) = \frac{1}{2}[h_{TBC}^2 + 2h_{TBC}(h_b - y)]\sigma''_{TBC} + \frac{1}{2}(h_b - y)^2\sigma''_{BC} \tag{3.8}$$

Substrate

Global equilibrium of forces is now applied to obtain longitudinal stress in the substrate, no external load is applied to the turbine component therefore the sum of the stresses in the different layers is equal to zero:

$$0 = \sigma_{SUB} + \frac{y_t - h_b}{h_s}\sigma_{TBC} + \frac{h_b - h_s}{h_s}\sigma_{BC}(x) \tag{3.9}$$

For simplification:

$$\lambda = \frac{y_t - h_b}{h_s} \tag{3.10}$$

$$\gamma = \frac{h_b - h_s}{h_s} \tag{3.11}$$

The longitudinal stress in the substrate can be expressed as:

$$\sigma_{SUB} = \sigma_{xx}^{(3)} = -\lambda\sigma_{TBC} - \gamma\sigma_{BC}(x) \tag{3.12}$$

Differentiating Eqn. 3.12 with respect to x and substituting $\frac{d\sigma_{SUB}(x)}{dx} = \sigma'_{SUB}$ into the first equilibrium Eqn. 3.1, and then differentiating the resulting expression with respect to y, we obtain,

$$\frac{\partial^2\sigma_{xy}^{(3)}}{\partial y^2} = 0 \tag{3.13}$$

Integrating the above equation twice with respect to y, and introducing the shear stress continuity condition at $y = h_s$, interface between substrate and bond coat, and the stress-free condition on the substrate, the following expression is obtained,

$$\sigma_{xy}^{(3)}(x,y) = [\lambda\sigma'_{TBC} + \gamma\sigma'_{BC}]y \tag{3.14}$$

Using the expression for $\sigma_{xy}^{(3)}$ in Eqn. 3.2 and following the same procedure used for shear stress, the expression for out of plane stress is given by

$$\sigma_{yy}^{(3)}(x,y) = -[\lambda\sigma''_{TBC} + \gamma\sigma''_{BC}]\frac{y^2}{2} \tag{3.15}$$

3.1.4 Energy and Variational principle

In this section the complementary energy functional in the system will be obtained using the stress components for the different layers earlier calculated in the stress field section. In order to obtain the unknown stresses σ_{TBC} and σ_{BC}, variational method will be used. In general terms variational principal is used in the calculus of variations, developing general methods to find a function or functions that minimize or maximize a measurement that depend on those functions. For the formulation of Thermodynamic Variational Principle there are two ways to approach the problem, either assuming a field of infinitesimal displacement along with the principle of minimum potential, or assuming small variation on the stress field in conjunction with complementary energy theorem [51] In the principle of minimum potential, used in Chapter 2, the displacement field among a family of admissible displacement fields that minimizes the potential energy of the system is obtained. For the case of complimentary energy theorem, that will be used in the calculation of stresses with in the TBC system, the purpose is to obtain the

field stress among a family of feasible stress fields which minimizes the complimentary energy Π [47] [11].

In order to model the stress evolution in a EB-PVD TBC system, the solution for the unknown stresses σ_{TBC} and σ_{BC} which minimize the complimentary energy of the system is found. The feasible stress states will be those which satisfy continuity equilibrium equation, stress free boundary conditions of the system and continuity of stresses along the plain perfectly bounded interfaces. The solutions of the functional are those values of σ_{TBC} and σ_{BC}, for which the complimentary energy is minimum, called real stress state. Once the unknowns are calculated the rest of stresses expressed in the previous section in terms of the unknown will be obtained.

The complementary energy of the thermal barrier coating system Π, is given by the sum of the complementary energy for the different layers:

$$\Pi = \Pi_1 + \Pi_2 + \Pi_3 \tag{3.16}$$

where Π_1 is the stored energy of the ceramic top coat, Π_2 is the complementary energy of the metallic bond coat, and Π_3 is the complementary energy of the nickel superalloy substrate.

Complimentary energy general for Π_i (i=1,2,3) for a linear thermo-elastic material is given by the following equation:

$$\Pi_i = \int_{TBCs} \frac{1}{2} S_{ijkl}\sigma_{ij}\sigma_{kl}\, dV \tag{3.17}$$

Expressing the complementary energy in terms of stresses in the expanded form:

$$\Pi_i = \int_{x_1}^{x_2}\int_{y_1}^{y_2} (S^i_{11}(\sigma^i_{xx})^2 + S^i_{22}(\sigma^i_{yy})^2 + 2S^i_{12}\sigma^i_{xx}\sigma^i_{yy} + \sigma^i_{xx}\varepsilon^i_{tx} + \sigma^i_{yy}\varepsilon^i_{ty} + 2S^i_{66}(\sigma^i_{xy})^2)\, dx\, dy \tag{3.18}$$

where S_{ijkl} is defined as:

$$\begin{pmatrix} \frac{(1-\nu^i_{zx}\nu^i_{xz})}{E^i_x} & -\frac{(\nu^i_{xy}+\nu^i_{zy}\nu^i_{yz})}{E^i_x} & 0 & 0 & 0 & 0 \\ -\frac{(\nu^i_{yx}+\nu^i_{zx}\nu^i_{yz})}{E^i_y} & \frac{(1-\nu^i_{zy}\nu^i_{yz})}{E^i_y} & 0 & 0 & 0 & 0 \\ 0 & 0 & 0 & 0 & 0 & 0 \\ 0 & 0 & 0 & 0 & 0 & 0 \\ 0 & 0 & 0 & 0 & 0 & 2(\frac{1+\nu^i_{xy}}{E^i_x}) \end{pmatrix}$$

Writing the above matrix of plain strain orthotropic material problem particularly for the

case of plain strain problem and isotropic material where properties are not dependent of the direction, the case in which we are approximating the behavior of our system, will be as follow:

$$\begin{pmatrix} \frac{1-\nu_i^2}{E_i} & -\frac{\nu_i+\nu_i^2}{E_i} & 0 & 0 & 0 & 0 \\ -\frac{\nu_i+\nu_i^2}{E_i} & \frac{1-\nu_i^2}{E_i} & 0 & 0 & 0 & 0 \\ 0 & 0 & 0 & 0 & 0 & 0 \\ 0 & 0 & 0 & 0 & 0 & 0 \\ 0 & 0 & 0 & 0 & 0 & 2(\frac{1+\nu_i}{E_i}) \end{pmatrix}$$

ε_{tx}^i and ε_{ty}^i for a plain strain problem of thermo-elastic material is given by:

$$\varepsilon_{tx}^i = (\nu_{zx}^i \alpha_z^i + \alpha_x^i)\Delta T \tag{3.19}$$

$$\varepsilon_{ty}^i = (\nu_{zy}^i \alpha_z^i + \alpha_y^i)\Delta T \tag{3.20}$$

For the case of an isotropic material ε_{tx}^i and ε_{ty}^i hence result in

$$\varepsilon_{tx}^i = \varepsilon_{ty}^i = \alpha_i(\nu_i + 1)\Delta T$$

In our study no mechanical load is directly applied into the system, and the stresses will be the result of the thermal loads of the systems due to the temperature change during cooling.

The expressions of Π_1 Π_2, and Π_3 are, respectively:

$$\Pi_1 = \int_0^L \int_{h_b}^{h_t} (A_1\sigma_{TBC}^2 + A_2(\sigma_{TBC}'')^2 + A_3\sigma_{TBC}\sigma_{TBC}'' + A_4\sigma_{TBC} + A_5\sigma_{TBC}'' + A_6(\sigma_{TBC}')^2)\, dx\, dy \tag{3.21}$$

$$\Pi_2 = \int_0^L \int_{h_s}^{h_b} (B_1\sigma_{BC}^2 + B_2(\sigma_{TBC}'')^2 + B_3(\sigma_{BC}'')^2 + B_4\sigma_{TBC}''\sigma_{BC}'' + B_5\sigma_{TBC}''\sigma_{BC} + B_6\sigma_{BC}''\sigma_{BC} + B_7\sigma_{BC} + B_8\sigma_{TBC}'' + B_9\sigma_{BC}'' + B_{10}(\sigma_{TBC}')^2 + B_{11}(\sigma_{BC}')^2 + B_{12}\sigma_{TBC}'\sigma_{BC}')\, dx\, dy \tag{3.22}$$

$$\begin{aligned}\Pi_3 = \int_0^L \int_0^{h_s} (&C_1\sigma_{TBC}^2 + C_2\sigma_{BC}^2 + C_3\sigma_{TBC}\sigma_{BC} + C_4(\sigma_{TBC})^2 + C_5(\sigma_{BC})^2 + C_6\sigma''_{TBC}\sigma''_{BC} \\ &+ C_7\sigma_{TBC}\sigma''_{TBC} + C_8\sigma_{BC}\sigma BC'' + C_9\sigma_{TBC}\sigma''_{BC} + C_{10}\sigma_{BC}\sigma TBC'' + C_{11}\sigma_{TBC} + C_{12}\sigma_{BC} \\ &+ C_{13}\sigma''_{TBC} + C_{14}\sigma''_{BC} + C_{15}(\sigma'_{TBC})^2 + C_{16}(\sigma'_{BC})^2 + C_{17}\sigma'_{TBC}\sigma'_{BC})\,dx\end{aligned} \tag{3.23}$$

Expressions $A_i(i = 1,...,6)$, $B_i(i = 1,...,12)$ and $C_i(i = 1,...,17)$ are shown in Appendix A.

Introducing Eqn. 3.21, 3.22 and 3.23 in Eqn. 3.16 the total complimentary energy for the system will be:

$$\begin{aligned}\Pi = \int_0^L (&\beta_1\sigma_T BC + \beta_2\sigma_B C + \beta_3(\sigma_T BC'')^2 + \beta_4(\sigma_B C'')^2 + \beta_5\sigma_{TBC}\sigma_{BC} + \beta_6\sigma''_{TBC} \\ &+ \beta_7\sigma''_{BC} + \beta_8(\sigma''_{TBC})^2 + \beta_9(\sigma''_{BC})^2 + \beta_{10}\sigma''_{TBC}\sigma''_{BC} + \beta_{11}(\sigma'_{TBC})^2 + \beta_{12}(\sigma'_{BC})^2 \\ &+ \beta_{13}\sigma'_{TBC}\sigma'_{BC} + \beta_{14}\sigma_{TBC}\sigma''_{TBC} + \beta_{15}\sigma_{BC}\sigma''_{BC} + \beta_{16}\sigma_{TBC}\sigma''_{BC} + \beta_{17}\sigma_{BC}\sigma''_{TBC})\,dx\end{aligned} \tag{3.24}$$

Where the expressions for $\beta_i(i = 1,...,17)$ con be followed in Appendix A

Resulting in functional energy function F in terms of σ_{TBC}, and σ_{BC}, and their derivatives $\dot{\sigma_{TBC}}$, σ''_{TBC}, $dot\sigma_{BC}$, and σ''_{BC}, that evaluated for values of x, form $(0tol)$ will lead to the complementary energy π. Which can be seen in the following Eqn. 3.25.

$$\Pi = \int_0^L F(\sigma, \sigma_a, \sigma', \sigma'_a, \sigma'', \sigma''_a)\,dx \tag{3.25}$$

Applying now variation principle to the energy function F:

$$\frac{\partial F}{\partial \sigma_{TBC}} - \frac{d}{dx}\left(\frac{\partial F}{\partial \sigma'_{TBC}}\right) + \frac{d^2}{dx^2}\left(\frac{\partial F}{\partial \sigma''_{TBC}}\right) = 0 \tag{3.26}$$

$$\frac{\partial F}{\partial \sigma_{BC}} - \frac{d}{dx}\left(\frac{\partial F}{\partial \sigma'_{BC}}\right) + \frac{d^2}{dx^2}\left(\frac{\partial F}{\partial \sigma''_{BC}}\right) = 0 \tag{3.27}$$

For details see Appendix A.

Evaluating F in Eqn. 3.26 and 3.27, yields to the following two linear differential equations:

$$\alpha_7 + \alpha_6\sigma_{TBC} + \alpha_5\sigma_{BC} + \alpha_4\sigma''_{TBC} + \alpha_3\sigma''_{BC} + \alpha_2\sigma''''_{TBC} + \alpha_1\sigma''''_{BC} = 0 \tag{3.28}$$

$$\eta_7 + \eta_6\sigma_{TBC} + \eta_5\sigma_{BC} + \eta_4\sigma''_{TBC} + \eta_3\sigma''_{BC} + \eta_2\sigma''''_{TBC} + \eta_1\sigma''''_{BC} = 0 \tag{3.29}$$

where α_i and η_i are constants dependent on the material and geometrical properties of the different layers of the coating system. Details of α_i and η_i are given in Appendix A.

Representing the ordinary differential equations in matrix form:

$$\begin{pmatrix} \alpha_1 & \alpha_2 & 0 & 0 & \alpha_3 & \alpha_4 & 0 & 0 & \alpha_5 & \alpha_6 & \alpha_7 \\ \eta_1 & \eta_2 & 0 & 0 & \eta_3 & \eta_4 & 0 & 0 & \eta_5 & \eta_6 & \eta_7 \end{pmatrix} \begin{pmatrix} \sigma''''_{BC} & \sigma''''_{BC} \\ \sigma''''_{TBC} & \sigma''''_{TBC} \\ \sigma'''_{BC} & \sigma'''_{BC} \\ \sigma'''_{TBC} & \sigma'''_{TBC} \\ \sigma''_{BC} & \sigma''_{BC} \\ \sigma''_{TBC} & \sigma''_{TBC} \\ \sigma'_{BC} & \sigma'_{BC} \\ \sigma'_{TBC} & \sigma'_{TBC} \\ \sigma_{BC} & \sigma_{BC} \\ \sigma_{TBC} & \sigma_{TBC} \\ 1 & 1 \end{pmatrix} = \begin{pmatrix} 0 & 0 \\ 0 & 0 \end{pmatrix}$$

The problem of two ODE system can be solved using boundary conditions in $x = 0$ and $x = L$:

- $\sigma^{(i)}_{xx}(0,y) = \frac{d\sigma^{(i)}_{yy}}{dx}]_{x=0} = 0$
- $\sigma^{(i)}_{xx}(L,y) = \frac{d\sigma^{(i)}_{yy}}{dx}]_{x=l} = 0$

The model will be applied to study the cooling case from constant temperature along the system, from high temperature of 1500^oC to constant temperature field at room temperature 40^oC. The different layers are assumed as isothermal and isotropic materials. Young's modulus, Poisson's ratio and CTE of the three layers used for the calculation of stresses are: For the YSZ top coat (1) $E_{TBC} = 30$ GPa, $\nu_{TBC} = 0,1$, $\alpha = 11x10^{-6}/^oC$, metallic bond coat $E_{TBC} = 100$

GPa, $\nu_{TBC} = 0,3$, $\alpha = 16.5x10^{-6}/^{o}C$ and nickel base superalloy $E_{TBC} = 150$ GPa, $\nu_{TBC} = 0,35$, $\alpha = 17x10^{-6}/^{o}C$. Thickness of the layers can be observed in Fig. 3.1.4.

Dimension	*[mm]*
h_SUB	2
h_BC	0.05
h_TGO	0.25
L	100

Table 3.1: Dimensions of the Thermal Barrier Coating system used in Analytical Modeling Fig. 3.1.

Layer	Young's modulus*[GPa]*	Poisson's ratio	CTE $x10^6$ $[/^oC]$
TBC	30	0.1	11
BC	100	0.3	16.5
SUBS	150	0.35	17

Table 3.2: Dimensions of the Thermal Barrier Coating system used in Analytical Modeling Fig. 3.1.

3.1.5 Results

A general analysis of two-dimensional steady-state thermal stresses in a thermal barrier coating system was developed. It has been observed in previous work [63] that failure of TBC systems occurs in the bond coat and surroundings due to high stress concentration in this area. Therefore, stresses will be observed in the mid-plane of the bond coat where higher stresses are concentrated. To understand the entire picture of the system in Fig.3.2, and 3.3, the stresses in the TBC-BC and Substrate-BC interfaces are also plotted. The bending effect of the whole coating system increases with the increase of the ceramic layer and with the porosity reduction. The effects are reduced and hence can be neglected when the elastic modulus and thickness of the top coat are low compared to the values of the substrate. [63] After deposition stress gradient exist in the thickness of the coating. The stresses tend to gradually change to in-plane compressive in the interface direction with temperature increase, and the tensile stresses in the insulating YSZ change from tensile to compressive. During cooling, in-plane compressive stress will arise in the coating due to the difference of coefficients of thermal expansion of substrate and thermal coating [59]. From results it can be observed that the compressive stresses in the top coat and bond coat are being higher than those of the bond coat after cooling to room temperature from 1500^oC. Measurements for thermal residual stresses obtained in the study are in accordance

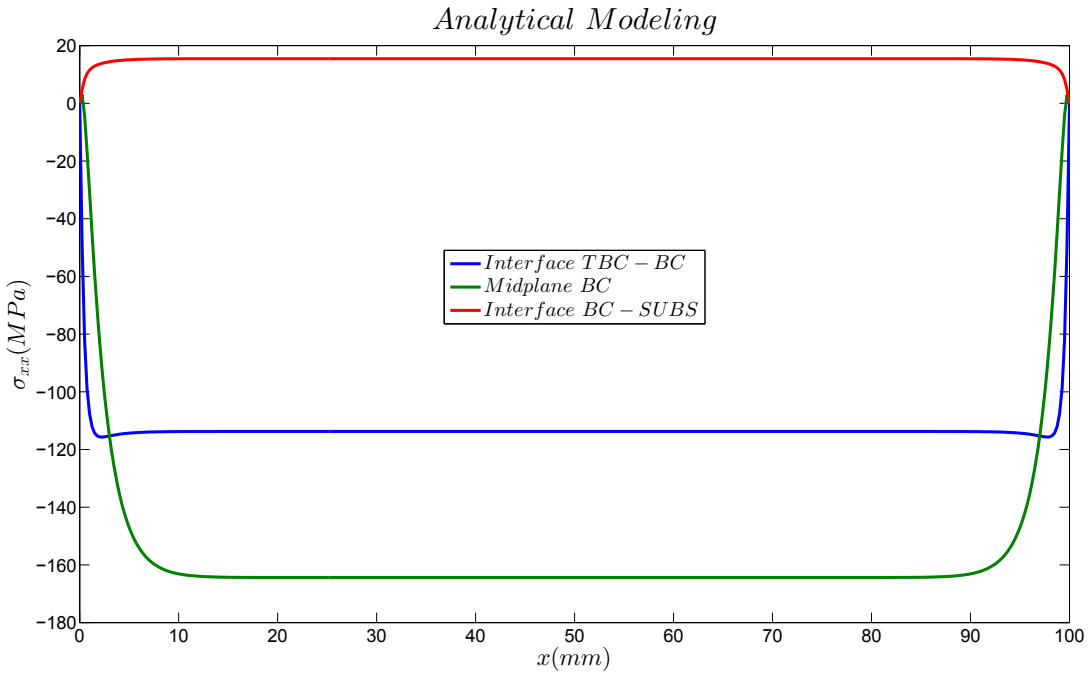

Figure 3.2: Stress distribution along the x direction of the TBC system.

with the statements in [63] and [59], however the high complexity of the problem is difficult to be completely cover in the analytical model. The aim of this analytical model is to understand the behavior of the coating system and not to represent every detail of its behavior. High limitations were observed in the model, like the dependence of temperature with time, oxidation and creep of the bond coat, sintering effect and rumpling of the thermally grown oxide. A computational model using FEA software to study the relevance of the different factors taking place within the coating system during service and cooling will be developed in the following section of this chapter.

It may be noted that the big difference is observed in stresses from the Nickel-based layer to the YSZ coat. Interface substrate-BC is subjected to tensile traction stresses, while contraction tensile stresses are taking place at the TBC-BC substrate. This mismatch is the reason for appearing of rumpling in the BC. This study is very limited since no effect of bond coat surface roughness can be studied, that has been proved to increase in stress within the coating [21]. Shear and out of plane stresses are likely to be almost zero along the piece but out of plane stresses can be observed in the sides of the component, as explained in [63], and it can lead to bending if stresses are sufficiently high and will help in rumpling development.

Computational model will be studied due to the restrictions of the analytical model, where

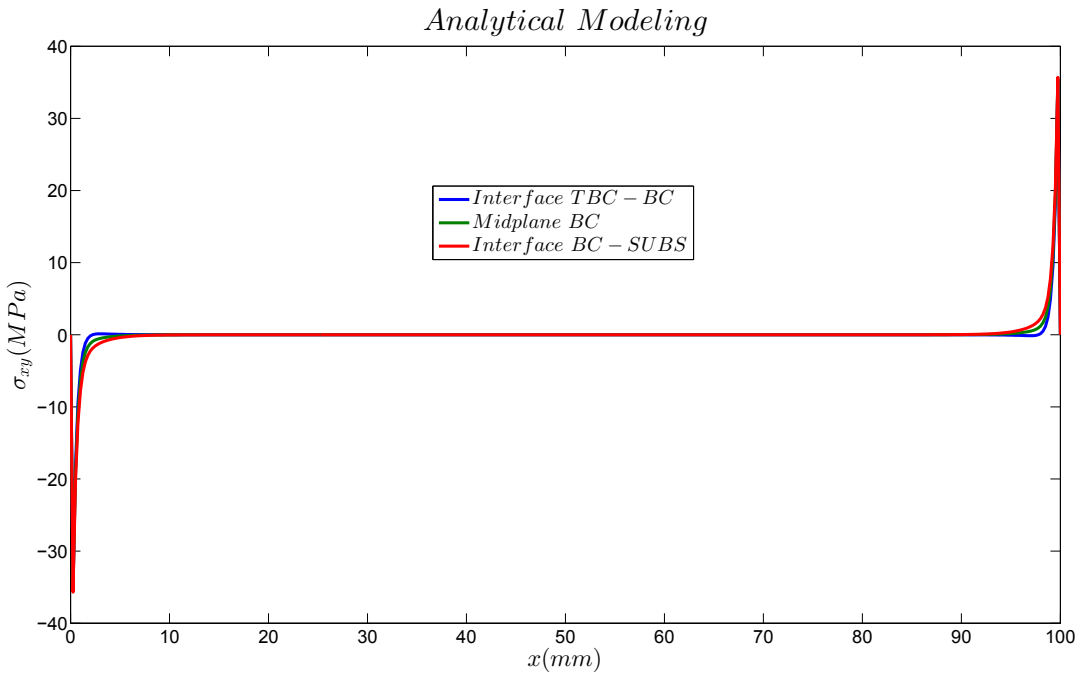

Figure 3.3: Distribution of in- plane shear stress along the bond coat and its interfaces.

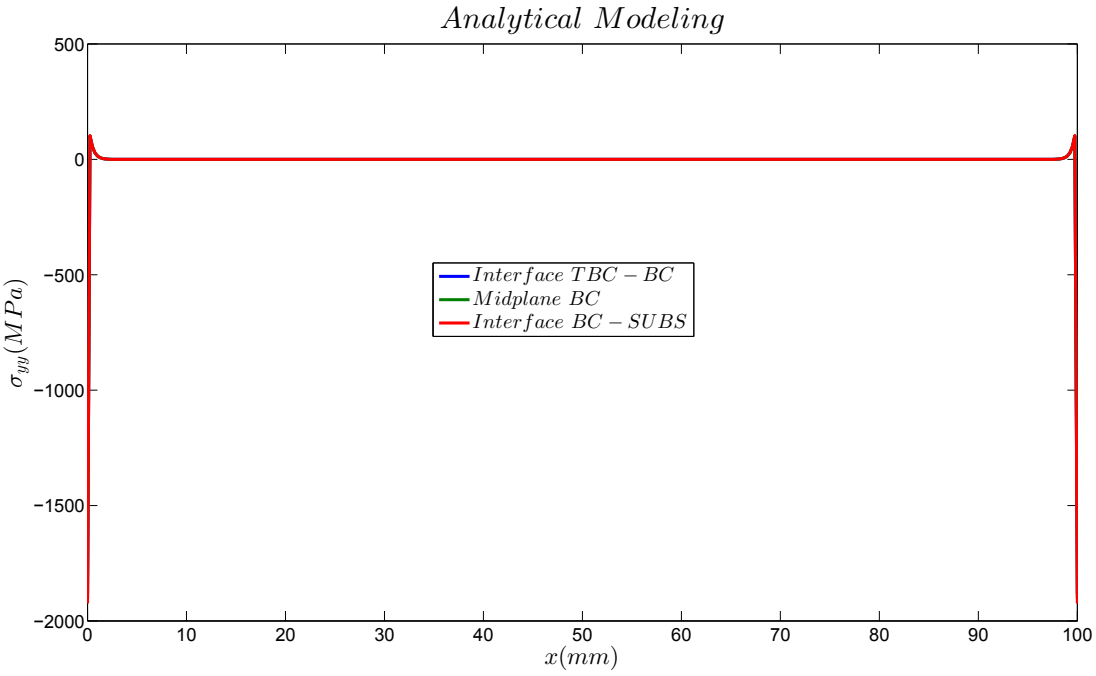

Figure 3.4: Distribution of out of plane stress along the bond coat and its interfaces.

relevant factors influencing the stress development in the coating like creep strength, volume expansion, sintering evolution, etc, are left in a side and are highly difficult to be included in the analytical study.

3.2 Computational Model

A finite element study has been undertaken to investigate the development of stresses in a thermal barrier coating system with an EB-PVD yttria stabilized zirconia top coat, Pt-Al metallic bond coat deposited over a nickel based superalloy, where relevance of the effect of sintering evolution, temperature fields, creep strength in the YSZ, as well as variation in creep strength in the bond coat and formation of the thermally grown oxide are studied. First the effect of sintering and temperature graded fields along the thickness of the coating will be discussed, along with the possible boundary conditions that better describe the behavior of the coating system. Three simulations will be undertaken for each model using two thermal steady states. One of them is used to obtain the temperature distribution during service and the second one to predict the temperature field in the final stage upon cooling. Once the temperature graded fields are obtained during service, then the main step cooling will be simulated, which is an steady state analysis where strain and stress during cooling to ambient temperature will be calculated in the system. To carry out this study a commercial finite element tool (Abaqus) will be used.

3.2.1 Boundary Conditions

Two sets of boundary conditions will be studied for the finite element analysis, taking into account rigidities at which the component is subjected during service, to study which of them better predicts the behavior of the thermal residual stress evolution in the EB-PVD thermal barrier coating system.

First boundary condition evaluated in the study, which will be called from now on BCs 1 or Old-BC in the graphs, restricts displacements on the longitudinal direction x, for $x = 0$ the left side of the system and restricts displacements on the lower bottom corner, $x = 0$, $y = 0$ in the horizontal and vertical direction x and y. See Fig. 3.5.

The second set of boundary conditions will restrict the displacement in the horizontal direction x for $y = 0$ and in vertical direction y for the set of points located in $x = 0$, it can be observed

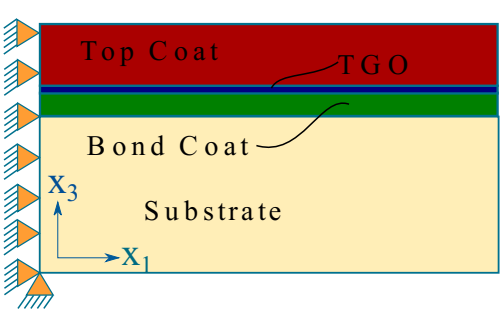

Figure 3.5: First set of BounCond (BCs1).

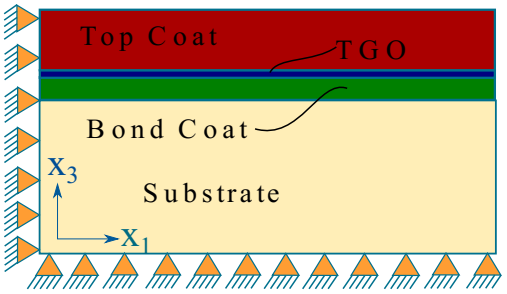

Figure 3.6: Second set of BounCond (BCs2).

in Fig. 3.6, which will be called from now on BCs 2 or New-BC in the graphs.

3.2.2 Temperature Fields

Gas turbine components are subjected to a very high temperatures on the outer surface of the top coat while internal cooling techniques are used in the inner surface of the nickel based super-alloy substrate to achieve longer life of the components and to allow higher inlet temperatures of the hot gas. This will produce a graded temperature field between the high temperatures of the top coat surface and the low temperatures of the substrate surface. Steady state heat transfer finite element analysis will be carried out in order to obtain temperature fields in the component upon cooling and during service. Two cases will be evaluated: (i) uniform cooling from 1500^oC to 40^oC, and (ii) non-uniform cooling. Non-uniform cooling takes place from: (i) graded temperature field during service, from 1500^oC in the outer surface of the YSZ top coat in contact with the inlet hot gas but protected by film cooling, to 650^oC in the inner surface of the substrate in contact with the cooling gas, to (ii) graded field of temperatures upon cooling late stage from 100^oC in the YSC surface to 40^oC in the Nickel-based superalloy inner surface [26],[63]. In order to understand the underestimation of considering uniform cooling when graded non-uniform cooling occurs.

3.2.3 TBC Constituents Behavior

To model the behavior of the TBC system, a complete understanding of the thermal and mechanical behavior of each constituent and its relation with the microstructure is needed. Aging has been proved to affect the properties and microstructure of the TBC system constituents. Sintering evolution in the YSZ top coat microstructure has been studied in Chapter 2 and its effect will be studied in the stress evolution within the coating system. Bond coat oxidation and

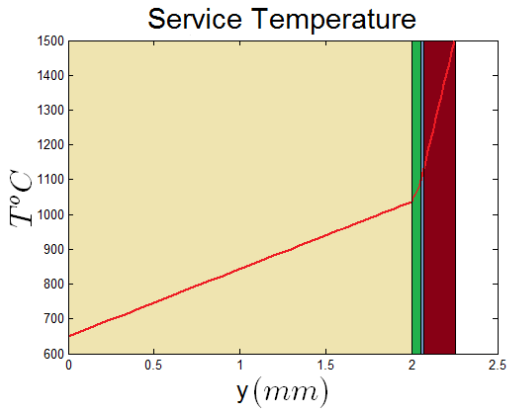

Figure 3.7: Predefined temperature field during service obtained by finite element heat transfer analysis.

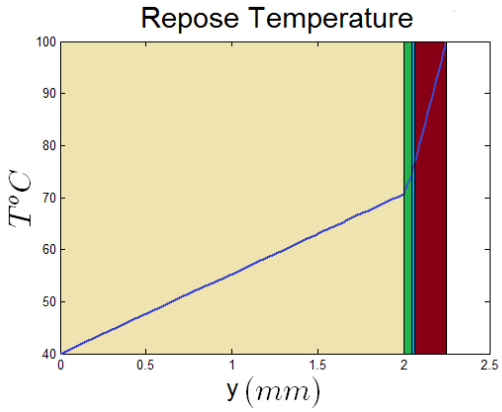

Figure 3.8: Predefined temperature field upon cooling to repose state obtained by finite element heat transfer analysis.

formation of TGO will be modeled and its effect will be studied.

EB-PVD YSZ Top Coat

As studied in Chapter 2, electro beam physical vapor deposited yttria stabilized zirconia top coat has a very characteristic microstructure. To model its mechanical behavior, evolution of sintering, columnar microstructure and spatial distribution has to be taken into account. From the typical columnar microstructure exhibited by EB-PVD methods 1.2.3, anisotropic elastic properties has been observed [19]. Anisotropic behavior of the top coat can be assumed as transversely isotropic, with different mechanical properties in the in-plane directions x and the out-plane direction along the columns length y. Transversely isotropic mechanical behavior and sintering effect will be modeled in a user material subroutine for its introduction in the computational study in the following subsection. Elastic properties of the ceramic top coat [26] were deduced from [[61], [44] and [53]], and can be observed in Table 3.2.4. Creep effect in the ceramic top coat is not presented here, since its effect in stress evolution can be neglected in areas close to the TGO interface where we have special interest [9], [22], [12].

Spatially Graded and Temperature Dependant Properties

Stress evolution along thermal barrier coatings systems will be computationally modeled to investigate the effects of properties and micro-structure evolution due to sintering [6] of the top YSZ coat. Abaqus user of material subroutine has been developed to introduce strain on the EB-PVD YSZ coating due to sintering and to study the image analysis of Young's modulus variation

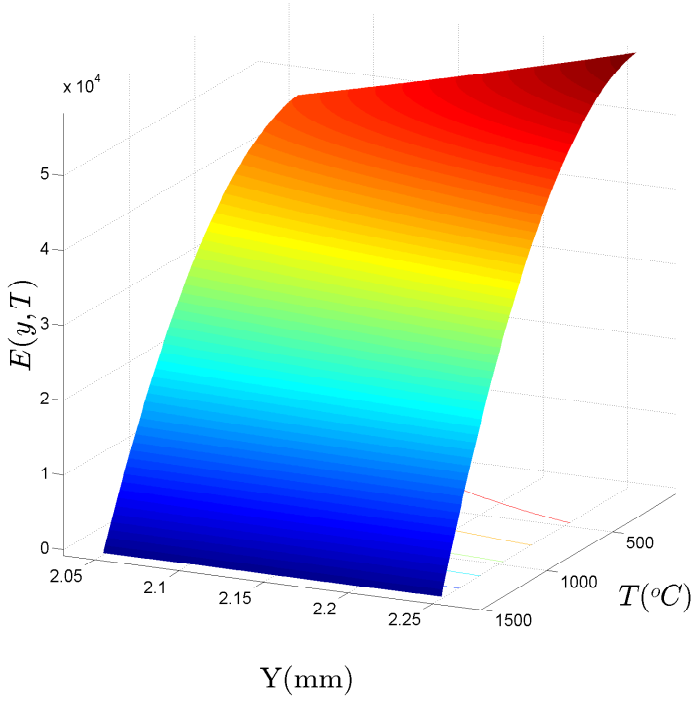

Figure 3.9: spatially graded and temperature dependent Young's Modulus.

with porosity along the top coat thickness in [24]. Sintering is known to produce hardening in the top coat by pore reduction leading to higher elastic modulus of the ceramic. Sintering occurs non uniformly in the ceramic top coat thickness, having higher sintering rate and strain increase in the lower areas closer to the bond coat. From image-analysis of Young's modulus variation with porosity due to sintering [24] and stress evolution due to sintering [39] studied in Chapter 2, coded in the subroutine along with temperature dependent properties [26], and then spatially graded thermally dependent properties are calculated. Dependence of Young's modulus along the y direction for the different range of temperatures can be observed in Fig. 3.9.

3.2.4 Thermally Grown Oxide, Bond Coat and Substrate Elastic Behavior

Elastic properties of the thermally grown oxide aluminide layer, metallic bond coat and Nickel based superalloy substrate [21] are assumed as isotropic and were obtained from [26], where Young's modulus and Poisson's ratio has been calculated from [14], [52], [25] and [41] shown in table 3.2.4. Plastic creep behavior of the BC and TGO is not presented here, its mechanical behavior will be included in the model later in this Chapter to study the rumpling effect of the thermally grown oxide layer.

	Young's Modulus [GPa]				*Poisson's Ratio*				*CTE* $[10^{-6}/^{o}C]$			
Temperature	SUBS	BC	TGO	TBC	SUBS	BC	TGO	TBC	SUBS	BC	TGO	TBC
20	220	200	400	48	0.31	0.3	0.23	0.1	14.8	13.6	8.0	9.0
200	210	190	390	47	0.32	0.3	0.23	0.1	15.2	14.2	8.2	9.2
400	190	175	380	44	0.33	0.31	0.24	0.1	15.6	14.6	8.4	9.6
600	170	160	370	40	0.33	0.31	0.24	0.11	16.2	15.2	8.7	10.1
800	155	145	355	34	0.34	0.32	0.25	0.11	16.9	16.1	9.0	10.8
1000	130	120	325	26	0.35	0.33	0.25	0.12	17.5	17.2	9.3	11.7
1100	120	110	320	22	0.35	0.33	0.25	0.12	18.0	17.6	9.6	12.2

Table 3.3: Elastic thermal dependent properties for different layers of the thermal barrier coating system.

3.2.5 Finite Element Analysis

Elasto-plastic finite element models are used to present two-dimensional computational models for the thermo-mechanical stress analysis of high-performance coatings where a system with three and four layers is studied.

The substrate formed of nickel superalloy component, 2 *mm* thickness, possess enhanced properties as high temperature resistant, ductility, oxidation resistance and hot corrosion resistance, Bond Coat is an oxidation-resistant metallic layer of 50 μm thickness where usually spallation failure occur, and oxidation of the bond coat typically occurs at high temperatures operating conditions resulting in TGO formation of 5 μm. These layers are regarded as linear elastic, isotropic and continuum, and TBC, 200 μm m thick, is a thermally insulating, strain tolerant oxide, stabilized zirconia as emerged as the preferred material regarded as a linear elastic, isotropic, with dependence of properties with temperature and y direction due to sintering.

The multilayer system is subjected to temperature change during cooling of the system from in service to repose state, implementing graded temperature fields in both on in service and repose states, during in service due to the exposure on the TBC side to the hot inlet gas and exposure of the side of the substrate to the cooling gas of the air cooling technology. While in the cooling state due to the uniformly cooling, both states by steady state heat transfer analysis is carried out using Abaqus software. For the accuracy of the analysis we implemented two systems of boundary conditions to observe which of them more closely approximate the behavior of the system. In the first set of boundary conditions, displacement was restricted in the horizontal direction in the left side of the system and in the left bottom point in both horizontal and

vertical direction. For the second set of boundary conditions, displacement was restricted in the horizontal direction in the left side of the system and in the bottom in the vertical direction.

3.3 Thermal Residual Stresses

Predicted residual stress state in a EB-PVD yttria coating over a metallic bond coat due to thermal loading may be liable for the failure of the TBC coating. Idealized flat surface is assumed for the study in order to observe the stress evolution in the coating due to coefficients of thermal expansion (CTE) mismatch. Effect due to cyclic thermal loading and bond coat roughness is not addressed in this study.

3.3.1 Three Layers System

First a finite element model for three layers will be designed, composed by a nickel based superalloy substrate, metallic Pt-Al bond coat and electron beam physically vapor deposited yttria stabilized zirconia top coat. Stress evolution during cooling to room temperature from service state will be analyzed. In particular, four cases will be studied: first boundary conditions 1 (Fig. 3.5) from the case of uniform cooling from 1500^oC to 40^oC and nonuniform cooling from Fig. 3.7 to Fig. 3.8 temperatures,and then boundary conditions 2 (Fig. 3.6) for both cases also, uniform and nonuniform cooling. Observed results of tensile stresses in direction x along the bond coat (see Fig. 3.10) are very disparate between the different cases. Based on our assumptions in previous works we can neglected the case of BCs 2 since the obtained stresses suppurate in an overwhelming manner yield stress of platinum aluminide bond coat that would cause direct failure of the coating will not occur. Further studies of the other three cases will be made because the difference of stresses could be due to boundary conditions or neglected roughness and creep effects. Note that wrinkling effect and a stress concentration with peak stress values occur at $x = 95mm$. The stress prediction that seems to behave closer to BCS, cooling behavior is nonuniform and cooling occurs under boundary conditions 2.

After addition of spatially graded and temperature dependent properties for the thermally insulating YSZ ceramic coat, tensile stresses due to elasto-plastic analysis tend to decrease at mean values along the bond coat and peak values at the end of the model where stresses are concentrated. This is due to the high stress concentration in the thermal barrier top coat.

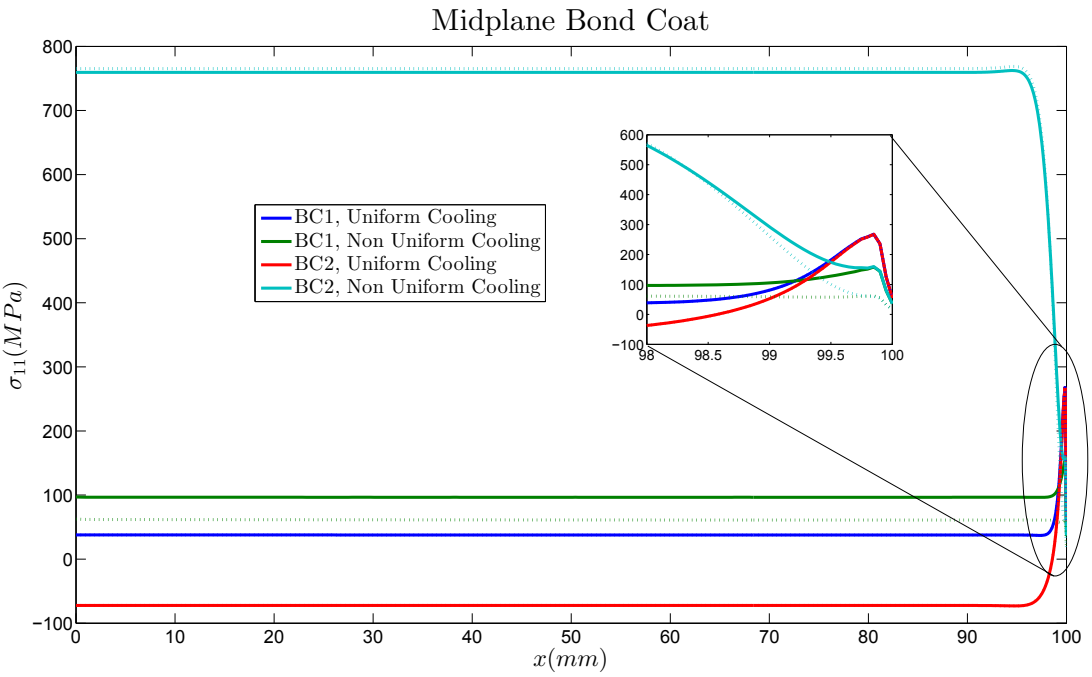

Figure 3.10: For a three layer system where TGO is not taken into account. Distributions of tensile stresses along the BC midplane (y=2.025) when temperature dependent properties have been study for BCs 1 and 2 as shown in Fig.3.5 and Fig.3.6 respectively, in the case of uniform and nonuniform cooling. Comparing the case of spatially graded properties(doted lines) and temperature dependent properties(solid lines).

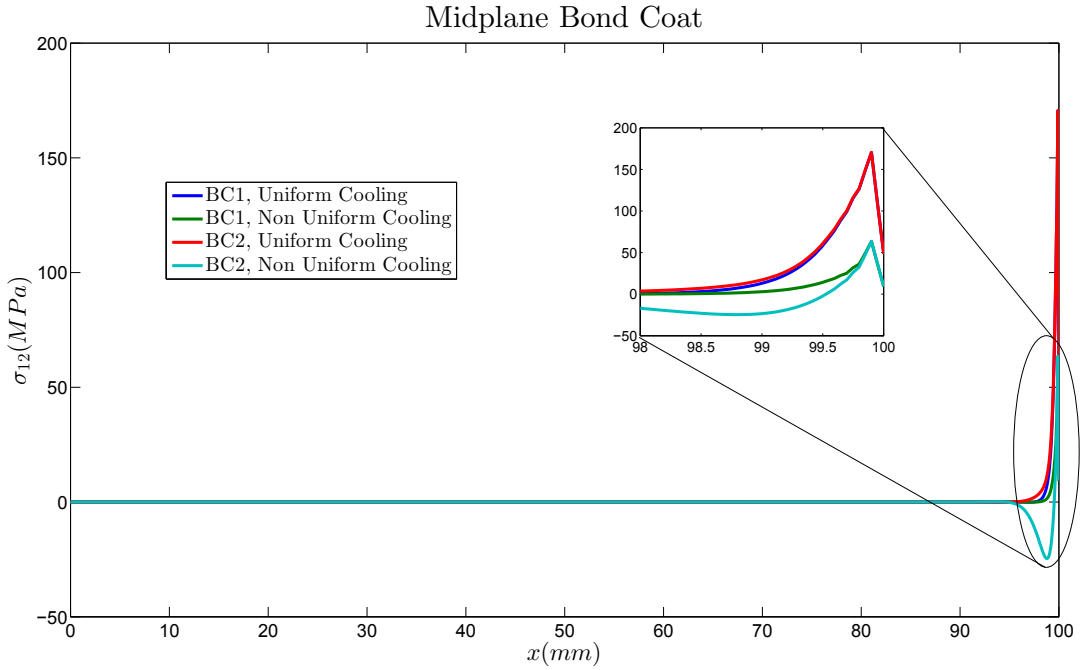

Figure 3.11: For a three layer system where TGO is not taken into account. Distributions of stresses in xy plane along the BC midplane ($y = 2.025$) when temperature dependent properties have been studied for BCs 1 and 2 as shown in Fig.3.5 and Fig.3.6 respectively, in the case of uniform and nonuniform cooling.

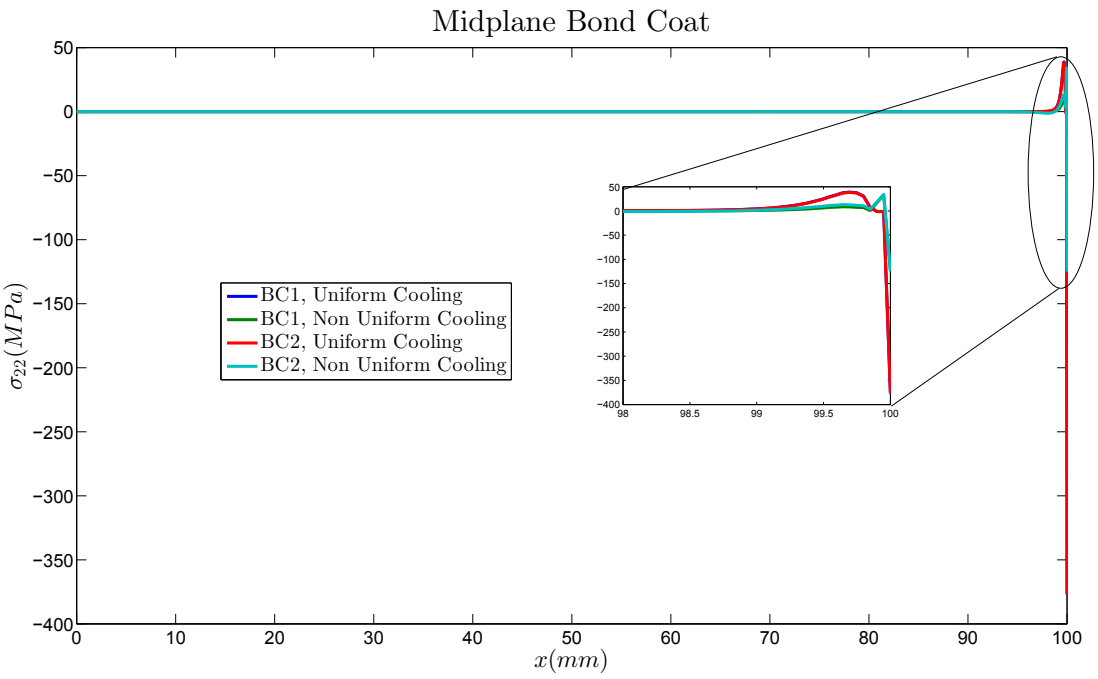

Figure 3.12: For a three layer system where TGO is not taken into account. Distributions of out of plane stresses along the BC midplane ($y = 2.025$) when temperature dependent properties have been studied for BCs 1 and 2as shown in Fig.3.5 and Fig.3.6 respectively, in the case of uniform and nonuniform cooling.

Distribution of shear and out of plane stresses are almost zero generally along the bond coat with small peaks at the end in the case of shear stress and maximum in the y-direction that fluctuate from 100 to -150 MPa. This fluctuation is likely to cause roughness in the bond coat. Values of shear and out of plane stresses are of the same order for both cases before taking into account sintering effect on the YSZ top coat of the system and after. Significant changes and more accurate stress values are noticed when sintering straining effect is accounted.

3.3.2 Four Layers System

Largest tensile stresses are likely to occur in thermally grown oxide interfaces according to several studies [21][26][3] due to its thin structure in relation with the bond coat and ceramic layer thickness, playing a crucial role in the TBC systems. The largest stress values were found to be in flat areas of the TGO layer, with in plane compressive stresses values of the order of 3.5 *GPa*. Therefore a flat constant thickness thermally grown oxide layer of 5 μm will be included in the study to understand the oxide growth between BC and TBC. It can be observed in our study that measurements are very similar for the case of nonuniform cooling when boundary conditions 1 are imposed.

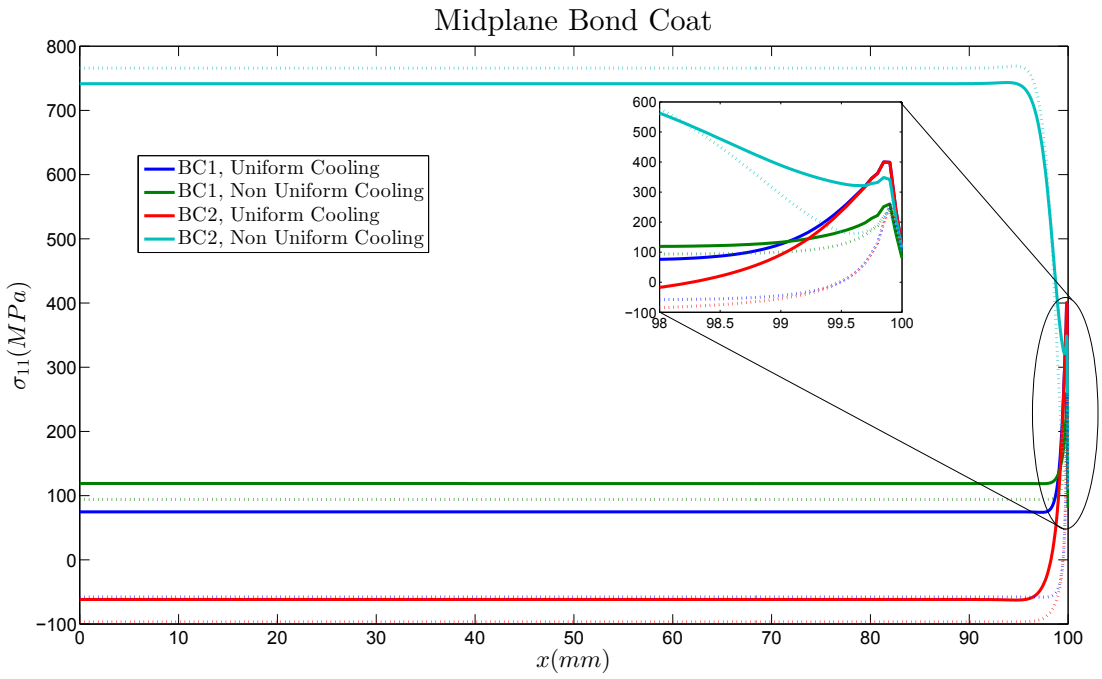

Figure 3.13: Four layer system to study the effect of thermally growing oxide. Distributions of shear stresses along the BC midplane ($y = 2.025$) when temperature dependent properties have been studied for BCs 1 and 2 as shown in Fig.3.5 and Fig.3.6 respectively, in the case of uniform and nonuniform cooling. Comparing the case of spatially graded properties(doted lines) and temperature dependent properties(solid lines).

In case of inclusion of the thermally grown oxide layer into the coating systems, an increase in the bond coat tensile stress has been observed as shown in Fig. 3.13 for both the mean stresses of the flat areas from 100 to 120 MPa and the peak areas where stresses are concentrated 300 to 400 MPa in the case of BCs 1 and nonuniform cooling.

In-plane tensile stresses in the midplane of bond coat tend to decrease due to he effect of spatially graded and temperature dependent properties for the thermal barrier coating layer because of the increase of stresses in the grown oxide. It can be seen from Fig. 4.3 that for the case of TGO thickness of $5\mu m$ stresses are very high compared to the stresses in the bond coat, with values of 2.8 GPa in the flat regions and tend to decrease at the end to values of 1.3 GPa. Opposite to the behavior of the stresses in the bond coat mid plane which shows peaks in the last area of the geometry studied. This will lead to formation of wrinkles in the BC and TGO and concentration of stresses in the peaks and valleys.

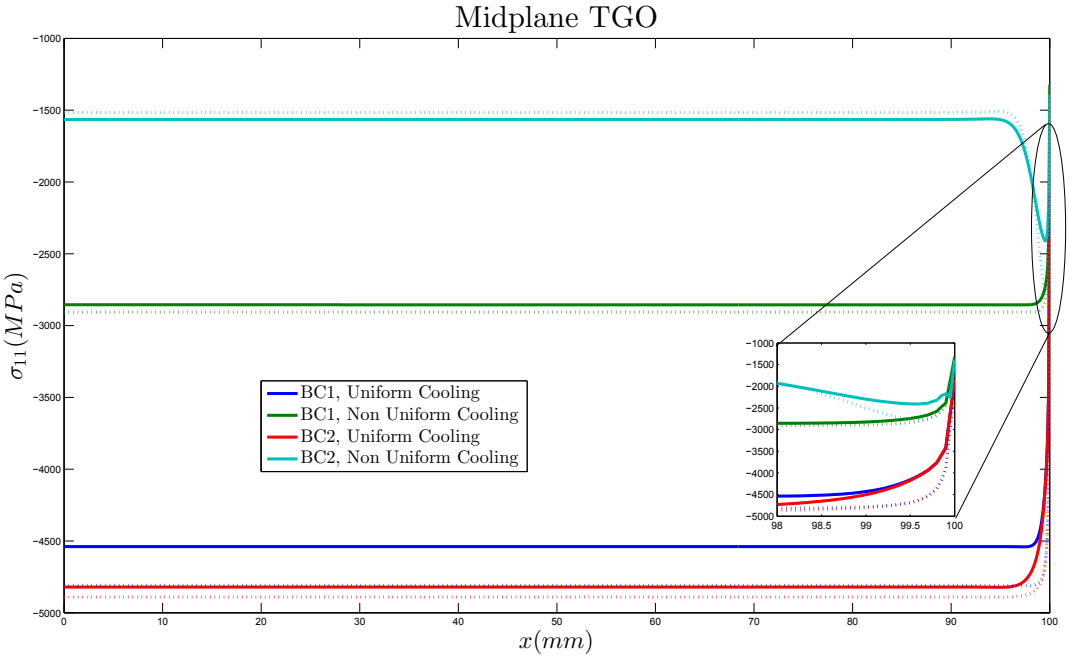

Figure 3.14: Four layer system to study the effect of thermally growing oxide. Distributions of tensile stresses along the BC midplane ($y = 2.025$) when temperature dependent properties and spatially graded in the TBC thickness due to sintering rate have been study for BCs 1 and 2 as shown in Fig.3.5 and Fig.3.6 respectively, in the case of uniform and nonuniform cooling.

Influence of BCs On Stresses

From the plots of stresses it can be observed that a disparate behavior in the application of the different boundary conditions. For the analysis of the cases where boundary conditions 1 as shown in Fig.3.5 are applied to the model and similar behaviors with small stress increment can be observed between uniform and nonuniform from service to repose state. This shows a curbed deformation as has been described in [63] due to stress mismatch between the different coatings.

In the other two cases where boundary 2 conditions are restricting the coating system the system is observed to shrink, shorter and smaller due to the bottom restriction. This causes a high stress increase in the system. First the observed result in the bond coat is seen to be negative due to the compression of the system, but when nonuniform temperature cooling occurred, the compressive stresses become tensile stresses. Therefore, it can be assumed that BCs 2 do not resemble the thermal barrier coating system behavior.

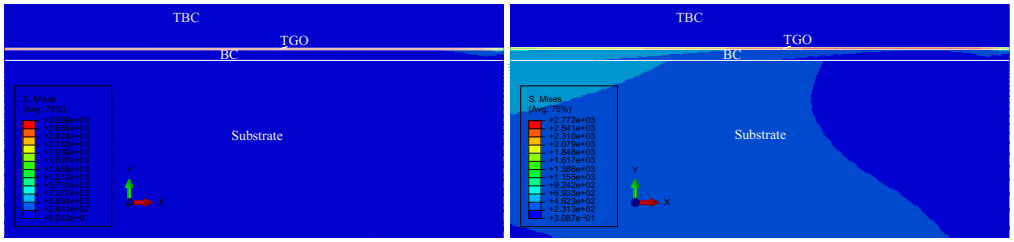

Figure 3.15: Von Mises stress field [MPa] is displayed over the finite element TBC-TGO-BC-Substrate coating system for a)Boundary conditions 1 b)Boundary conditions 2.

3.3.3 Conclusion

Variations in the stress field due to addition of thermally grown oxide accounting hardening of the thermal barrier coating due to sintering have been studied. It is observed that tensile and shear stresses in the out of plane direction remain constant. It is also observed that after addition of sintering effect and thermally grown oxide layer results are likely to behave very closely to previous experiments in the field of thermal residual stresses in thermal barrier coating systems.

Creep straightening is likely to occur as discuses in previous studies [39][22] in the metallic bond coat at typical operating temperatures, even though creep analysis is not included in the model. Nonlinear behavior of the material due to creep will be addressed using elastic perfectly plastic properties of the Pt-Al bond coat.

Nonuniform temperature cooling and sintering effect were likely to be a possessive addition since it is an accurate approximation of gas turbine components behavior during service and cooling, and it has been proved to be an step forward in life stress prediction of thermal barrier coating systems. For further finite element analysis, only the case of boundary conditions 1 and non uniform cooling will be considered.

The observed increase of tensile stresses in the farthest area from the application of the boundary conditions in the bond coat layer, and simultaneous decrease of the compressive stresses of the thermally grown oxide layer. Will lead, in addition to the fluctuations on the shear stresses, to the formation of wrinkles in the TGO that will highly affect in the stress field of the coating system.

CHAPTER 4

Thermal Stresses Evolution

4.1 Influence of Thermal Grown Oxide Thickness in Stresses

Bond coat oxidation of thermal barrier coating system during service is an important factor and it should be taken into account for the top coat spallation. This oxide growth increases due to the stored elastic strain energy per unit area which is responsible for the ceramic spallation. The thermally grown oxide layer is considered in the finite element analysis to evaluate the influence of the stress evolution with respect the previous three layers system. It has been stated by earlier researches that TGO growth has an important effect in oxidation induced stresses, but it can also be influenced by creep and roughness of bond coat[3].

The evolution of stresses will be analyzed in the following sections along the three different planes of the TBC system for the cooling process of different TGO thicknesses. First, the stresses along the bond coat midplane after then along the TGO midplane, and finally stresses will be studied in the transversal direction to the layers interfaces. The different paths followed for the analysis are shown in Fig. 4.1.

4.1.1 Bond Coat

Residual thermal stresses developed in the mid plane of the bond coat during cooling are analyzed for the thermo-mechanical model previously presented. Preselected optimum characteristics are consistent with boundary conditions 1, spatially graded and thermal dependent proper-

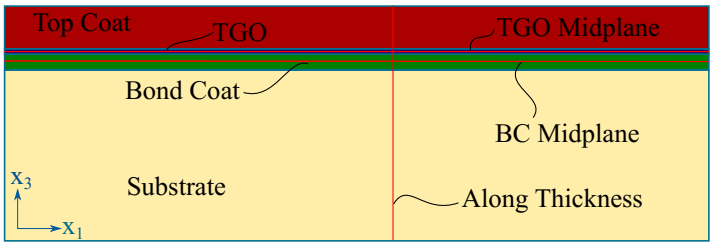

Figure 4.1: Red paths are followed to study the thermal stresses along the coatings.

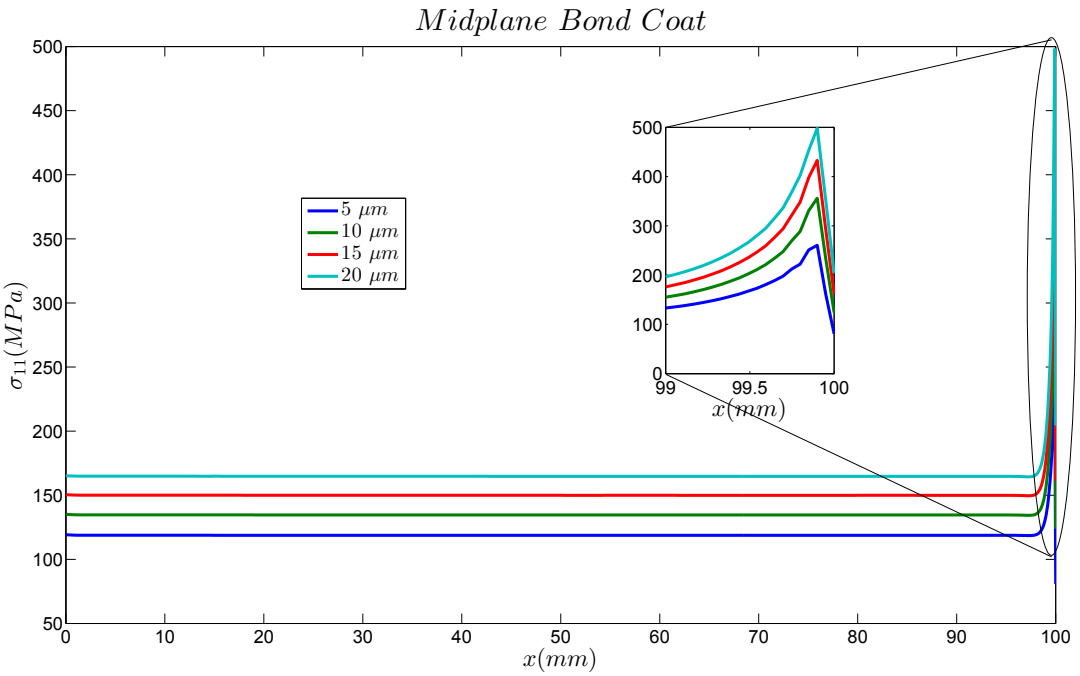

Figure 4.2: Distribution of in plane stress at the Bond Coat mid-plane for the case of different Thermal Grown Oxide thicknesses.

ties of the bond coat and temperature graded fields are considered for different TGO thicknesses, where the TGO growth is driven by oxidation of aluminide particles of the bond coat. It has been observed in [24] that peak stresses are developed during service at high temperature in the BC-TGO interface where TGO is more likely to form. In-plane residual stresses during cooling for thicknesses from 5 μm to 45 μm are presented in Fig 4.2. Peak tensile stresses increase from 260 *MPa* to the values of 566 *MPa* in accordance with TGO which increase from 5 μm to 45 μm, respectively, as presented in Fig. 4.2. Peak values of thermal stresses in the bond coat mid plane are presented in table for the in-plane and out of plane directions, that is direction x_1 and x_2, respectively are expressed in Table 4.1.1. Increase of in-plane stresses can be explained due to higher stresses due to mismatch increase by TGO growth. Out of plane stresses remain constant with small variations.

Bond Coat	*Thickness [μm]*			
Stress[MPa]	5	10	15	20
In-plane	260	338	392	434
Out-Plane	90	92	92	93

Table 4.1: Peak stresses along the Al-Pt bond coat for different thicknesses of the thermal grown oxide layer due to alumina oxidation.

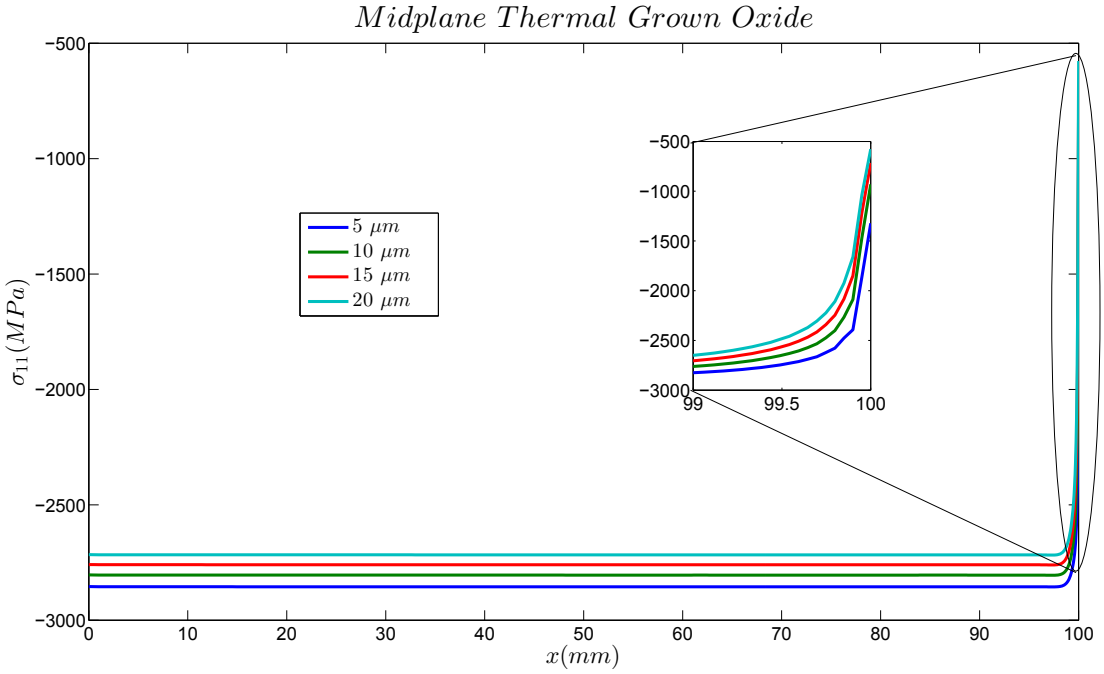

Figure 4.3: In-plane residual stress at the thermally grown oxide mid-plane for the case of different Thermal Grown Oxide thicknesses.

4.1.2 Thermal Grown Oxide

Residual compressive stresses of the TGO mid-plane are likely to decrease from values of 2855 MPa to 2480 MPa when thickness of TGO increases, as shown in Fig. 4.3. Decrease due to growth occurs due to the creep relaxation and reduction of stored strain energy. The average in-plane stress for a flat thermal oxide layer was found to be around 2.7 GPa in [24], highly in accordance with our model, while maximum and minimum in plane stresses ranges from -1.8 GPa to -4.5 GPa in the undulated TGO model, that demand the need of rumpling inclusion in our model. Increase in compressive out of plane stresses in the TGO, presented in Table 4.1.2, while tensile out of plane stresses were observed in the BC. It may be observed that larger mismatch in out of plane stress along BC-TGO occurs than along TGO-TBC interface, where TGO formation occurs.

Bond Coat	*Thickness [μm]*			
Stress[MPa]	5	10	15	20
In-plane	-2855	-2804	-2721	-2662
Out-Plane	-57	-106	-165	-196

Table 4.2: Peak in-plane and out of plane residual stresses along the Al-Pt bond coat for different thicknesses of the thermally grown oxide layer due to alumina oxidation.

4.1.3 Along Coating Thickness

In-plane stresses along the TBC system thickness in the middle of the sample $x = 50mm$ is illustrated in Fig. 4.4. A better understanding of residual thermal stresses along the interfaces is obtained. Tensile stress of magnitude of 100 MPa is observed in the BC near the BC-TGO interface. Maximum mismatch is observed with the compressive stress values around 2.8 GPa in the TGO near the BC interface for a TGO thickness of 0.005 μm and decreasing as the TGO thickness increases. In the TGO-TBC interface, measures of 2.8 GPa compressive stress are observed in the TGO side while magnitudes of 200 compressive stress is observed in the TGO side. Significant difference of stresses are shown in the BC-TGO interface that is in agreement with the thermal strain mismatch and therefore cracks are more likely to occur in this area as explained in [24]. Qualitative results are again in accordance with previous studies [10][13][31], but quantitative results are lower, need the importance of implementation of TGO creep.

4.2 Creep Behavior and TGO Growth

In Chapter 3, the stress evolution during cooling of the EB-PVD thermal barrier coating has been studied. Hardening due to creep is observed at high temperatures during service conditions of the gas turbine components and can affect its lifetime. In the previous section the effect of growth of TGO thickness in the stress evolution upon cooling was studied, concluding that the stress along the TGO decreases with the increase of TGO thickness. In this section, the effect of creep and TGO growth in the microstructure and stress field prior to cooling will be modeled using Abaqus.

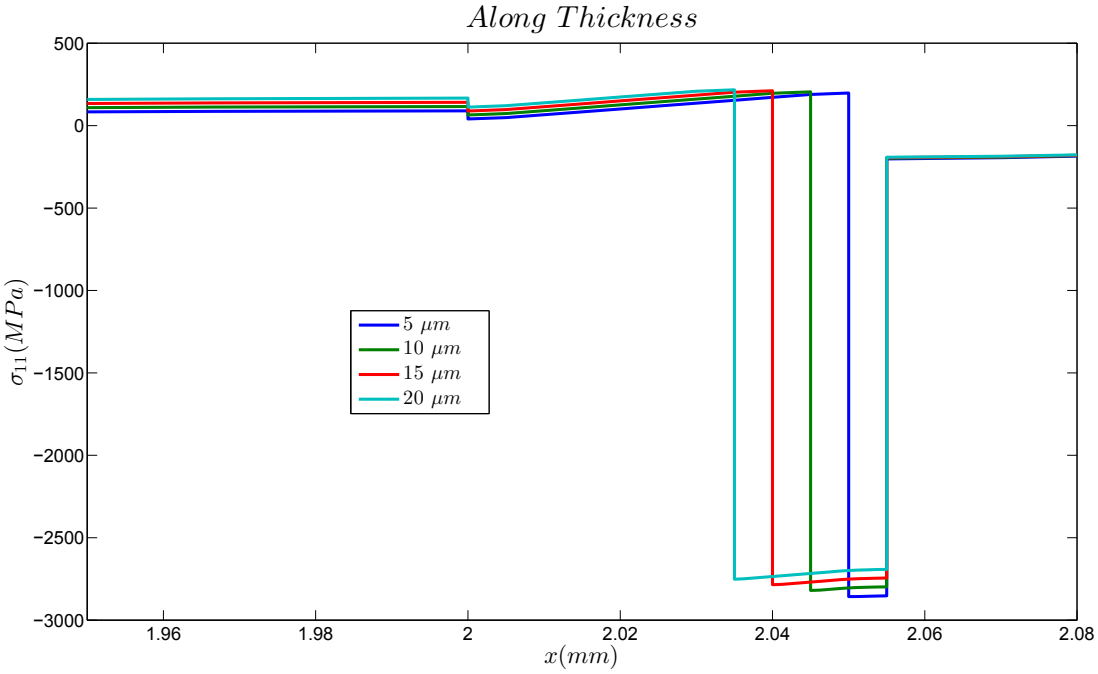

Figure 4.4: Distribution of in-plane stress along the TBC system for the case of different Thermal Grown Oxide thicknesses.

4.2.1 Creep Properties

Creep behavior will be assumed to be the stress and temperature dependent and steady-state described by the following power law equation:

$$\dot{e}^{vp} = Aexp\left(\frac{-Q}{RT}\right)\left(\frac{\sigma_{eq}}{\sigma_0}\right)^n \tag{4.1}$$

where A is the creep constant $[s^{-1}]$, Q is the activation energy, R is the molar constant of gases [8.314 $J/molK$], T is the temperature of the component, σ_{eq} is the corresponding von Mises equivalent stress $[MPa]$, σ_0 is a fixed parameter $[MPa]$ and n is the order of the stress equation.

TGO

Previous experimental studies concluded that TGO is mostly alumina oxide, containing other oxides also. Addition of reactive elements, as the one observed in Frachon by metallographic analysis which are rich in yttrium, affect the growth mechanism and oxide microstructure [56], [5] and [43]. Creep resistance improvement has been observed by dopant addition to the alumina oxide. The effect of this additions was studied in [50], [28] and [27], and has been compared in [24], as shown in Fig. 4.5. Average values of the measurements obtained in [28] and [27]

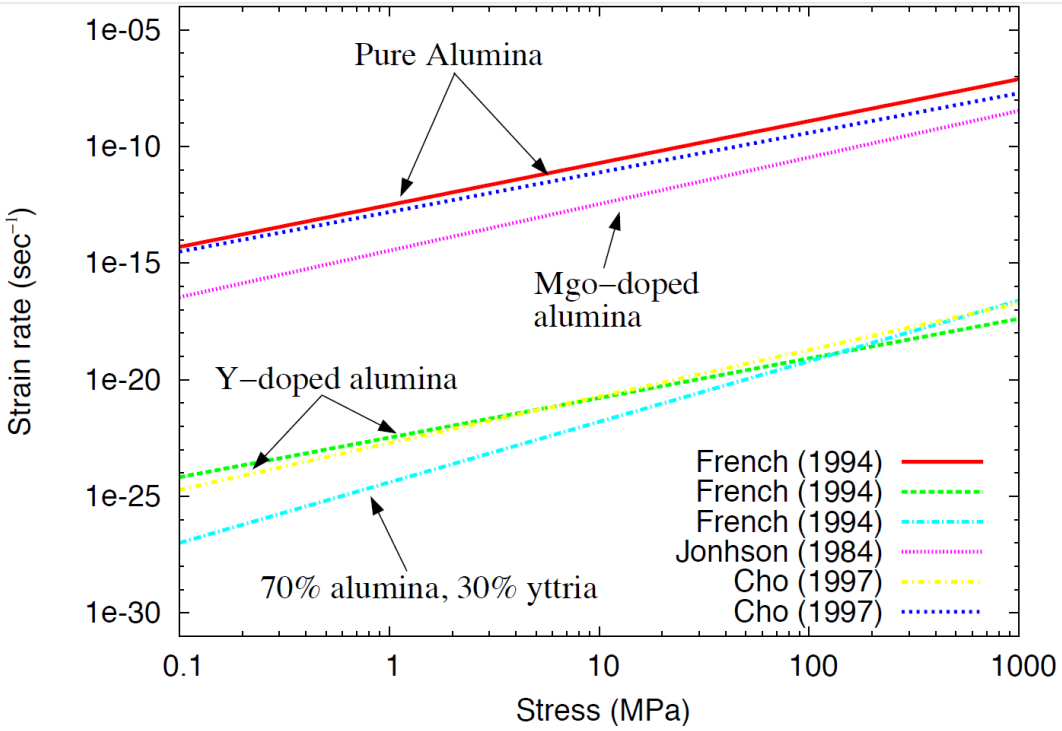

Figure 4.5: Creep properties of alumina oxide at 1100^oC to study the effect of addition of dopant and reactive components such as yttria [24].

for yttria coped alumina are calculated to define the creep behavior of the TGO in the model. Alumina si treated to be viscoelastic, where no plastic strain occur as per stated in [15] and to following the power law Eqn. 4.1, where the values for the TGO creep law are given as: stress equation order n=1.85 implying a controlled vacancy diffusion in alumina [16], activation energy Q= 690 kJ/mol, the power law multiplier A= 5.1 10^{16} and reference stress σ_0= 100 MPa.

Stress equation order	n=1.85
Activation energy	Q=690 kJ/mol
Power law multiplier	A=5.1 $\times 10^{16}$
Reference stress	σ_0= 100 MPa

BC

The weak creep behavior of the bond coat allows a great relaxation of stress, supporting the resistance of the top coat to spallation. The bond coat is a multiphase material with evolving microstructure when exposed to oxidation during time according to experimental observations in [24]. Mechanical and thermal properties of the platinum-aluminide isotropic bond coat are assumed to be time-independent and temperature-dependent, and are presented in Table 3.2.4.

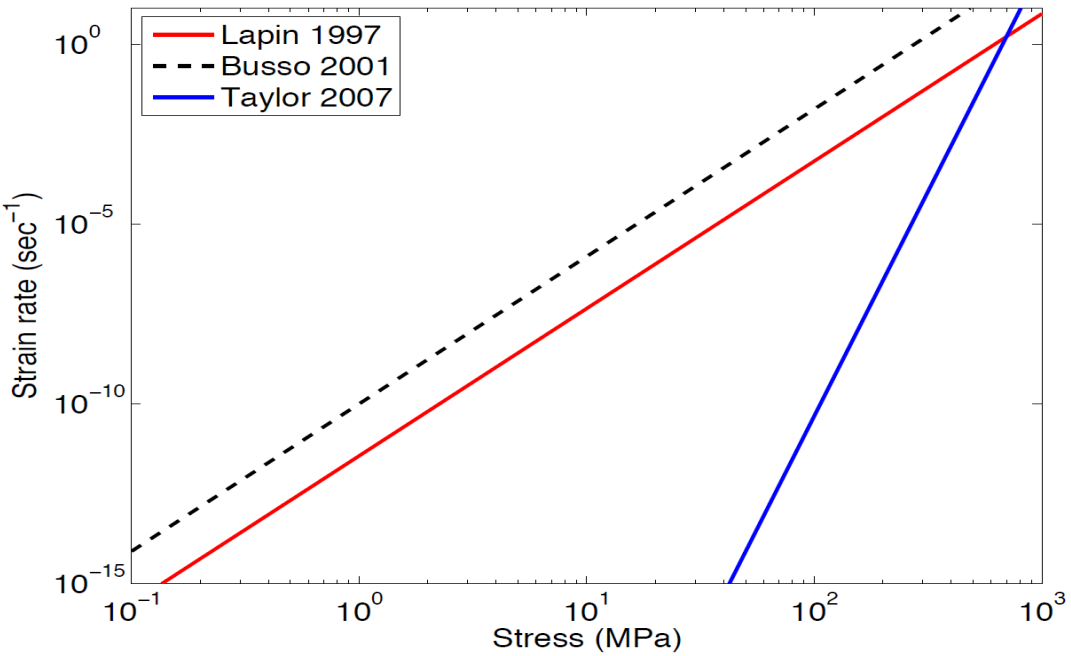

Figure 4.6: Creep properties of bond coat at $1100^{o}C$: experimentally studied by different authors [24].

An homogenization method to determine the creep properties of the bond coat, based on experimental results [45] and [25], was presented in [21]. Following the numerical approach expressed in [24] for the creep behavior of the bond coat described by Eqn. 4.1, and taking the average of the values obtained by experimental means by [38], [36] and [21] presented in Fig. 4.6, creep behavior of the bond coat will be defined. Average values for the power law equation are: stress equation order n= 4.1, activation energy Q= 282 kJ/mol, power law multiplier A= 1.1 10^{8} and reference stress σ_0= 100 MPa, and are listed in Table 4.2.1.

Stress equation order	n=4.1
Activation energy	Q=282 kJ/mol
Power law multiplier	A=1.1 $\times 10^{8}$
Reference stress	σ_0= 100 MPa

4.2.2 Oxide Growth

TGO plays a crucial role in the TBC spallation due to its thin nature in comparison with bond coat and top coat layers, and elastic stored strain energy in the system increases according to thickening of the thermal grown oxide. Alumina oxide formation occurs at the BC-TGO interface due to the higher diffusivity of oxygen than aluminide cations within the TGO. Columnar grain microstructure normal to the oxide interface is observed close to the BC-TGO interface

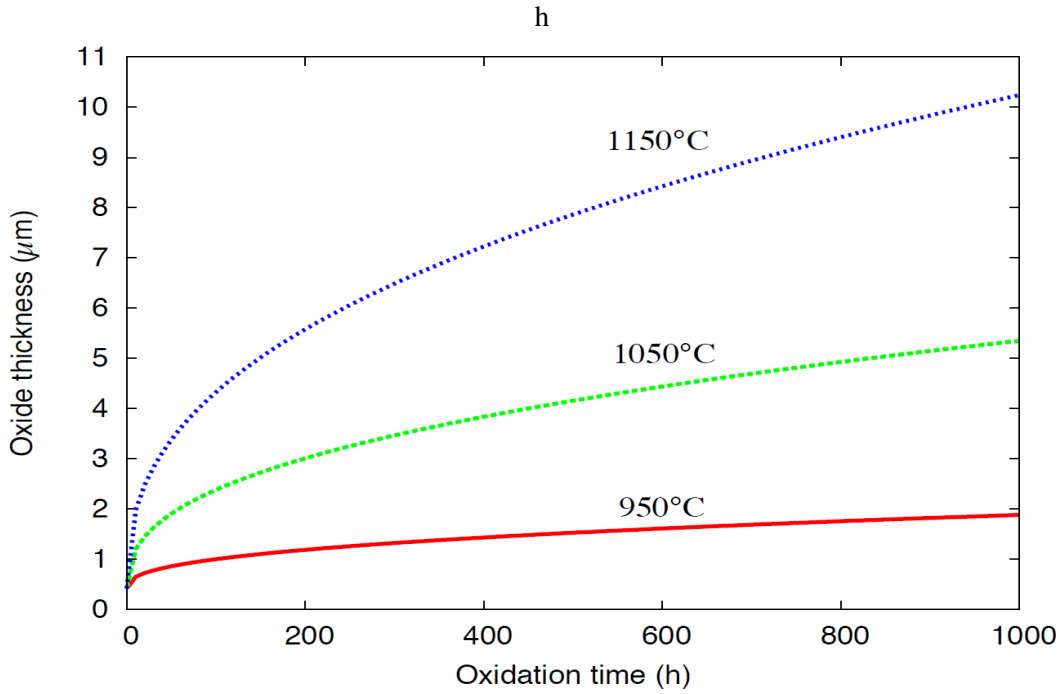

Figure 4.7: Evolution of thermal grown oxide thickness with time for temperatures: 950^0C, 1050^0C and 1150^0C [38].

[24], inducing anisotropic growth strains. Oxidation of the bond coat induces a volumetric expansion at the thermally grown oxide interface. A study carried out by the University of Birmingham supported by Siemens has determined the kinetics of the oxide growth at different temperatures up to 1000 h. Equation 4.2 describes the oxide thickness for different times, measured normal to the bond coat-top coat interface, where material parameter k_n and n are dependent on temperature, h_0 is the initial thickness of the specimen after deposition process and t is the time exposed to high temperature. Oxide growth is presented in Fig. 4.7 for different temperatures up to the 1000 h is studied.

$$h_{TGO} = h_0 + (k_n t)^{1/n} \tag{4.2}$$

4.2.3 Oxide Interface Roughness

Observations have pointed the importance of the TGO morphology and how small variations of it can lead to a different stress field close to the oxide interfaces, increasing the possibility of fracture and propagation. Frachon has characterized the TGO morphology using image processing analysis, which consists of processing an initial image of the TBCs obtained in the Scanning electron microscope (SEM) into a binary image, and subtracting the TGO geometry

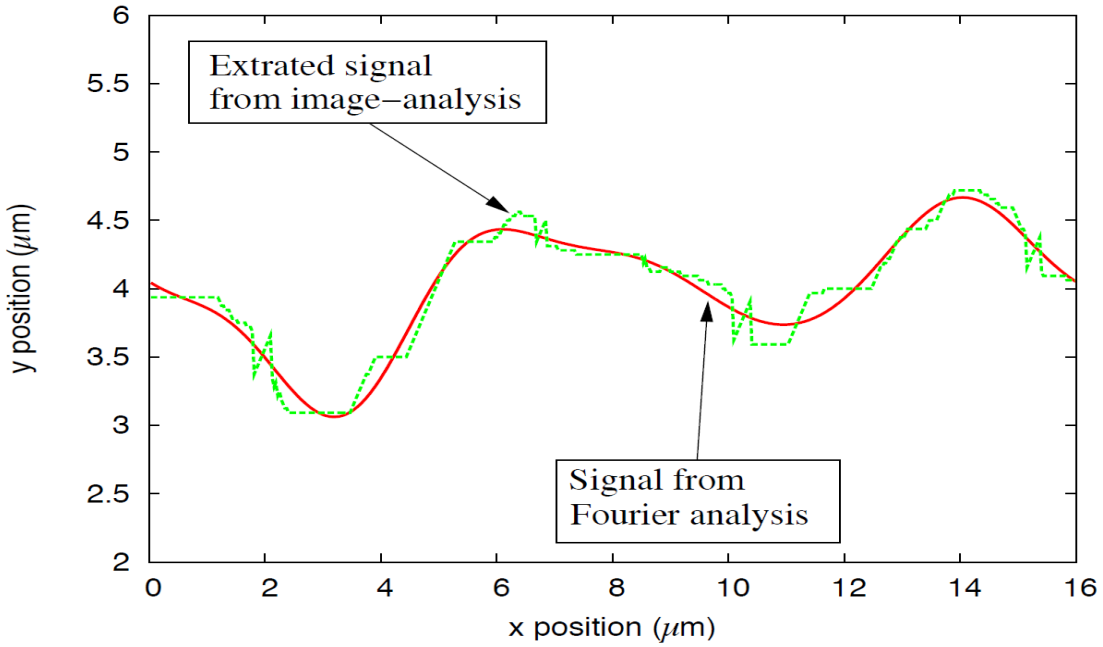

Figure 4.8: Approximation of the interface obtained by image analysis by a Fourrier analysis [24]

by a geometrical percolation procedure. The real shape of the upper surface of the TGO layer can be observed in Fig 4.8. An approximation of the real TGO roughness obtained into a sinusoidal interface will be made and included to the model to better understand the concentration of stresses in local areas due to the TGO interface roughness.

4.2.4 Finite Element Analysis

Investigation of the TGO morphology is extremely relevant, because of its importance in the local stress field and the though TGO interfaces. Finite element model defined in Chapter 3, will be modify to include creep behavior of the bond coat and TGO layers. Swelling properties and modeling growth of the TGO by bond coat oxidation and idealized sinusoidal interfaces of the TGO, are crucial factors in influencing the spallation of the TBCs. Therefore these factors are necessary to consider the more realistic behavior of the stress evolution within a thermal barrier coating system. The mesh of a small portion of the model can be observed in Fig. 4.9, in which sinusoidal interface is characterized by a average wave length $w = 12\ \mu m$ and amplitude $a = 1\ \mu m$. The simulation run conducted 40 min from high temperature following the temperature distribution as shown in Fig. 3.7, cooled down to low temperature distribution as presented in Fig. 3.8.

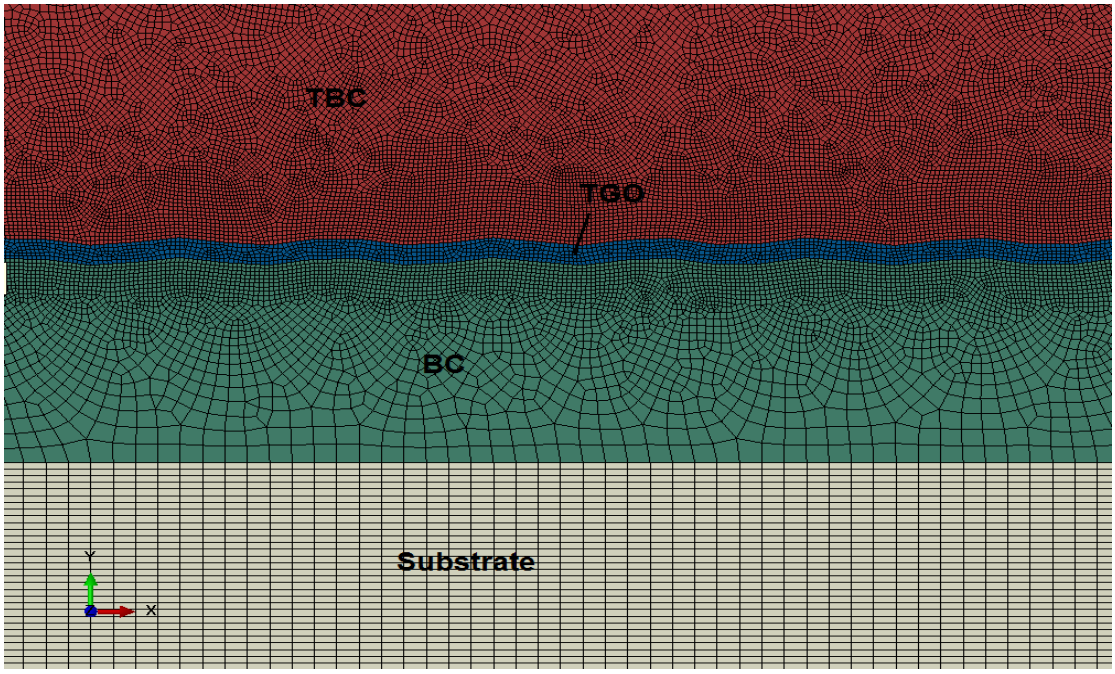

Figure 4.9: FE mesh of a thermal barrier coating system with idealized sinusoidal interfaces modeling of the TGO roughness.

4.2.5 Relevance

The in-plane compressive stresses in the TBC system are numerically determined by the constitutive model as previously explained. This work is necessary due to the importance of elastic stored strain energy which is directly dependent of the in-plane compressive stresses. During cooling in-plane stresses are generated due to the thermal expansion mismatch between different layers of the system. The system is assumed to deform following the substrate thermal expansion due to the large thickness of layer in comparison with the bond coat, TGO and top coat thicknesses. Thermal oxide sinusoidal surfaces associated with the thermal strain mismatch upon cooling, has shown to highly influence the in-plane stress field, and it can be observed from Fig. 4.10. In-plane compressive stresses supported by the TGO varies from 2.6 *GPa* to 4.9 *GPa*, and higher stresses are observed to be localized in the peak and valley regions. Comparing the results with those obtained in Chapter 3 by a plane oxide interfaces, this findings resemble the importance of consideration of TGO interface evolution in the stress prediction modeling. Concluding the high compressive stresses along the TGO demonstrate the importance of the inclusion of in-plane stresses in life time prediction models of thermal barrier coating systems and the influence of the thermally grown oxide morphology on in-plane stress evolution.

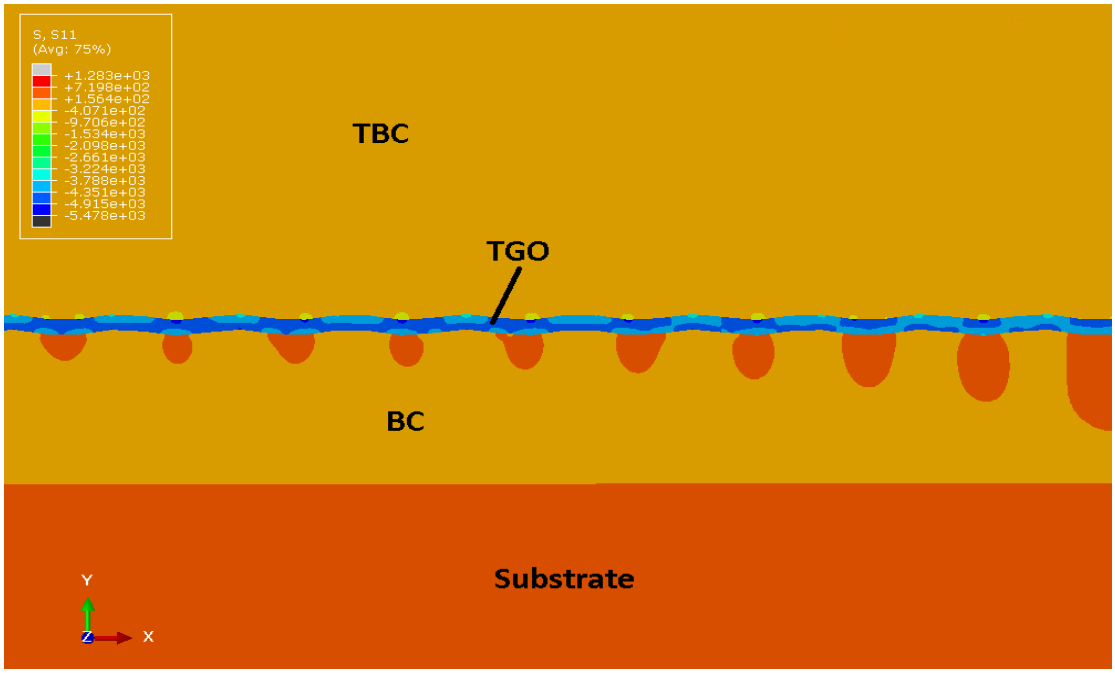

Figure 4.10: Stress distribution in the in-plane direction(x_1) along the TBC system, when creep, swelling and TGO growth formation is undertaken in the model

4.3 Finite Element Reduced Model

To get a more realistic simulation of stress distribution within the TBC system during cooling, the stress field generated during service conditions will be taken into account, followed by cooling to room temperature, representing one day cycle. For computational simplification due to high complexity, CPU and time consuming of the previous model, reduction to a two dimensional half period (w) computational model has been developed from the previous model. Symmetry is considered in the right side of the model and boundary conditions 1 are applied in the left side and fine meshing is generated in the representative element as shown in Fig. 4.3, the good agreement between the obtained results and the experimental data of literature shows that the computational model closely represents the stress evolution within the system.

4.3.1 Thermal Loading

The loading conditions for the half period model consists of two steps:

First, the component is exposed to high temperature during service for 22 hours, following temperature distribution shown in Fig. 3.7. In this step, the component is subjected to high temperature simulating service conditions. Creep and bond coat oxidation specially occur at

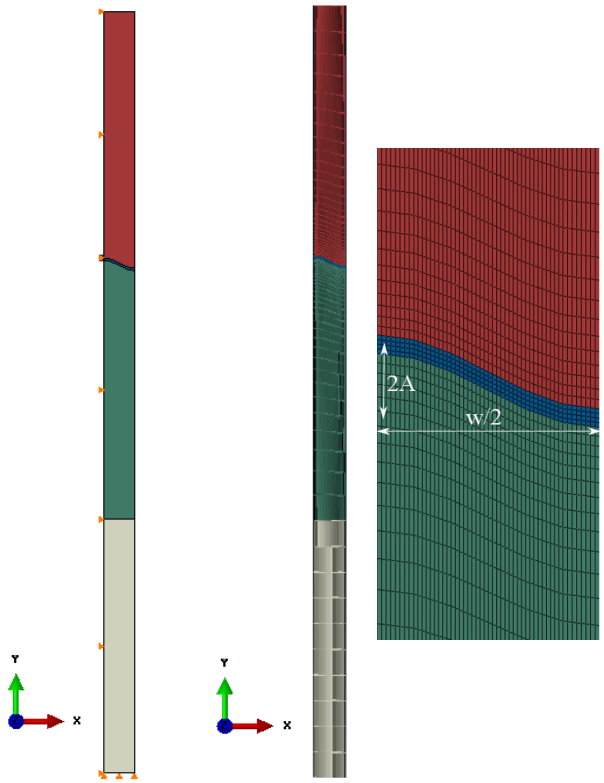

Figure 4.11: Reduced TBC model, boundary conditions, finite element mesh, and wavelength and amplitude of the sinusoidal idealized TGO interface.

elevated temperatures during service. Final thickness of the TGO will depend on the heating dwell time, for our time of 22 h the TGO growth is of a few μmTherefore stress field and deformations are considered prior to cool down.

Second, cool down from service temperature distribution to nonuniform temperature at repose state (see Fig. 3.8) during 40 min (step 2). The acquired TGO thickness prior to the cooling step is crucial in the stress field developed along the TBCs. In this we are only considering a single cycle, since fatigue and failure are not being studied.

4.3.2 Predicted Stress Field

The effect of stresses within the TBCs after service at high temperature is observed. The stress and TGO thickness after step 1 are studied. To calculate the stress along the TBC system after cool down to room temperature, step 1 is used as initial condition. Stress field will be compared with the obtained for a full component where cooling is directly studied without previous exposure to high temperatures during service, and finally will be compared with the case of flat interfaces.

Stress Distribution After Service

In this section the stresses resulting after exposing the sample to high temperatures for 22 hours will be studied. During service, the evolution of stresses in the system are influenced by creep relaxation and bond coat oxidation at high temperatures. The stress field at high temperature after 22 hours service for a thin initial TGO of size of 0.5 μm in the in-plane direction is shown (see Fig. 4.13). For the top coat layer (TBC) compressive stress of a value of -10 *MPa* is observed at the peak region, while the stresses are very low near zero in the rest. Regarding the bond coat layer maximum tensile stress (204 *MPa*) is observed between peak and valley regions due to TGO growth, that occurs in the BC-TGO interface. The stress state along the TGO is compressive, smaller in the valley and lower part of the peak regions, because of the thermal gradient in the system leading to hotter areas in TGO peak than the valleys. Maximum compressive stress is observed in the peak with values of -675 *MPa*. Relatively low stresses are observed during service conditions, TGO growth and creep relaxation are crucial factors that evolve during service and highly affect the stress state during cooling.

Stress Distribution After Cooling

The stress state resulting after cooling down to room temperature during 40 min posterior to high temperature service conditions are studied in this section (see Fig. 4.14). For the top coat layer (TBC) compressive area existing in the peak after service moves to the valley region reaching a tension value of 70 *MPa*, while the rest of the layer remain in near zero stress. Concerning the bond coat maximum tensile stress are observed still half way between the peak and valley regions showing higher stresses near the peak zone. Maximum tensile stress in the bond coat increase to a value of 678 *MPa*. Compressive stress state is observed along the TGO as previously mention after service, higher stress is observed in the upper part of the peak region raising after cooling to a value of -2.77 *GPa*. Comparing the obtained stress state in the TGO compared with the case of flat TGO interfaces, a significant increase is observed due to the consideration of creep, TGO growth and specially undulation of the surface. Lower maximum stress than the obtained for the model of the full component is observed due to the creep relaxation of the TGO and top coat at high temperature.

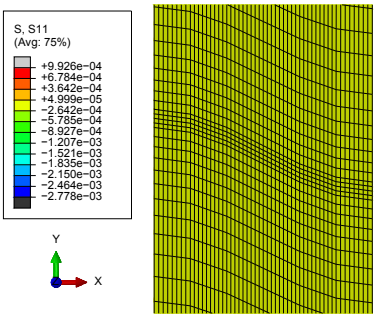

Figure 4.12: Initial model with of the part TGO thickness of 0.5 μm.

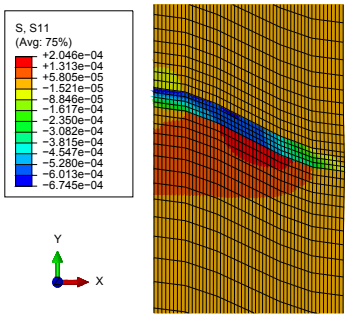

Figure 4.13: In plane stress distribution within the TBC system after service for 22 hours at high temperature for an initial TGO thickness of 0.5 μm.

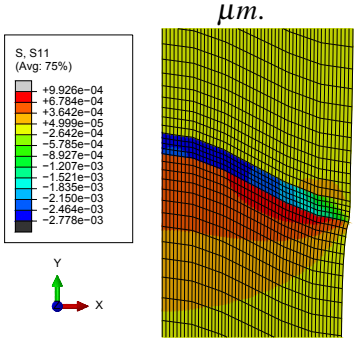

Figure 4.14: In plane stress distribution within the TBC system at room temperature after cooling for 40 min posterior to service conditions.

CHAPTER 5

Conclusion

Multiscale modeling is used to study the sintering evolution at the micro- and macroscopic level along a EB-PVD YSZ top coat, mud-cracking can occur as a result of the combination of the build up tensile stress and inter columnar sintering. Partial stress relaxation as been observed after mud-cracking driving further sintering. And hardening of the top dependent of the height of the top coat due to sintering as been concluded.

A computational model is developed to determine the stress field in a thermal barrier coating system of electron beam physical vapor deposited yttria stabilized zirconia top coat. Such system was created in the current study. After inclusion of sintering effects and graded temperature fields, and selection of the BCs after proper validation with the previous experimental and theoretical results, the current model reliable represents the qualitative stresses developed in the coatings. Quantitatively previous stress field distributions have been determined by [24], [31], [13], [10] showed higher stresses along the TGO rough interfaces. It is also found that high local stresses are concentrated in pick and valley regions of the order of 4-5 GPa. Our study provides an insight on the importance of addition of TGO rumpling formation due to bond coat oxidation and formation of the thermally grown oxide as well as plasticity of BC and TGO. Two-dimensional plane stress steady state finite element simulations have been carried out to evaluate the build up residual stresses and significance of the different parameters' consideration in the model during cooling from high to room temperatures in a thermal barrier coating

system. Among the different parameters considered affecting the evolution of stress, the importance of coupled spatially graded and temperature dependent properties effect in the build up stresses in the coating system is observed. Furthermore two dimensional coupled field plain stress transient finite element simulations were also carried out to study the effect of non considered parameters of the previous study in the stress evolution and change in microstructure during service at high temperature prior to cooling. High influence of thermally grown oxide morphology and growth was observed. The overall predictions of the model agree with the reported experimental and computational results. The presented work in this study contributes to a better understanding of the thermal stress evolution during cooling within a TBC system. In plane stresses are generated at high temperatures by the increased strain associated with the bond coat roughness, oxidation and creep.

Future work in this area can be focused in the study of creep, TGO surface roughness and thermal growth of the thermally grown oxide layer during operation conditions at high temperature and cycling loading conditions.

APPENDIX A

Functional Energy calculation Plain strain problem

Functional Energies are calculated for the different layers of the system Eq. 3.18. The sum of all the energies will be the stored energy of the system (Eqn. 3.16).

A.1 Appendix

Thermal Barrier Coating Layer

The energy function for the top coat $i = 1$ Eqn.3.18 general form is:

$$\Pi_1 = \int_0^L \int_c^{y_t} (S_{11}^1(\sigma_{xx}^1)^2 + S_{22}^1(\sigma_{yy}^1)^2 + 2S_{12}^1\sigma_{xx}^1\sigma_{yy}^1 + \sigma_{xx}^1\varepsilon_{tx}^1 + \sigma_{yy}^1\varepsilon_{ty}^1 + 2S_{66}^1(\sigma_{xy}^1)^2)\,dx \quad \text{(A.1)}$$

Introducing the values for S_{ijkl} and stresses in the different directions calculated in Chapter 3 Eqn. 3.3 , 3.4 and 3.5,

$$\Pi_1 = \int_0^L A_1\sigma_{TBC}^2 + A_2(\sigma_{TBC}'')^2 + A_3\sigma_{TBC}\sigma_{TBC}'' + A_4\sigma_{TBC} + A_5\sigma_{TBC}'' + A_6(\sigma_{TBC}')^2\,dx\,dy$$

The expressions for I_1, I_2, and I_3 are as it follows:

$$A_1 = \int_{h_b}^{h_t} (S_{11})\, dy \tag{A.2}$$

$$A_2 = \int_{h_b}^{h_t} \frac{S_{22}}{4} (h_t - y)^4\, dy \tag{A.3}$$

$$A_3 = \int_{h_b}^{h_t} S_{12} (h_t - y)^2\, dy \tag{A.4}$$

$$A_4 = \int_{h_b}^{h_t} \varepsilon_{tx}\, dy \tag{A.5}$$

$$A_5 = \int_{h_b}^{h_t} \frac{1}{2} (h_t - y)^2\, dy \tag{A.6}$$

$$A_6 = \int_{h_b}^{h_t} 2S_{66} (h_t - y)^2\, dy \tag{A.7}$$

Bond Coat

Now for $i = 2$ the internal energy in the bond coat in the general form is:

$$\Pi_2 = \int_0^L \int_{h_1}^{c} (S^a_{11}(\sigma^a_{xx})^2 + S^a_{22}(\sigma^a_{yy})^2 + 2S^a_{12}\sigma^a_{xx}\sigma^a_{yy} + \sigma^a_{xx}\varepsilon^a_{tx} + \sigma^a_{yy}\varepsilon^a_{ty} + 2S^a_{66}(\sigma^a_{xy})^2)\, dx\, dy \tag{A.8}$$

And introducing the calculated stresses in Chapter 3 shown in Eqn.3.6, 3.7, and 3.8, the above Eqn. A.8 results:

$$\Pi_2 = \int_0^L (B_1\sigma^2_{BC} + B_2(\sigma''_{TBC})^2 + B_3(\sigma''_{BC})^2 + B_4\sigma''_{TBC}\sigma''_{BC} + B_5\sigma''_{TBC}\sigma_{BC} + B_6\sigma''_{BC}\sigma_{BC} + B_7\sigma_{BC} + B_8\sigma''_{TBC} + B_9\sigma''_{BC} + B_{10}(\sigma'_{TBC})^2 + B_{11}(\sigma'_{BC})^2 + B_{12}\sigma'_{TBC}\sigma'_{BC}\, dx\, dy$$

The expressions for B_i (i=1,...,12) are the following:

$$B_1 = \int_{h_s}^{h_b} S_{11}\, dy \tag{A.9}$$

$$B_2 = \int_{h_s}^{h_b} S_{22} A^2 \, dy \tag{A.10}$$

$$B_3 = \int_{h_s}^{h_b} \frac{S_2 2}{4} B^4 \, dy \tag{A.11}$$

$$B_4 = \int_{h_s}^{h_b} S_{22} A B^2 \, dy \tag{A.12}$$

$$B_5 = \int_{h_s}^{h_b} 2 S_{12} A \, dy \tag{A.13}$$

$$B_6 = \int_{h_s}^{h_b} S_{12} B^2 \, dy \tag{A.14}$$

$$B_7 = \int_{h_s}^{h_b} \varepsilon_{tx} \, dy \tag{A.15}$$

$$B_8 = \int_{h_s}^{h_b} A \varepsilon_{ty} \, dy \tag{A.16}$$

$$B_9 = \int_{h_s}^{h_b} \frac{\varepsilon_{ty}}{2} B^2 \, dy \tag{A.17}$$

$$B_{10} = \int_{h_s}^{h_b} 2 S_{66} h_{TBC}^2 \, dy \tag{A.18}$$

$$B_{11} = \int_{h_s}^{h_b} 2 S_{66} B^2 \, dy \tag{A.19}$$

$$B_{12} = \int_{h_s}^{h_b} 2 S_{66} h_{TBC} B \, dy \tag{A.20}$$

Where A and B are:

$$A = \frac{1}{2}[(h_{TBC})^2 + 2 h_{TBC}(h_b - y)] \sigma''_{TBC} \qquad\qquad B = \frac{1}{2}(h_b - y)$$

Substrate

From the general energy Eqn. 3.18 for the substrate $i = 3$:

$$\Pi_3 = \int_0^L \int_{y_b}^{h_1} (S_{11}^2(\sigma_{xx}^2)^2 + S_{22}^2(\sigma_{yy}^2)^2 + 2S_{12}^2\sigma_{xx}^2\sigma_{yy}^2 + \sigma_{xx}^2\varepsilon_{tx}^2 + \sigma_{yy}^2\varepsilon_{ty}^2 + 2S_{66}^2(\sigma_{xy}^2)^2)\,dx\,dy \quad \text{(A.21)}$$

Introducing the calculated stresses Eqn. 3.12, 3.14, and 3.15, and values of S_{ijkl}in the energy function for the substrate, it results:

$$\begin{aligned}\Pi_3 = \int_0^L (&C_1\sigma_{TBC}^2 + C_2\sigma_{BC}^2 + C_3\sigma_{TBC}\sigma_{BC} + C_4(\sigma_{TBC})^2 + C_5(\sigma_{BC})^2 + C_6\sigma''_{TBC}\sigma''_{BC} \\ &+ C_7\sigma_{TBC}\sigma''_{TBC} + C_8\sigma_{BC}\sigma BC'' + C_9\sigma_{TBC}\sigma''_{BC} + C_{10}\sigma_{BC}\sigma TBC'' + C_{11}\sigma_{TBC} + C_{12}\sigma_{BC} \\ &+ C_{13}\sigma''_{TBC} + C_{14}\sigma''_{BC} + C_{15}(\sigma'_{TBC})^2 + C_{16}(\sigma'_{BC})^2 + C_{17}\sigma'_{TBC}\sigma'_{BC})\,dx\end{aligned} \quad \text{(A.22)}$$

Where the values forC_i (i= 1,...,17) are:

$$C_1 = \int_0^{h_s} S_{11}\lambda^2\,dy \quad \text{(A.23)}$$

$$C_2 = \int_0^{h_s} S_{11}\gamma^2\,dy \quad \text{(A.24)}$$

$$C_3 = \int_0^{h_s} S_{11}\lambda\gamma\,dy \quad \text{(A.25)}$$

$$C_4 = \int_0^{h_s} S_{22}u^2\,dy \quad \text{(A.26)}$$

$$C_5 = \int_0^{h_s} S_{22}v^2\,dy \quad \text{(A.27)}$$

$$C_6 = \int_0^{h_s} 2S_{66}uv\,dy \quad \text{(A.28)}$$

$$C_7 = \int_0^{h_s} -2S_1 2\lambda uy\,dy \tag{A.29}$$

$$C_8 = \int_0^{h_s} -2S_1 2\gamma vy\,dy \tag{A.30}$$

$$C_9 = \int_0^{h_s} -2S_1 2\lambda vy\,dy \tag{A.31}$$

$$C_{10} = \int_0^{h_s} -2S_1 2\gamma uy\,dy \tag{A.32}$$

$$C_{11} = \int_0^{h_s} -\lambda \varepsilon_{tx}\,dy \tag{A.33}$$

$$C_{12} = \int_0^{h_s} -\lambda \varepsilon_{tx}\,dy \tag{A.34}$$

$$C_{13} = \int_0^{h_s} u\varepsilon_{ty}\,dy \tag{A.35}$$

$$C_{14} = \int_0^{h_s} v\varepsilon_{ty}\,dy \tag{A.36}$$

$$C_{15} = \int_0^{h_s} 2S_{66}\lambda^2 y^2\,dy \tag{A.37}$$

$$C_{16} = \int_0^{h_s} 2S_{66}\gamma^2 y^2\,dy \tag{A.38}$$

$$C_{17} = \int_0^{h_s} 2S_{66}\lambda\gamma y^2\,dy \tag{A.39}$$

Where λ γ $u(y)$ and $v(y)$ are as follow

$$\lambda = \frac{h_t - h_b}{h_s} \qquad \gamma = \frac{h_b - h_s}{h_s}$$

$$u(y) = \frac{-y^2}{2}\lambda \qquad v(y) = \frac{-y^2}{2}\gamma$$

Introducing the calculated energies for the different layers Eqn. 3.21, 3.22, and 3.23 in Eqn. 3.16, the obtained functional energy for the system is:

$$\begin{aligned}\Pi = \int_0^L (&\beta_1 \sigma_T BC + \beta_2 \sigma_B C + \beta_3 (\sigma_T BC'')^2 + \beta_4 (\sigma_B C'')^2 + \beta_5 \sigma_{TBC} \sigma_{BC} + \beta_6 \sigma''_{TBC} \\ &+ \beta_7 \sigma''_{BC} + \beta_8 (\sigma''_{TBC})^2 + \beta_9 (\sigma''_{BC})^2 + \beta_{10} \sigma''_{TBC} \sigma''_{BC} + \beta_{11} (\sigma'_{TBC})^2 + \beta_{12} (\sigma'_{BC})^2 \\ &+ \beta_{13} \sigma'_{TBC} \sigma'_{BC} + \beta_{14} \sigma_{TBC} \sigma''_{TBC} + \beta_{15} \sigma_{BC} \sigma''_{BC} + \beta_{16} \sigma_{TBC} \sigma''_{BC} + \beta_{17} \sigma_{BC} \sigma''_{TBC}) \, dx\end{aligned}$$

The values of β_i (i=1,...,17) in therms of A_i, B_i and C_i are:

$$\beta_1 = A_4 + C_{11} \tag{A.40}$$

$$\beta_2 = B_7 + C_{12} \tag{A.41}$$

$$\beta_3 = A_1 + C_1 \tag{A.42}$$

$$\beta_4 = B_1 + C_2 \tag{A.43}$$

$$\beta_5 = C_3 \tag{A.44}$$

$$\beta_6 = A_5 + B_8 + C_{13} \tag{A.45}$$

$$\beta_7 = B_9 + C_{14} \tag{A.46}$$

$$\beta_8 = A_2 + B_2 + C_4 \tag{A.47}$$

$$\beta_9 = B_3 + C_5 \tag{A.48}$$

$$\beta_{10} = B_4 + C_6 \tag{A.49}$$

$$\beta_{11} = A_6 + C_{15} + B_{10} \tag{A.50}$$

$$\beta_{12} = B_1 1 + C_1 6 \tag{A.51}$$

$$\beta_{13} = B_{12} + C_{17} \tag{A.52}$$

$$\beta_{14} = A_3 + C_7 \tag{A.53}$$

$$\beta_{15} = B_6 + C_8 \tag{A.54}$$

$$\beta_{16} = C_9 \tag{A.55}$$

$$\beta_{17} = B_5 + C_{10} \tag{A.56}$$

Now that the functional F is defined, we can evaluate it in Eqn. 3.26 and 3.27, what yields in two Ordinary Differential Equations as in Eqn.3.28 and 3.29. represented bellow:

$$\alpha_7 + \alpha_6\sigma_{TBC} + \alpha_5\sigma_{BC} + \alpha_4\sigma''_{TBC} + \alpha_3\sigma''_{BC} + \alpha_2\sigma''''_{TBC} + \alpha_1\sigma''''_{BC} = 0$$

$$\eta_7 + \eta_6\sigma_{TBC} + \eta_5\sigma_{BC} + \eta_4\sigma''_{TBC} + \eta_3\sigma''_{BC} + \eta_2\sigma''''_{TBC} + \eta_1\sigma''''_{BC} = 0$$

The values for α_i (i=1,...,7) in Eqn.3.28 are:

$$\alpha_1 = \beta_{10} \tag{A.57}$$

$$\alpha_2 = 2\beta_8 \tag{A.58}$$

$$\alpha_3 = \beta_{16} - \beta_{13} + \beta 17 \tag{A.59}$$

$$\alpha_4 = 2\beta_{14} - 2\beta_{11} \tag{A.60}$$

$$\alpha_5 = \beta_5 \tag{A.61}$$

$$\alpha_6 = 2\beta_3 \tag{A.62}$$

$$\alpha_7 = \beta_1 \tag{A.63}$$

And the values for η_i (i=1,...,7) of Eqn.3.29 are:

$$\eta_1 = \beta_9 \tag{A.64}$$

$$\eta_2 = 2\beta_{10} \tag{A.65}$$

$$\eta_3 = 2\beta_{15} - 2\beta_{12} \tag{A.66}$$

$$\eta_4 = \beta_{17} - \beta_{13} + \beta 16 \tag{A.67}$$

$$\eta_5 = \beta_4 \tag{A.68}$$

$$\eta_6 = 2\beta_5 \tag{A.69}$$

$$\eta_7 = \beta_1 \tag{A.70}$$

APPENDIX B

Abbreviations

TBC Thermal Barrier Coating

TGO Thermal Grown Oxide

BC Bond Coat

YSZ Yttria Stabilized Zirconia

Pt-Al Platinum Aluminide

DOF Degrees of Freedom

ODE Ordinary Differential Equation

PDE Partial Differential Equation

TVP Thermodynamic Variational Principle

Eqn Equation

Fig Figure

EB-PVD Electron Beam Physical Vapor Deposition

APS Air Plasma Spray

BCs Boundary Conditions

TET Turbine Entry Temperature

CTE Coefficient of Thermal Expansion

FEA Finite Element Analysis

E Young's modulus

ν Poisson's Ratio

ε Strain

σ Stress

G Gibbs Free Energy

U,π Elastic Stores Strain Energy or Potential Energy

Ψ Rate Potential

Bibliography

[1] S. P. A. Gill A. C. F. Cocks and J. Pan. Modelling microstructure evolution in engineering materials. *Advances in Applied Mechanics*, 36:81–161, 1999.

[2] D.R. Mumm J.W. Hutchinson G.H. Meier A.G. Evans and F.S. Pettit. Mechanisms controlling the durability of thermal barrier coatings. *Progress in Materials Science*, 5:505–553, 2001.

[3] W.J. Brindley A.M. Freborg, B.L. Ferguson and G.J. Petrus. Modeling oxidation induced stresses in thermal barrier coatings. *Materials Science and Engineering*, A245:182–190, 1998.

[4] Evgeny Grigoryev Andrey Maximenko, Andrey Kuzmov and Eugene Olevsky. Direct multi-scale modeling of sintering. *J. Am. Ceramic Society*, 95:2383–2388, 2012.

[5] W. Lee Y. Zhang K. Prubner B. Pint, I. Wright and K. Alexander. Substrate and bond coat compositions: factor affecting alumina scale adhesion. *Materials Science Engineering*, 245:201–211, 1998.

[6] R. Vassen B. Siebert, C. Funke and D. Stover. Changes in porosity and young's modulus due to sintering of plasma sprayed thermal barrier coatings. *Journal of Materials Processing Technology*, 92-93:217–223, 1999.

[7] K. Kokini B.D. Choules and T.A. Taylor. Thermal fracture of ceramic thermal barrier coatings under high heat flux with time-dependent behaviorpart i: experimental results. *Material Science Engineering*, A299:296–304, 2001.

[8] DAWES W.N. JARRETT J.P. BELL, C.P. and P.J. CLARKSON. Improving the conceptual design of turbine rotor blade cooling systems in iced05. *15th International Conference on Engineering Design, Melbourne, Australia.*, 2005.

[9] J. Besson and M. Abouf. Rheology of porous aluminia and simulation of isostatic pressing. *Journal of American Ceramic Society*, 75:2165–2172, 1992.

[10] M. Bialas. Finite element analysis of stress distribution in thermal barrier coatings. *Surface and Coating Technology*, 202:6002–6010, 2008.

[11] A. F. Bower. Applied mechanics of solids. *CRC Press*, 2010.

[12] E. Busso and Z. Qian. Mechanistic study of microcracking in transversely isotropic ceramic-metal systems. *Acta Materialia*, 54:325–338, 2006.

[13] Feyel F. Kruch S. Caliez, M. and J. Chaboche. Oxidation induced stress fields in an eb-pvd thermal barrier coatings. *Surface and Coating Technology*, pages 103–110, 2002.

[14] D. Chung and G. Simmons. Pressure and temperature dependences of the isotropic elastic moduli of polycrystalline alumina. *Journal of Applied Physics*, 39:5316–5326, 1968.

[15] D. Clarke. The lateral growth strain accompanying the formation of a thermally grown oxide. *Acta Materialia*, 51:1393–1407, 2003.

[16] R. Coble. Sintering crystalline solids i and ii. *Journal of Applied Physics,*, 32:787–799, 1961.

[17] Kurt Kremer Walter Thiel Jrg Neugebauer Dierk Raabe, Matthias Scheffler and Martin Jansen. Multi-scale modeling in materials science and engineering. *Max-Planck-Gesellschaft*, 2001.

[18] Weinan E. *Principles of Multiscale Modeling*. 2011.

[19] S. Barwulf E. Lugscheider, K. Bobzin and A. Etzkorn. Mechanical properties of eb-pvd tbcs by nano-indentation. *Surface and Coating Technology*, 138:9–13, 2001.

[20] General Electric. Ge flexefficiency* 60 natural gas turbine means cleaner air and more renewables. *Ecomagination*, 1, 2012.

[21] H.E. Evans L.N. McCartney S.R.J. Saunders S. Osgerby E.P. Busso, L. Wright and J. Nunn. A physical-based life prediction methodology for thermal barrier coating systems. *Acta Meterialia*, 55:1491–1503, 2007.

[22] M.P. Taylor E.P. Busso, Z.Q. Qian and H.E. Evans. The influence of bondcoat and topcoat mechanical properties on stress development in thermal barrier coating systems. *Thin Solid Films*, 488:274–282, 2005.

[23] Swinkels FB and Ashby MF. A second report on sintering diagrams. *Acta Metall*, pages 29–259, 1981.

[24] Julien Frachon. Multiscale approach to preduct the life time of eb-pvd thermal barrier coatings. *Ecole Nationale Superieure des Mines de Paris*, page 160, 2009.

[25] H. J. Frost and M. F. Ashlby. Deformation-mechanism maps: The plasticity and creep of metals and ceramics. *Pergamon Press*, 1982.

[26] B. Barber J. Cheng, E.H. Jordan and M. Gell. Thermal/residual stress in an electron beam physical vapor deposited thermal barrier coating. *Acta mater*, 46(16):5839–5850, 1998.

[27] H. Chan J. Rickman J. Cho, M. Harmer and A. Thompson. Effect of yttrium and lanthanum on the tensile creep behavior of aluminium oxide. *Journal of American Ceramic Society*, 80:1013–1017, 1997.

[28] M. Harmer H. Chan J. French, J. Zhao and G. Miller. Creep of duplex microstructure. *Journal of American Ceramic Society*, 77:2857–2865, 1994.

[29] J. Capek J. Martan and E. Amin Chalhoub. Measurement of thermal properties of thin films up to high temperaturespulsed photo-thermal radiometry system and sibcn films. *Review of Scientific Instruments*, 81, 2010.

[30] A. Johnstone J.R. Nichollsa, K.J. Lawson and D.S. Rickerby. Methods to reduce the thermal conductivity of eb-pvd tbcs. *Surface and Coatings Technology*, 151-152:383–391, 2002.

[31] J. K., Aktaa and D. Munz. Numerical investigation of the residual stress field and crack behavior in tbc systems. *Materials Science Engineering*, 333:351–360, 2002.

[32] M.F.J. Koolloos. Behaviour of low porosity microcracked thermal barrier coatings under thermal loading, 2001.

[33] S. Kumar and A.C.F. Cocks. Sintering and mud cracking in eb-pvd thermal barrier coatings. *Journal of the Mechanics and Physics of Solids*, 60:723–749, 2012.

[34] E. H. Jordan N. P. Padture T. Xiao L. Xie, X. Ma and M. Gell. Deposition of thermal barrier coatings using the solution precursor plasma spray process. *Journal Of Materials Science*, 39:1639–1646, 2004.

[35] Akhlesh Lakhtakia and Joseph B. Geddes III. Thin-film metamaterials called sculptured thin films. *Trends in Nanophysics*, 1:59–71, 2010.

[36] L. Lapin. Effect of ageing on the microstructure and mechanical behaviour of a directionnaly solidified ni3al-based alloy. *Intermetallics*, 5:615–624, 1997.

[37] J. Sumner M. Seraffon, N.J. Simms and J.R. Nicholls. The development of new bond coat compositions for thermal barrier coating systems operating under industrial gas turbine conditions. *Surface and Coatings Technology*, 206:1529–1537, 2011.

[38] S. Gray M. Taylor and H. Evans. Contract report. *Siemens*, 2006-2007.

[39] J.W. Hutchinson M.Y. He and A.G. Evans. Simulation of stresses and delamination in a plasma-sprayed thermal barrier system upon thermal cycling. *Material Science and Engineering*, 345:172–178, 2003.

[40] T. Bhatia A. Ozturk B. Cetegen E.H. Jordan M. Gell S Jiang T.D. Xiao P.R. Strutt E. Garcia P. Miranzo N.P. Padture, K.W. Schlichting and M.I. Osendi. Towards durable thermal barrier coatings with novel microstructures deposited by solution-precursor plasma spray. *Acta Materialia*, 49:2251–2257, 2001.

[41] A. Wolfenden P. Jaminet and V. Kinra. Mechanics and mechanisms of material damping. *American Society For Testing and Materials*, 1992.

[42] M. Padture, N.P. Gell and E.H. Jordan. Thermal barrier coatings for gasturbine engine applications. *Science*, 296:280–284, 2002.

[43] B. Pint and K. More. Characterization of alumina interfaces in tbc systems. *Journal of Materials Science*, 44:1676–1686, 2009.

[44] R. L. McKnight T. S. Cook R. V. Hillery, B. H. Pilsner and M. S. Hartle. Contract report. *NASA*, 1:180807, 1988.

[45] A. Mukherjee R. Vandervoort and J. Dorn. *Trans. American Society Metals*, 59:930, 1966.

[46] Sudarshan Rangaraj and Klod Kokini. Estimating the fracture resistance of functionally graded thermal barrier coatings fromtherm al shock tests. *Surface and Coatings Technology*, 173:201–212, 2003.

[47] L. N. Reddy. Energy principles and variational methods in applied mechanics. *Jon Willey Sons*, 2002.

[48] N.A. Fleck R.G. Hutchinson and A.C.F. Cocks. A sintering model for thermal barrier coatings. *Acta Materialia*, 54:1297–1306, 2006.

[49] T.N. Rhys-Jones and F.C. Toriz. Thermal barrier coatings for turbine applications in aero engines. *High Temperatures Technology*, 7:73–81, 1989.

[50] B. Dalgleish S. Johnson and A. Evans. High-temperature failure of polycrsystalline alumina: Iii, failures times. *Journal of American Ceramic Society*, 67:759–763, 1984.

[51] Richard Allan Schapery. Irreversible thermodynamics and variational principles with applications to viscoelasticity. *California Institute of Technology*, 1962.

[52] G. Simmons and H. Wang. Single crystal elastic constants and calculated aggregate properties: A handbook. *MIT*, 2nd, 1971.

[53] D. M. Nissley S.M. Meier and K. D. Sheffler. Contract report. *NASA*, 1:189111, 1989.

[54] Thomas Sourmail. Coatings for turbine blades. *U.K. Centre for Materials Education*, 2009.

[55] Z. Suo. Motions of microscopic surfaces in materials. *Advances in Applied Mechanics*, 33:193–294, 1997.

[56] N. Shibata K. Matsunaga T. Mizoguchi T. Yamamoto H. Haneda T. Nakagawa, I. Sakaguchi and Y. Ikuhara. Yttrium doping effect on oxygen grain boundary diffusion in -al2o3. *Acta Materialia*, 55:6627–6633, 2007.

[57] K. Fritscher U. Schulz and M. Peters. Eb-pvd y203 and ceo2/y203 stabilized zirconia thermal barrier coatings- crystal habit and phase composition. *Surface and Coatings Technolog*, 82:259–269, 1996.

[58] K. Fritscher U. Schulz, B. Saruhan and C. Leyens. Review on advanced eb-pvd ceramic topcoats for tbc applications. *International Journal Applied Ceramics Technology*, 4:302–315, 2004.

[59] W. Fischer H.P. Buchkremer V. Teixeira, M. Andritschky and D. StoEver. Analysis of residual stresses in thermal barrier coatings. *Journal of Materials Processing Technology*, 92-93:209–216, 1999.

[60] Vladimir K. Tolpygo Vanni Lughi and David R. Clarke. Microstructural aspects of the sintering of thermal barrier coatings. *Materials Science and Engineering*, A368:212221, 2004.

[61] J.B. Wachtman. Mechanical properties of ceramics. *John Wiley*, 996.

[62] John Wiley and Sons. *Supplemental Proceedings : Materials Fabrication, Properties, Characterization, and Modeling*. 2011.

[63] H.D Wang X.C Zhang, B.S. Xu and Y.X. Wu. An analytical model for predicting thermal residual stresses in multilayer coating systems. *Thin Solid Films*, 488:274–282, 2005.

[64] R.Vassen X.Q. Cao and D. Stover. Ceramic materials for thermal barrier coatings. *Journal of the European Ceramic Society*, 24:1–10, 2004.

[65] O.A. Zubacheva. Comparative analysis of thermal behavior based on curvature studies. *TU University of Aachen*, 2004.